Analog Optical Links: Modeling and Implementation

Sidney Buchbinder

Electrical Engineering and Computer Sciences
University of California, Berkeley

Technical Report No. UCB/EECS-2023-41
http://www2.eecs.berkeley.edu/Pubs/TechRpts/2023/EECS-2023-41.html

May 1, 2023

Analog Optical Links: Modeling and Implementation

by

Sidney Douglas Buchbinder

A dissertation submitted in partial satisfaction of the

requirements for the degree of

Doctor of Philosophy

in

Electrical Engineering and Computer Science

in the

Graduate Division

of the

University of California, Berkeley

Committee in charge:

Professor Vladimir Stojanović, Chair
Professor Ali Niknejad
Professor Liwei Lin

Spring 2022

Analog Optical Links: Modeling and Implementation

Abstract

Analog Optical Links: Modeling and Implementation

by

Sidney Douglas Buchbinder

Doctor of Philosophy in Electrical Engineering and Computer Science

University of California, Berkeley

Professor Vladimir Stojanović, Chair

As next generation wireless and sensing systems scale to massive array sizes, so too scales the cost and complexity of data transmission and aggregation across the array. Silicon photonic links offer promising solutions to meet the high bandwidth and energy efficiency requirements of these future systems. This work addresses three challenges facing input/output scaling in photonic links. First, a new photonic system design framework called Berkeley Photonics Generator (BPG) is presented. BPG is an open-sourced, modular, and easy-to-use framework for end-to-end photonic system design. BPG aims to create an agile, robust, and easily adoptable workflow with a rich set of reusable libraries to boost the photonic design ecosystem. The design philosophy, plugin-based architecture, and technology-agnostic design workflow are described, and several design results enabled by BPG are discussed. Next, a new framework for modeling crosstalk and insertion loss penalty in digital optical links is presented. This framework provides intuitive understanding for the receive-filter imposed limitations of channel densification in optical links. The major sources of signal impairment are identified as functions of technology parameters and system design choices, such as channel spacing. The framework is used to derive optimal filter design parameters, and the utility of higher order filters is considered. Finally, analog modulation in optical links is proposed as an alternative signaling modality for high-bandwidth links. The fundamental gain and noise performance are derived for a generic analog optical link, and the performance of a microring in GlobalFoundries 45CLO platform is validated for use as a WDM compatible analog optical modulator. A proof-of-concept microring-resonator-based analog WDM link system is designed for data remoting in magnetic resonance imaging (MRI), demonstrating an SFDR3 of $63\,\mathrm{dBHz}^{2/3}$.

To my family.

Contents

List of Figures

List of Tables

Acknowledgments

It is with a great deal of gratitude that I look back at my experience at Berkeley. I am indebted to so many people: mentors, collaborators, friends, and family, without whom this work would not be possible.

First and foremost, I would like to thank my advisor Professor Vladimir Stojanović. I could not imagine a better mentor to guide me and help me grow. I thank Vladimir for his deep insight, infinite patience, and passion towards his work. Vladimir is more than an academic advisor; he serves as a role model for how to be a great leader, researcher, and person. Thank you, Vladimir, for your faith and support in my many efforts. I look forward to continuing to work with you in the future.

I would next like to thank Professor Ali Niknejad and Professor Liwei Lin for serving on my thesis and qualifying exam committees, and Professor Michael Lustig for serving on my qualifying exam committee. I appreciate your interest and feedback on my work, and thank you for your technical guidance.

It was a pleasure to collaborate with and learn from Professor Miloš Popović at Boston University. I thank you for many interesting and insightful conversations on optical device design. I greatly appreciate the collaborations I had with Professor Popović's students; in particular I would like to thank Josep, Hayk, Deniz, and Manuj.

One of the greatest opportunities in graduate school has been the opportunity to learn from and work with so many talented and passionate students. I would especially like to thank all the members of the Integrated Systems Group (ISG), from whom I learned so much. Thank you to Panagiotis Zarkos and Christos Adamopoulos, for being my 'partners in crime' throughout my PhD. Thank you as well to Pavan Bhargava, one of the smartest and most driven people I know. Thank you to Ruocheng Wang, for our close collaboration on many analog links projects. I was fortunate to have such great mentors in the more senior ISG students. Thank you to Sajjad, Krishna, Nandish, Sen, and Taehwan for being invaluable teachers. I would like to thank all the other ISG members with whom I have worked: Bozhi, Daniel, Kourosh, Erik, and Sunjin– I wish you the best of luck on your endeavors. It has been a pleasure working with you all, and I value the friendships we have built.

I am incredibly grateful for all the students at BWRC. It was a joy to work in such a diverse, creative, and driven environment. Special thanks to Nathan, John, Greg, Lorenzo, and Sashank, for putting up with all my questions. Thank you as well to all the staff at BWRC and in the EECS department. Special thanks to Candy Corpus for being a great friend, and working tirelessly to take care of me and all BWRC students.

I was fortunate to get the opportunity to intern at Ayar Labs during part of my PhD. I am grateful to John, Anatoly, Derek, Mark, Chen, and the entire team for being incredible colleagues. I learned so much working with you all, and greatly appreciate all the discussions on optical design, system architecture, and how to take a project from concept to product.

I wish to thank the many friends that have supported me throughout graduate school. In addition to those mentioned above, special thanks to Keertana, Emily, and Andy for the close friendships we have formed. It was a pleasure to live with many great housemates throughout graduate school: thank you to Federico, Amrutha, Alison, Alok, Ann, Joe, Richard, and Jared. A special shout out goes to Jackie and Linda– thank you for being truly great friends, and for living with me for nearly ten years. Graduate school, and life in general, would not have been as special without you all. To everyone who supported me throughout my PhD, I am and will be forever grateful.

Finally, my special thanks and enormous gratitude go to my parents, brother, sister, and entire family. Thank you for your unwavering support, boundless encouragement, and endless love. You have always believed in me, and have helped me become the person I am today. I will always love you all.

Support: This work was supported in part by the National Science Foundation Graduate Research Fellowship Program award number DGE 1752814; by ComSenTer, a research center part of the Semiconductor Research Corporation (SRC) program JUMP; and by the Director's Innovation Initiative (DII) program. I would also like to thank the BNC and Marvell Nanofabrication Laboratory at UC Berkeley, Santec Corporation, Ayar Labs, and the Berkeley Wireless Research Center for their support.

Chapter 1

Introduction

Input/output (I/O) scaling is one of the key challenges facing next-generation wireless systems as well as many other compute and sensing systems. As wireless systems transition to 5G and beyond, adoption of massive multiple-input multiple-output (MIMO) arrays will be required to provide better spectral utilization and spacial beamforming capability. In a similar trend, future sensing systems will look to utilizing larger arrays of sensors to provide spatially multiplexed sampling, or to take advantage of the signal quality gains as array size increases. Such arrays can be physically large with many elements and chips, and require significant amounts of power to aggregate data from across the array.

Co-packaged and fully integrated silicon photonics offer great potential in meeting the low-power high-bandwidth requirements for future I/O interconnects. Silicon photonics transceivers are becoming the ubiquitous solution for inter and intra-rack interconnects in the datacenter, providing high speed solutions at energies below 10pJ per bit [1, 2]. In addition, silicon photonic links enable further bandwidth density scaling by utilizing wavelength division multiplexing (WDM), in which multiple distinct data streams can be transmitted along a single optical fiber. As future bandwidth requirements continue to scale, system designers must similarly scale the complexity and density of optical links.

1.1 Thesis Organization and Contributions

This work attempts to address three challenges facing I/O scaling in photonic links.

1. Large scale and complex electronic-photonic systems require new layout and verification tools to enable rapid, flexible, and scalable design methodologies.
2. Achieving high data densities requires proper understanding of the design tradeoffs when targeting high channel count WDM systems.
3. As data bandwidth scales, conventional digital signalling requires high power as the energy per bit reaches a plateau; thus, alternative signaling modalities such as analog modulation can provide power-efficient solutions.

In Chapter 2, the author presents the Berkeley Photonics Generator (BPG). BPG offers an end-to-end photonic system design framework, which allows the full electronic-photonic design flow to be managed from a single source. This framework enables engineers to implement large-scale photonic systems rapidly and with design confidence. BPG promotes a technology-agnostic generator-based coding methodology, and has produced functioning systems in a number of technology nodes. This work is done in collaboration with Pavan Bhargava and Ruocheng Wang. Parts of this work appear in

- [3] V. M. Stojanović, P. Bhargava, **S. Buchbinder**, and J. Kim, "EPDA for EPSoC design: From co-simulation to photonic circuit generators," in Design Automation and Test in Europe (DATE), 2019.

and a paper is currently in review in Transactions on Computer-Aided Design of Integrated Circuits and Systems. In addition, this work has enabled the photonic designs which have appeared in

- [4] P. Zarkos, **S. Buchbinder** et al., "Monolithically Integrated Electronic-Photonic Ultrasound Receiver Using Microring Resonator," 2021 Conf. Lasers Electro-Optics, CLEO 2021 - Proc., pp. 2021–2022, 2021.
- [5] C. Adamopoulos, **S. Buchbinder** et al., "Fully Integrated Electronic-Photonic Biosensor for Label-Free Molecular Sensing in Advanced Zero-Change CMOS-SOI Process," 2021 Conf. Lasers Electro-Optics, CLEO 2021 - Proc., pp. 4–5, 2021.
- [6] C. Adamopoulos, P. Zarkos, **S. Buchbinder** et al., "Lab-on-Chip for Everyone: Introducing an Electronic-Photonic Platform for Multiparametric Biosensing Using Standard CMOS Processes," IEEE Open J. Solid-State Circuits Soc., vol. 1, no. October, pp. 198–208, 2021.
- [7] M. Wade et al., "An Error-free 1 Tbps WDM Optical I/O Chiplet and Multi-wavelength Multi-port Laser," 2021 Opt. Fiber Commun. Conf. Exhib. OFC 2021 - Proc., no. c, pp. 6–8, 2021.

as well as other published works.

In Chapter 3, a new framework for modeling crosstalk and insertion loss penalty for digital optical links is presented. This framework provides intuitive understanding for the receive-filter imposed limitations of channel densification in optical links. The major sources of signal impairment are identified as functions of technology parameters and system design choices, such as channel spacing. The modeling framework is used to derive the optimal receiver filter design as a function of these technology and system parameters. Finally, the utility of higher order filters is considered. The results of this work provide design guidelines that help determine how to properly scale channel count and data density in optical links.

In Chapter 4, the performance of analog modulation in optical links is explored. The fundamental gain and noise performance are derived for a generic analog optical link. Next, the author derives optimal design parameters for low frequency microring modulators. The linearity and noise performance of microrings as resonant modulator devices are then investigated. Characterization of the linearity performance of a microring in GlobalFoundries 45nm CLO platform is presented. This work will be presented in

- [8] **S. Buchbinder** et al., “Silicon Microring Modulator for High SFDR Analog Links in Monolithic 45nm CMOS,” in Conference on Lasers and Electro-Optics, 2022. To be published.

In Chapter 5, a proof-of-concept microring-resonator-based analog optical link system for magnetic resonance imaging (MRI) data remoting is presented. This system utilizes microring modulators to perform WDM-compatible analog optical modulation. The design objectives and circuit implementation details are provided, and the packaging flow required for this monolithic electronic-photonic IC is detailed. Current measurement status is provided. This work was done in collaboration with Ruocheng Wang. The author’s main contributions to this work are the overall link modeling, digital and optical system design, full-chip integration, and packaging flow.

Chapter 2

Berkeley Photonics Generator

2.1 Introduction

Over the past decade, research and development in integrated photonic systems has matured, heralding their deployment in new high volume products. These new photonic systems will have an impact across a wide range of applications, from digital communications and biosensors to autonomous vehicles and machine learning. Scaling integrated photonic systems to support these applications necessitates a design workflow that enables novel device development, scalability to systems with many thousands of optical devices, compatibility with electronic-photonic integration, and a robust verification methodology.

To date, many independent approaches to establishing such a design workflow have been pursued [9], some focused on supporting custom mask layout for research applications [10] and others focused on creating an ecosystem around assembling foundry-made PDK components. While each of these approaches has been successful within their respective domains, the needs of emerging high-volume integrated photonic systems bridge the gap between these approaches.

Many of the major EDA companies offer integrated photonic design environments, which rely on close foundry collaboration for PDK releases and which frequently treat low-level optical devices as black boxes that system designers snap together in a graphical environment [11, 12]. These types of environments are useful in lowering the barrier to entry for designing simple systems with existing foundry made components. However, as competition increases in the photonics space, designers will need to differentiate themselves with novel devices, design techniques, and large-scale photonic designs, which is challenging with these tools.

A significant amount of research in the academic space leverages open source tools such as gdspy or KLayout [10, 13]. These tools allow designers to have fine grain control over the geometry of the primitive devices. However, they lack close integration with standard simulation and verification tools and the higher-level features required to enable easier large-scale photonic system design and integration. As a result, most designers need to combine many different commercial and custom tools to successfully create and verify a new design.

To address these shortcomings, we present the Berkeley Photonics Generator (BPG), an open-sourced, modular, and easy-to-use framework for end-to-end photonic system design [14]. BPG utilizes a plugin-based architecture with flexible support for third party tools, enabling a full design flow managed from a single source. BPG provides low-level design capabilities, enabling custom device design, as well as high-level integration features, enabling large-scale system design. By encouraging technology-agnostic generator-based design methodologies, BPG enables significant design reuse across different projects and technology nodes. BPG aims to create an agile, robust, and easily adoptable workflow with a rich set of reusable libraries to boost the photonic design ecosystem.

The remainder of the chapter outlines the design workflow from layout to verification. Section II discusses the overall architecture and design philosophies of the BPG framework, and Section III details the layout generation framework. Section IV presents an overview of the *Photonic Compiler* and describes how a technology agnostic design is automatically converted into technology specific design. Section V details BPG's optical testbench generation capabilities and interface to third party optical simulation tools. Section VI describes BPG's schematic and behavioral simulation capabilities. Section VII highlights several examples of large-scale integrated electronic-photonic designs, which were uniquely enabled by the BPG framework. Finally, Section VIII presents a conclusion and discusses future work.

2.2 BPG Design Philosophy

The BPG software platform was designed as a highly modular, plugin-based framework. One of the overarching goals of the BPG framework was to establish a unified ecosystem that brings together the various tools and methodologies required in electro-optic device and system design. The primary features enabled by BPG include: layout generation, technology compilation, optical simulation, behavioral simulation, and verification.

In order to create such a unified ecosystem, BPG utilizes a centralized design manager (Fig. 2.1) to control the flow of a design through the various stages of its development. Each of the primary features provided by BPG corresponds to one of the steps followed during a standard design process. Specialized plugins within each feature category have been developed to provide the required functionality, or manage an interface to a 3rd party tool. The central design manager stores the various elements of the design in a centralized database, and provides an interface between plugins that can be used to pass data through the design flow. Plugins are accessed through simple function calls, so that the top level design flow can be managed through a simple script (Fig. 2.2). BPG's plugin-based design philosophy allows new tools to be easily integrated into the design environment, and enables additional features to be added without disrupting existing workflows. In addition, by separating the design flow into distinct modules, multiple designers can collaborate and specialize in different aspects of design within a common framework. Finally, by storing the design content in a centralized database, BPG obviates the laborious and error prone task of manually porting the same design between various tools.

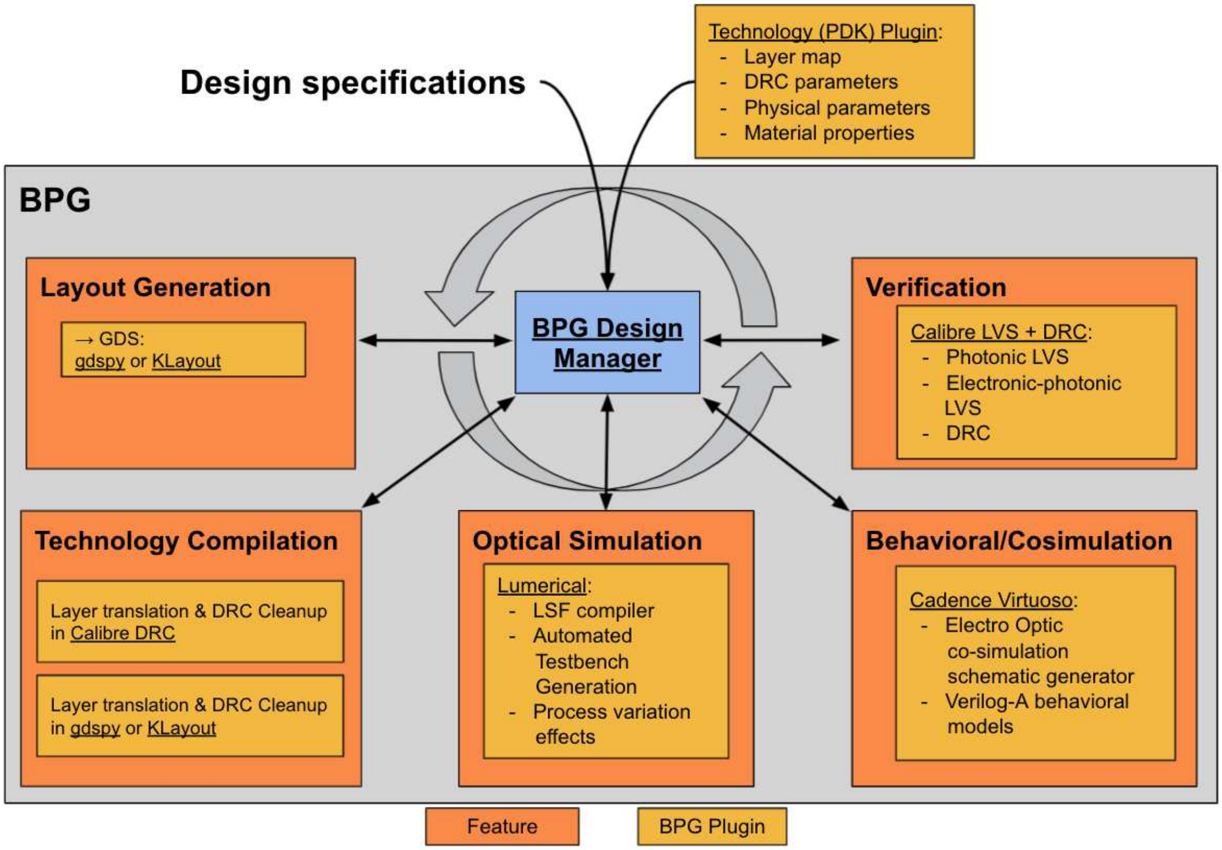

Figure 2.1: Main features provided by BPG, and the plugins that support those features. A central manager coordinates data flow between the various plugins. Designer specifications are provided as input to the design manager. A technology plugin, created once per technology process or provided as part of a PDK, abstracts foundry specific details from the design process.

BPG is written in the Python programming language. Python was chosen for several reasons. First, it is a very popular, easy to learn, and open source language. Python has many established libraries (such as NumPy, SciPy, pandas, and more) that are extensively utilized in the scientific community, that can be used to perform computation, optimization, data import/export, and other operations, eliminating the need for developers to create their own specialized tools. In addition, Python is simple to install on most platforms, enabling easy distribution and adoption of BPG. Finally, Python makes it simple to perform tasks such as dynamic module importing during run time, which are useful when user input specifications can modify the class hierarchy.

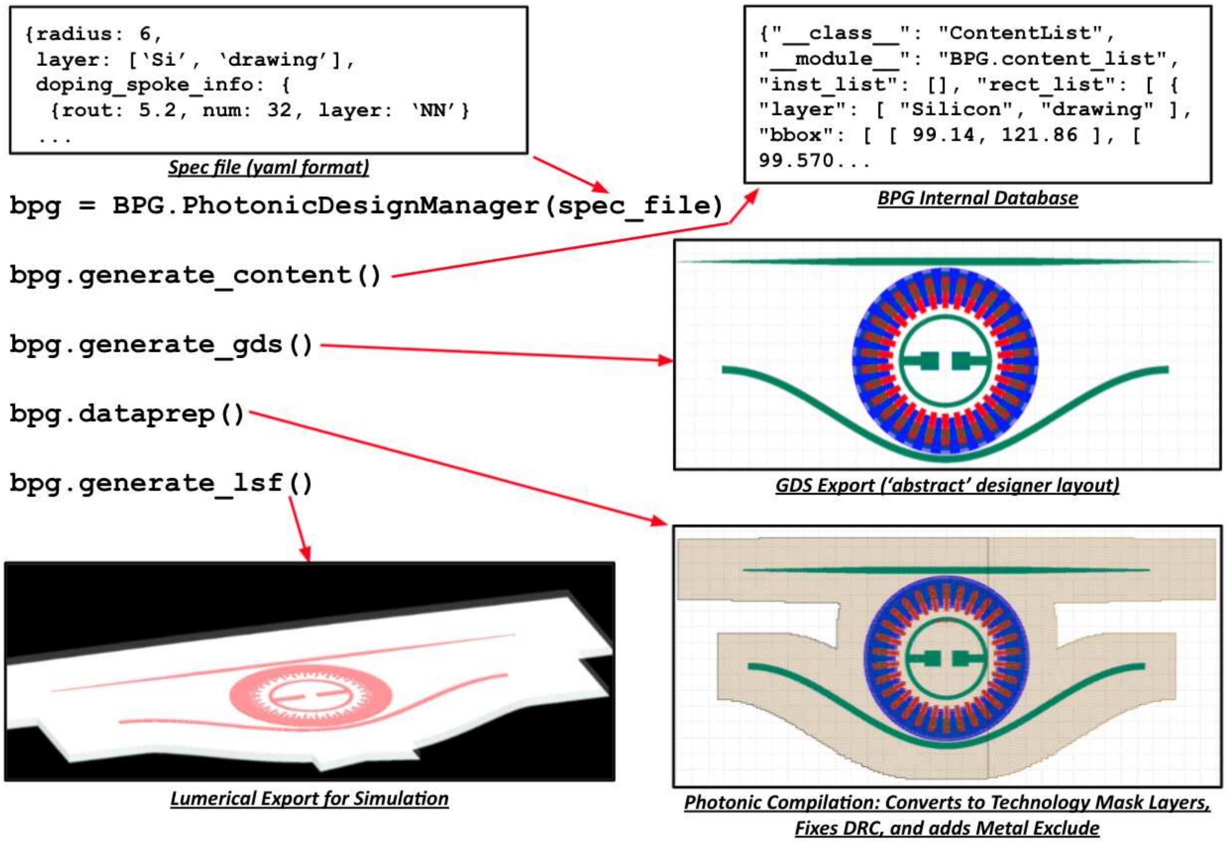

```
{radius: 6,
 layer: ['Si', 'drawing'],
 doping_spoke_info: {
  {rout: 5.2, num: 32, layer: 'NN'}
 ...
```

```
bpg = BPG.PhotonicDesignManager(spec_file)
bpg.generate_content()
bpg.generate_gds()
bpg.dataprep()
bpg.generate_lsf()
```

```
{"__class__": "ContentList",
"__module__": "BPG.content_list",
"inst_list": [], "rect_list": [ {
"layer": [ "Silicon", "drawing" ],
"bbox": [ [ 99.14, 121.86 ], [
99.570...
```

Figure 2.2: Sample design flow within the BPG framework. A top-level script creates a `PhotonicDesignManager` based on the user-provided specifications. The design manager can then, for example, create the internal representation of the layout, export to GDS, call the *Photonic Compiler* to convert the abstract layout into foundry layers, and export a simulation setup to Lumerical.

2.3 Layout Generation and Generator Based Design

BPG encourages a generator-based approach to designing photonic layouts. Rather than having designers hand-craft a final layout for every possible implementation of a given block through a GUI, the generator design approach requires that designers encode their intent as a generalized algorithm with a set of input user specifications. By doing this, the design flow is reproducible, automatically documented through code, and can be parameterized to be used in a wide variety of circumstances.

While PCells embrace a similar philosophy, we seek to extend them in several key ways. First, the BPG framework encourages and enables technology-agnostic design. By allowing

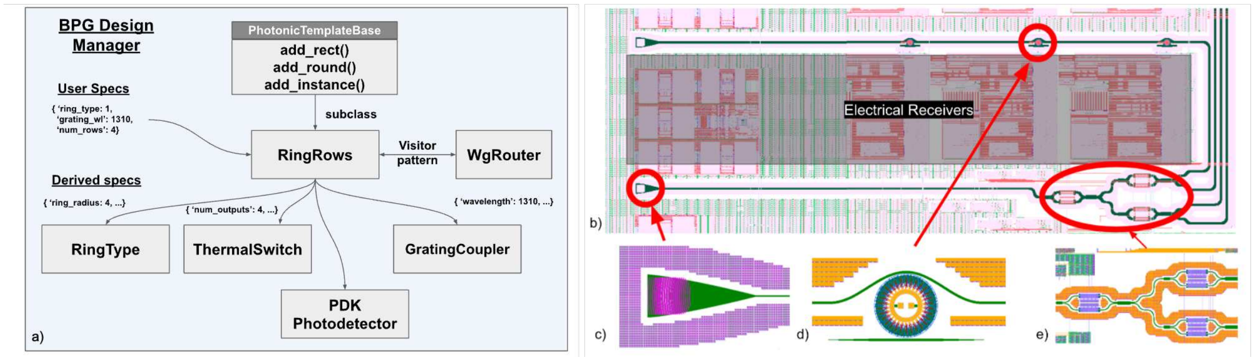

Figure 2.3: a) Example structure for a ring row photonic layout. The top level `RingRow` class subclasses `PhotonicTemplateBase`, which by inheritance gives it access to all of the primitive shape and hierarchy creation methods. Using the specifications provided by the user, `RingRow` then dynamically creates and instantiates all the different component types. These components can themselves be generators which subclass `PhotonicTemplateBase` such as `RingType` and `ThermalSwitch`, or they can be standalone PDK components imported from GDS. Finally, all of these components are assembled and routed together using `WgRouter`. b) Generated layout implementation of a ring row in GF45RFSOI [15]. c-e) Callouts of (c) grating coupler, (d) ring resonator, and (e) thermal switch tree, emphasizing the complex geometry required in photonic structures.

generator authors to write code for an abstract technology, it generalizes the applicability of a single generator to any number of platforms. This approach is discussed further in Section IV. Next, through BPG, generators have a very close connection with any optical simulator of choice. By leveraging this close connection, it is possible to automatically adjust and optimize the parameters for a specific technology that are not known when the generator is written.

BPG is built on top of Berkeley Analog Generator (BAG) [16], a generator-based framework for creating schematics, layouts, and testbenches for analog and mixed signal electrical circuits. BPG adapts and extends BAG to provide the underlying hierarchy management framework as well as new procedures required for photonic design. One of the key additions made by BPG is support for complex, free-form, polygon-based geometries used in photonic components (Fig. 2.3b-e). BPG is fully compatible with electronic circuit layout generators written for BAG, enabling easy co-design of circuits and photonics in monolithically integrated processes from within a single environment. This co-design of electronics and photonics has been leveraged to create components such as compact thermal optical switches [15]. In addition, the integration with BAG enables use of the complex wiring tools that are available and commonly used for analog circuit designs.

`PhotonicTemplateBase` is BPG's primary Python abstract base class that provides a common interface for photonic layout generators, and encapsulates concrete methods for creating and instantiating designs.

The `PhotonicTemplateBase` low level API contains methods that allow the designer to manipulate primitive geometry and layout objects. Methods such as `add_polygon`, `add_rect`, and `add_round` can be used to draw unrestricted primitive geometry objects. BPG supports polygons with free-form edges, and vertices on a quantized user-defined resolution grid. The `add_instance` method can be used to instantiate other `PhotonicTemplateBase` objects within the current layout at a desired location and orientation. BPG supports any-angle instancing (as opposed to restricting to 90 degree cardinal orientations), with intelligent caching that re-computes the generator for an instance only when needed, reducing memory and computation.

Designers can utilize the `add_photonic_port` method to create a `PhotonicPort` object within the layout. A `PhotonicPort` is a BPG primitive object that records, among other information, a location, angle, orientation, width, layer, and name. `PhotonicPorts` can be strategically placed at important locations in the photonic devices, such as terminals of the input and output waveguides, to demarcate locations that can later be used for automated connectivity and abutment. `PhotonicPorts` can also serve as location markers during photonic testbench generation and can be extracted from the design to provide I/O location and device information during testing.

The higher-level API provided by `PhotonicTemplateBase` allows designers to easily assemble subcomponents into a larger, hierarchical design. Methods like `add_instance_port_to_port` can be used to abut two photonic ports, automatically performing any required translation or rotation. Finally, `PhotonicTemplateBase` provides an abstract method `draw_layout` which is implemented by subclasses to define the layout for a particular system or component.

To enable easy connectivity and scalability of designs, BPG provides a semi-automated waveguide router class, `WgRouter`. This router is capable of connecting two ports using straight waveguide routes, parameterized turns (including circular and Euler), and ‘S’-bends. The router keeps track of the overall route length as the route is drawn, so that length matching can be performed. In addition, a waveguide bus fanout router utility is provided to automatically fan out arrays of waveguides to target offsets, ensuring maximal spacing between waveguides and that no waveguide crossings occur. Since this functionality is used and extended in many generator classes, `WgRouter` is implemented as a plugin, rather than additional methods of `PhotonicTemplateBase`. This allows `WgRouter` to use the visitor design pattern to access `PhotonicTemplateBase` methods and create complex assembled layouts, without increasing complexity of `PhotonicTemplateBase` (requiring multiple inheritance), and without requiring large specification dictionaries to be passed around to complete the routing tasks.

Foundry provided or pre-existing IP blocks can be encapsulated using the `GDSImport` subclass of `PhotonicTemplateBase`. By adding `PhotonicPorts` at the inputs/outputs of the block, the device can be treated within the hierarchy as any native BPG-created block, and is able to be automatically instantiated, abutted, and rotated using BPG’s assembly methods.

These features allow designers to manage the complexity of large-scale systems, such as a WDM ring row (Fig. 2.3). With this methodology, it is simple for users to change high level specifications, like ring types, number of rings, and wavelength targets, and have the generator automatically design and assemble the layout.

2.4 Technology Compilation and Process Portable Design

2.4.1 Process Portability

To enable process portability, BPG provides an abstract `PhotonicTechInfo` class. This class contains technology and process parameters required to abstract away hard-coded technology-related constants from layout generators. The `PhotonicTechInfo` class is implemented once per process by the foundry, PDK provider, or designer. In addition to basic design rules such as minimum width and space, via sizes and enclosures, and area constraints, `PhotonicTechInfo` also supports default design-related parameters, such as default waveguide routing layers and widths. Layout generators can then access these technology parameters using a standardized API. In this way, designers can abstract away basic technology-specific parameters (for example, by calling `PhotonicTechInfo.wg_layer`, rather than hard coding a layer), and can re-run the same layout generator using different `PhotonicTechInfo` technology plugins to regenerate the layout in multiple processes.

To further enable process portability, designers are encouraged to use ‘abstract’ design layers, such as ‘waveguide’, ‘nitride’, ‘undoped silicon’, or ‘n_doping’, when implementing the design. In this way, the layout generator captures the designer’s intent, rather than the obfuscating minutia of mask design required in a particular process. Thus, by using technology agnostic intent layers, a layout generator can be reused across processes, with subsequent operations ‘compiling’ the abstract design into a particular technology.

2.4.2 Photonic Compiler

BPG utilizes a *Photonic Compiler* to convert the layout geometry from the internal database representation to external formats, for example GDS. During the compilation process, the abstract designer layers are mapped to mask layers that the foundry requires to fabricate the structure. The compilation procedure utilizes a series of ordered Boolean layer operations (and, or, xor) and polygon manipulation (growth, shrink, snap, Manhattanize) steps, called *Dataprep* (Fig. 2.4). This *Dataprep* routine is standardized per technology, and is provided as part of the technology plugin.

The *Dataprep* routine can provide significant functionality beyond direct layer mapping. First, *Dataprep*’s layer and polygon operations can automatically add utility layers required by the foundry, such as fill-exclude, marker layers around photonic shapes, or create negative mask regions for partially etched silicon, removing these implementation level concerns from

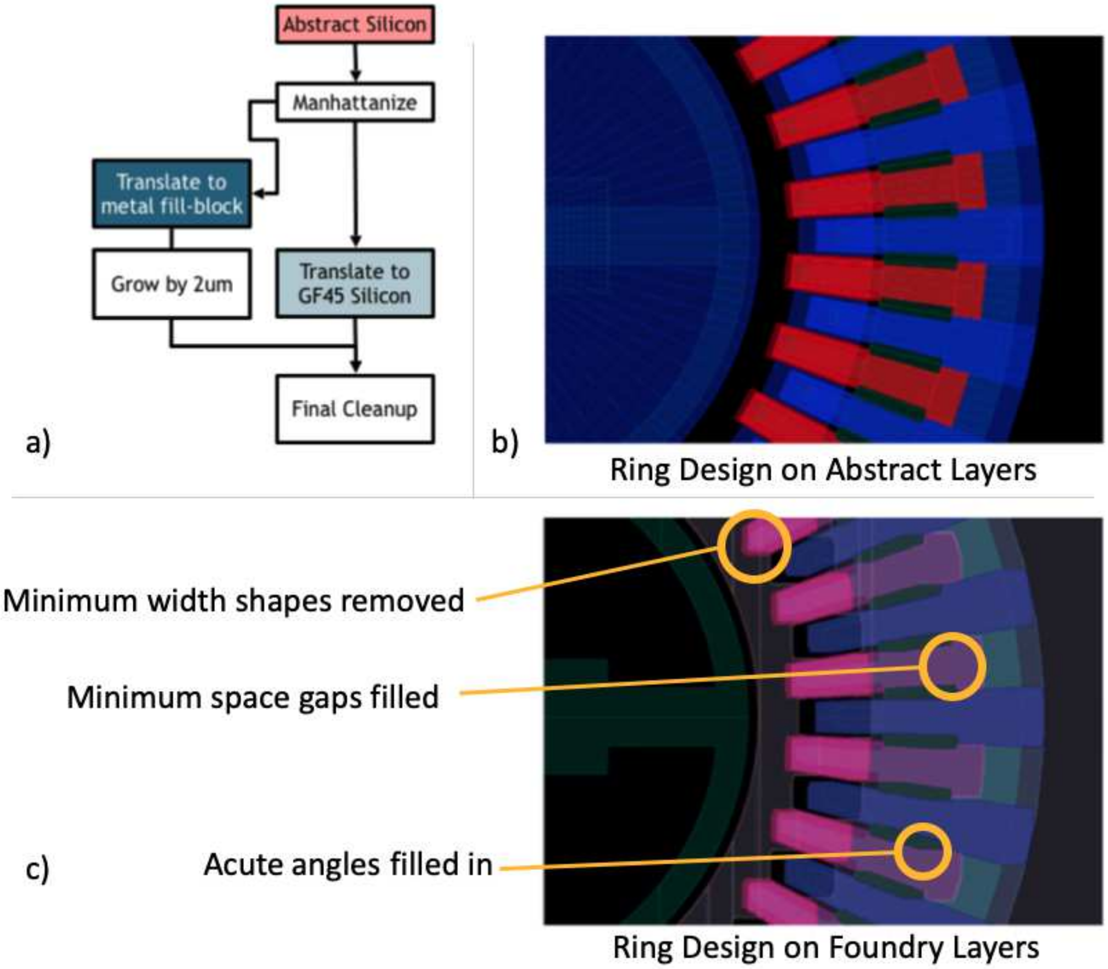

Figure 2.4: a) Sample *Dataprep* routine, showing the operations performed on shapes on the 'silicon' designer layer. In this example process, the silicon shapes are Manhattanized (de-angled) to a user specified grid. In parallel, a 2μm larger fill exclude is generated around the silicon geometry. Finally, these shapes are mapped onto the appropriate foundry layers. b) Sample of a ring modulator in GF45RFSOI, showing the 'abstract' designer layers before *Dataprep*. c) Sample of a ring modulator in GF45RFSOI, showing the foundry layers after *Dataprep*. Callouts indicate several types of DRC violations that are resolved in the *Dataprep* process.

the designer. *Dataprep* geometry manipulation can also be utilized for automatic removal of DRC violations [17]. Sequential 'over-of-under' and 'under-of-over' sizing operations remove free-form minimum width and space violations, respectively [17]. BPG provides a template for *Dataprep* routines, with a standardized geometry 'instruction set' that includes the add, subtract, rough-add, Manhattanize, and, xor, and snap operations, and regex layer parsing. Finally, specific regions in the design (such as foundry IP cells) can be excluded from standard *Dataprep* routine through the use of marker layers and appropriate Boolean subtraction operations.

Utilizing the *Photonic Compiler* to automate DRC correction enables vastly more complex and process portable layout generators. 'Correct by construction' methodologies, which force the designer to produce DRC clean layouts within the layout generator, are not sustainable in advanced process nodes, where the 1000's of DRC rules make even simple curvilinear photonics elements challenging to clean. As an example, for a ring modulator designed in GF45RFSOI [18], a direct mapping of the 'designer intent' geometry to the foundry layers results in tens of thousands of non-waivable DRC violations. However, applying the *Dataprep* routine results in zero remaining non-waivable DRC violations.

2.4.3 Photonic Compiler Implementations

Through BPG's plugin architecture, the computation backend can be customized as desired; however, an open source implementation using gdspy [10] as the computation backend is included, and an ultra-fast backend based on Mentor Graphics's (Siemens EDA) Calibre engine [19] has been implemented and used for wafer-scale photonic compilation. As an example, a 5.5 mm x 8.9 mm electro-optic transceiver IC in GF45RFSOI featuring over 160 ring modulator and detector devices, as wells as 100's of mm of curvilinear waveguide routing and many grating couplers, was generated in less than 2 minutes, and was compiled into a fully DRC clean output using the Calibre *Dataprep* backend in 30 minutes [18].

2.5 Optical Simulation

BPG enables robust and convenient optical device design and characterization through photonic testbench generators. While current work has focused on integration with Lumerical [20], one of the industry leading photonic device design tools, BPG's open plugin framework can be adapted to support other third-party software by simply implementing a standard Python interface between these tools and BPG.

BPG's `LumericalTB` class provides a framework for generating re-usable testbenches. The DUT's generator and specifications are passed to the `LumericalTB`, which automatically instantiates the device. The DUT's `PhotonicPorts` can be accessed to correctly place access waveguides to ensure the proper mode is launched. BPG supports multiple simulation objects, such as simulation boundaries, mode sources, and various optical monitors. In addition, direct Lumerical Script commands can be injected into the testbench using code objects. Within the testbench generator, designers specify which results should be saved from Lumerical for post processing within BPG or using an external tool. Because the testbench generator can access properties of the DUT and of the technology plugin, the same testbench generator can be reused across multiple devices and technologies; for example, a

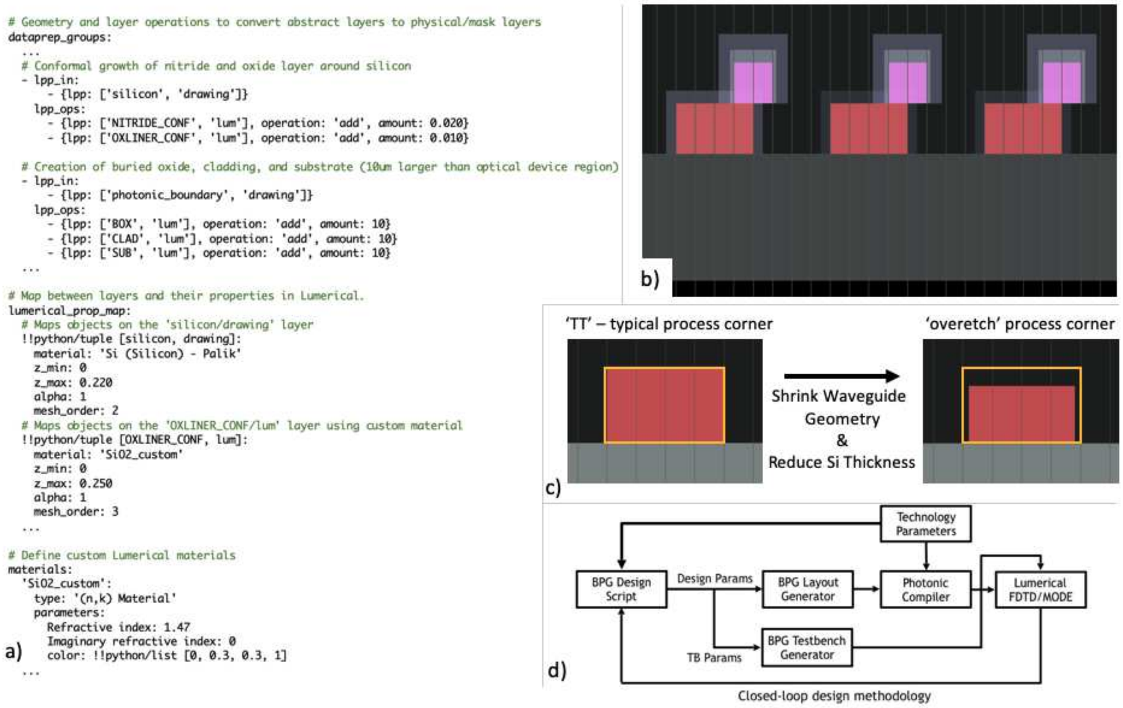

```
# Geometry and layer operations to convert abstract layers to physical/mask layers
dataprep_groups:
  ...
  # Conformal growth of nitride and oxide layer around silicon
  - lpp_in:
      - {lpp: ['silicon', 'drawing']}
    lpp_ops:
      - {lpp: ['NITRIDE_CONF', 'lum'], operation: 'add', amount: 0.020}
      - {lpp: ['OXLINER_CONF', 'lum'], operation: 'add', amount: 0.010}

  # Creation of buried oxide, cladding, and substrate (10um larger than optical device region)
  - lpp_in:
      - {lpp: ['photonic_boundary', 'drawing']}
    lpp_ops:
      - {lpp: ['BOX', 'lum'], operation: 'add', amount: 10}
      - {lpp: ['CLAD', 'lum'], operation: 'add', amount: 10}
      - {lpp: ['SUB', 'lum'], operation: 'add', amount: 10}
  ...

# Map between layers and their properties in Lumerical.
lumerical_prop_map:
  # Maps objects on the 'silicon/drawing' layer
  !!python/tuple [silicon, drawing]:
    material: 'Si (Silicon) - Palik'
    z_min: 0
    z_max: 0.220
    alpha: 1
    mesh_order: 2
  # Maps objects on the 'OXLINER_CONF/lum' layer using custom material
  !!python/tuple [OXLINER_CONF, lum]:
    material: 'SiO2_custom'
    z_min: 0
    z_max: 0.250
    alpha: 1
    mesh_order: 3
  ...

# Define custom Lumerical materials
materials:
  'SiO2_custom':
    type: '(n,k) Material'
    parameters:
      Refractive index: 1.47
      Imaginary refractive index: 0
      color: !!python/list [0, 0.3, 0.3, 1]
  ...
```

Figure 2.5: a) Sample Lumerical *Dataprep* routine for a dummy process. The `dataprep_groups` section defines geometry manipulation and layer operations. The `lumerical_prop_map` section defines how layers map to Lumerical materials, thicknesses, and mesh ordering. The `materials` section allows custom materials for the technology to be defined. b) Sample output of a grating coupler that models a foundry process which includes conformal liners around the silicon (red) and polysilicon (pink) grating teeth. The only user-defined geometry are the silicon and polysilicon grating elements. All liners and background material are automatically generated through the *Dataprep* routine. c) Example of two 'photonic process corners'. Different *Dataprep* recipes, with adjusted parameters reflecting 'typical' and 'overetched' process corners, run on the same designer geometry to produce different simulation outputs. d) Closed loop design procedure.

generic MxN transmission characterization testbench can be used for multiple devices such as AWGs, MMIs, or directional couplers. Testbench reuse enables more robust and standardized optical device verification prior to fabrication. Furthermore, codifying the testbench as a generator reduces the possibility of introducing mistakes compared to manually recreating the supporting geometry and simulation objects.

Upon testbench generation, the *Photonic Compiler* is used to convert the DUT and testbench geometry into Lumerical Script code, which can be run via a standard Lumerical workflow. The DUT geometry is converted from the same internal database that creates the tapeout mask outputs; thus, the designer can ensure there is no mismatch in version or parameters between what is simulated and what is fabricated. For export into Lumerical (or other optical simulators), rather than producing layers that correspond to tapeout masks, the *Dataprep* routine can instead be customized to output layers that model the physical structures present upon device fabrication. This conversion again allows arbitrary geometric and Boolean layer manipulation, which enables complex foundry flows to be modeled accurately.

For example, in some process flows, conformal layers (such as oxides or nitrides) are grown over lithographically defined geometry (such as silicon). Figure 2.5 demonstrates how a Lumerical *Dataprep* flow can accurately model such fabrication processes as a geometric oversize of the silicon layer and Boolean addition onto an oxide liner layer. A technology plugin mapping file defines the set of layers and their properties that finally get exported into Lumerical script (Fig. 2.5a). This ease of mimicking process flow allows designers to be confident they are simulating an accurate and complete view of their fabricated devices, without needed to manually specify all the additional non-designed material regions (such as background materials and conformal growth layers) (Fig 2.5b).

In addition to allowing for complicated process modeling, BPG allows customized Lumerical *Dataprep* routines to support ‘photonic process corners’, in which growth or shrink operations and changes to thickness or material parameters can be used to model process drift, over- and under-etch, and other fabrication imperfections (Fig. 2.5c). As photonic foundries develop further statistical models, BPG’s framework can enable robust, cross-corner photonic verification through PDK-provided variation parameters.

In a standard optical design workflow, BPG’s testbench generators can be used to quickly and confidently produce complex Lumerical simulation geometries. Designers can easily update layout parameters for their DUT, and by regenerating the testbench, all monitors, sources, and domains are automatically moved to match the new geometry. Finally, the results from the optical simulation can be fed back into Python to create a closed-loop design methodology (Fig. 2.5d). Many Python libraries exist (such as SciPy) to enable intelligent design space exploration and optimization.

2.6 Electro-optic Co-Simulation and Verification

Co-simulation is a critical aspect of system design to verify the behavior of the entire electro-optic system. In the electrical circuit domain, designers create visual schematics or netlists out of circuit primitives such as resistors, capacitors, and transistors. For photonic integrated circuits, the optical primitives comprise compact models of devices that contain extracted behavioral parameters. BPG uses schematic optical device primitives from a Verilog-A electro-optic co-simulation toolkit [21]. These primitives model the time-domain behavior of optical components (both forward and reverse waves), and can be co-simulated with standard electrical components within the Cadence Virtuoso simulation tool [22]. BPG utilizes the underlying BAG framework’s schematic generator [16] to create Virtuoso schematics

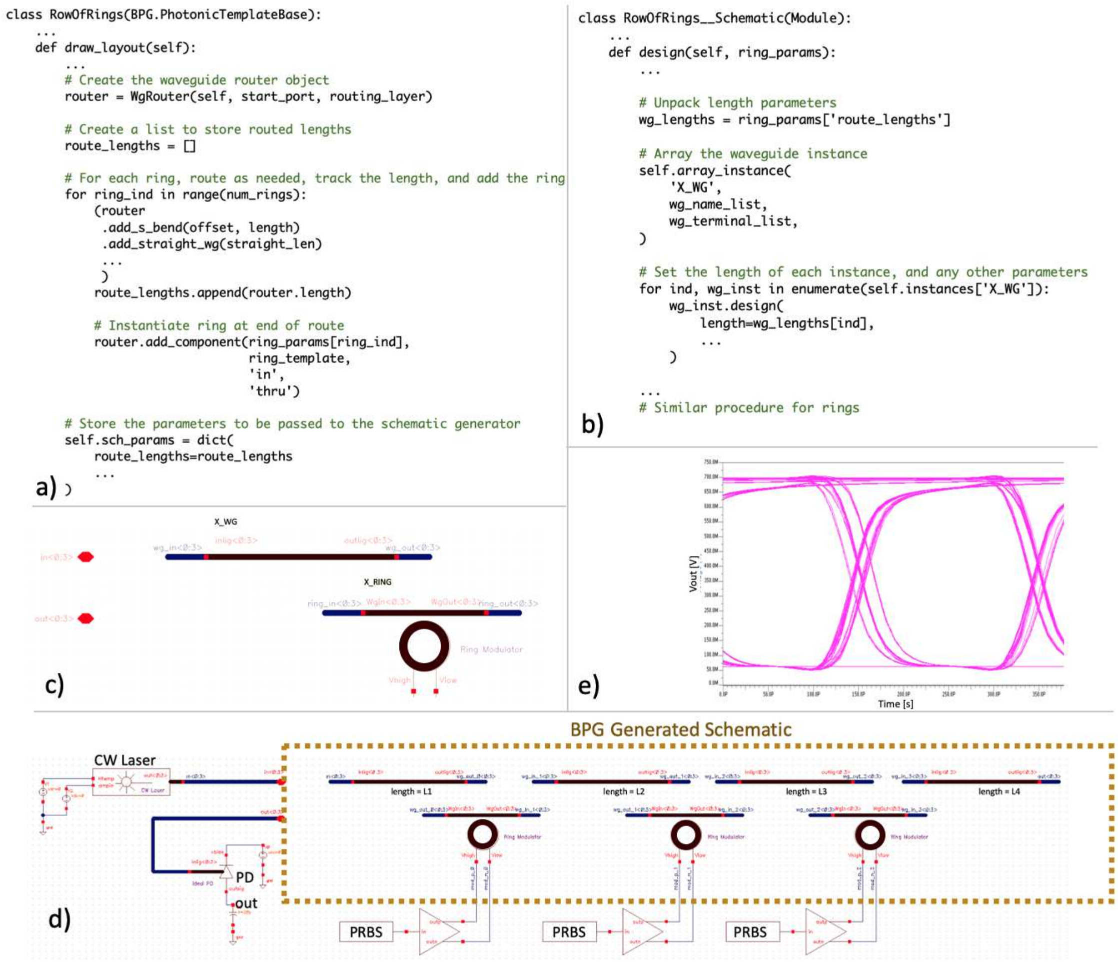

```
class RowOfRings(BPG.PhotonicTemplateBase):
    ...
    def draw_layout(self):
        ...
        # Create the waveguide router object
        router = WgRouter(self, start_port, routing_layer)

        # Create a list to store routed lengths
        route_lengths = []

        # For each ring, route as needed, track the length, and add the ring
        for ring_ind in range(num_rings):
            (router
             .add_s_bend(offset, length)
             .add_straight_wg(straight_len)
             ...
             )
            route_lengths.append(router.length)

            # Instantiate ring at end of route
            router.add_component(ring_params[ring_ind],
                                 ring_template,
                                 'in',
                                 'thru')

        # Store the parameters to be passed to the schematic generator
        self.sch_params = dict(
            route_lengths=route_lengths
            ...
        )
```

```
class RowOfRings__Schematic(Module):
    ...
    def design(self, ring_params):
        ...

        # Unpack length parameters
        wg_lengths = ring_params['route_lengths']

        # Array the waveguide instance
        self.array_instance(
            'X_WG',
            wg_name_list,
            wg_terminal_list,
        )

        # Set the length of each instance, and any other parameters
        for ind, wg_inst in enumerate(self.instances['X_WG']):
            wg_inst.design(
                length=wg_lengths[ind],
                ...
            )

        ...
        # Similar procedure for rings
```

Figure 2.6: a) Layout generator code outline for a row of rings. In the code snippet, a waveguide router is initialized and all the rings are routed and added in-line using the WgRouter class. Note that the route lengths, which might not be known apriori, are computed by the router. The routing lengths, along with other pertinent design parameters, are stored in a `sch_params` property at the end of the generator code. b) Schematic generator for a row of rings. The contents of `sch_params` are passed into the design procedure of the schematic generator. The schematic generator arrays the elements of the schematic template, sets the components' terminal connections, and sets the schematic parameters for each element using the provided design parameters. c) Schematic template for a row of rings. The schematic template consists of the waveguide and ring primitives, which will be arrayed and whose parameters are specified by the schematic generator. d) A BPG generated row of rings schematic, embedded in an electro-optic testbench. The electro-optic components such as CW laser, rings, and photodetector are modeled in Verilog-A. The PRBS generator and electrical drivers are standard electrical elements. e) Sample output eye diagram from the output of the photodetector, showing a functional electro-optical system.

that are capable of simulating both photonic and electronic devices. A schematic generator, similar to a layout generator, is a codified methodology for describing a circuit's schematic connectivity and device parameters. In BPG, physical parameters from the layout generator, in addition to other user or technology provided parameters, can be passed into the schematic generator class to manipulate a template schematic into a particular schematic instance. BPG can again utilize BAG's underlying methodologies to create an electro-optic testbench that instantiates the schematic, and simulates the combined behavior.

As a motivating example, Figure 2.6 shows the electro-optic simulation flow for a ring-based WDM link. At the end of the layout generator, derived physical quantities, which may not be known apriori (such as routing distance between rings or around bends), are combined with user-specified parameters into a python dictionary (Fig. 2.6a). The central design manager then passes these parameters to the schematic generator (Fig. 2.6b), which manipulates the schematic template (Fig. 2.6c) to implement the design. The final schematic can be hierarchically combined with an electronic schematic to produce the final electro optic schematic (Fig. 2.6d). The waveguide lengths in this schematic accurately reflect the physical lengths, which are not known apriori, and which are extracted from the layout generator. A final simulation output of the optical eye diagram is shown in (Fig. 2.6e).

Furthermore, the generated schematic can be combined with custom device and netlist extraction routines to perform photonic-LVS (layout versus schematic) verification. While specific implementations of the layout extraction routines are process specific and often proprietary, such tools have been implemented by the authors in GF45RFSOI, GF Fotonix (a next-generation GlobalFoundries 45nm electronic-photonic process), and Lionix Triplex processes to verify the layout against a simulatable optical schematic. BPG provides plugins to dispatch the LVS routine to the industry standard Mentor Graphics (Siemens EDA) Calibre LVS engine.

In addition to LVS dispatch plugins, BPG provides plugins to support DRC routines using the Mentor Graphics (Siemens EDA) Calibre DRC or KLayout backends.

2.7 Results and Motivating Examples

BPG has been adopted by several research and industry groups, and has been used to design devices and systems in at least five processes: GlobalFoundries' 45RFSOI [23], GlobalFoundries' 45nm Fotonix process [24], LioniX TriPleX [25], Applied Nanotools NanoSOI [26], and AIM Photonics [27]. Designers have used BPG to produce layouts for more than 10 full wafer runs and dozens of individual chips. In this section, we highlight several examples of systems and devices that were enabled by the BPG framework.

BPG's technology agnostic framework and *Photonic Compiler* allows the same design codebase to be reused across multiple processes. For example, the rapid adiabatic coupler introduced in [28] has been fabricated in GF45RFSOI, Applied Nanotools NanoSOI [29], a next-generation GlobalFoundries 45nm electronic-photonic process [30], and LioniX TriPleX (Fig. 2.7a). The same layout generator was used for all devices; the only change to produce these two designs was providing a separate Technology Plugin for each process, and providing appropriate design parameters for each process.

BPG's generator methodology allows for highly flexible and reusable design components. Properly coded generators can take advantage of conditional and looping logic to enable extremely scalable designs. For example, the same binary-tree based 1xN optical switch generator (Fig. 2.7b) can be used to produce 1x4, 1x16, and even 1x512 switch networks. Once coded, multiple instantiations of the parameterized structure can be used without additional design effort.

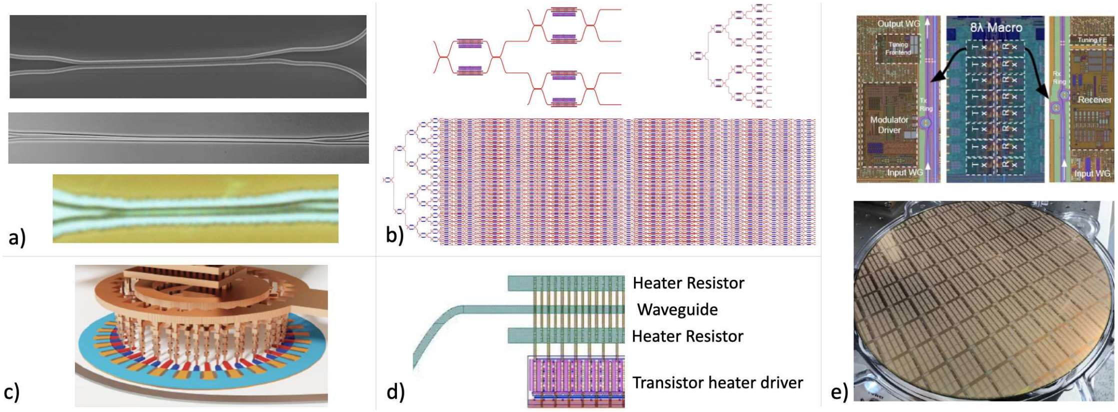

Figure 2.7: a) Three implementations of a rapid adiabatic coupler, implemented in (top) Applied Nanotools NanoSOI [29], (middle) LioniX TripleX, and (bottom) GF45RFSOI. All designs were produced using the same BPG generator. b) 1xN binary switch tree. The same generator is used to generate a 1x4, 1x16, and 1x512 switch. c) High modulation efficiency ring modulator with 30 GHz/V shift [31], implemented in GF45RFSOI. d) Thermal phase shifter with tightly integrated photonics and electronics. A single BPG generator produces both the waveguide and heater geometry, as well as the transistor layout and wiring. The distance between the photonics and electronics is below 3 microns. e) (top) High-speed photonic modulators and ring photodetectors as part of a WDM link [18]. (bottom) BPG generated all photonics components (1000s) on the 300 mm full-wafer run in GF45RFSOI [32].

Seamless integration with electronic devices is enabled through BPG's compatibility with the underlying BAG framework. BAG is a generator-based tool for analog and mixed signal electrical circuits that has been used to produce complex circuits such as ADCs and SerDes transceiver frontends [16]. Using the methods provided by BAG, transistor, resistor, and capacitor based electrical circuits can be generated in a scalable and process portable manner. As example, we show a waveguide heater integrated with its transistor heater drivers only microns away (Fig. 2.7d), with both the electronics and optics generated using a single layout generator. This was achieved by calling a BAG transistor generator class directly from within a BPG generator class. The close integration between BAG and BPG enabled wiring generators to be created to make the connection between the transistors and the photonics. This combined electronic and photonic layout was then verified with Calibre LVS tools before being assembled into a larger design.

BPG has been used for a variety of applications, from large-scale electronic-photonic system-on-chip designs to novel device fabrication. Large scale system-on-chip applications include the design and layout of microring based biomedical and ultrasound detector systems [15, 33]. Novel devices include cryogenic ring modulators and ultra-high shift and FSR rings [34]. Process portable layout generators, such as spoked ring modulator/photodetectors (Fig. 2.7c), have been used to produce highly performant devices, such as 30 GHz/V vertical junction modulators [31]. BPG has been used in novel applications for electro-optic systems, such as cryogenic egress links. Finally, BPG has not just been used in the context of academic research, but has been trusted and verified for use in volume production commercial electro-optic systems [18].

2.8 Conclusion

We presented BPG, a photonic design framework that enables users to craft a workflow encompassing layout, electromagnetic simulation, system simulation, and verification into a robust, automated, and reproducible script. BPG's architectural focus on modularity and extensibility helps support the diverse needs of photonic designers. Whether the goal is to experiment with novel devices that push the boundaries of complex design rules or to design and assemble large electronic-photonic systems for high-volume manufacturing, BPG has the power and flexibility to be customized to each user's specific needs. This has encouraged its use across both research and industry applications.

Given BPG's ability to easily create technology-agnostic generators, it serves as an ideal platform for creating a universal PDK. In the future, we plan to release a generator library for BPG which can be automatically compiled to a wide range of newly emerging photonic platforms.

The BPG framework is fully open source under the BSD-3 license and is available to anyone now [14]. We include several examples of design flows with layout generators and testbenches to jumpstart new users. Plugins to enable interfaces with other tools such as gdspy, KLayout, and Lumerical are also open source and freely available.

Chapter 3

Crosstalk in Wavelength Division Multiplexed Links

Silicon photonic interconnects promise high bandwidth-density, high energy efficiency, and compact integration with electrical transceivers [35, 36]. Such links hold great promise in addressing the I/O data bottleneck that is one of the most critical barriers towards exascale computing [37]. Optical I/O enabled by monolithically integrated silicon photonics has reached datarates above 1 Tbps per chip [7], and up to 8 Tbps in a co-packaged module [2].

One of the key enabling techniques that allows for such high bandwidth density is Wavelength Division Multiplexing (WDM). In WDM schemes, different channels of data are encoded on different wavelengths of light, Fig. 3.1. As target datarates increase, the datarate per channel and number of wavelengths (channels) must increase as well, reducing the wavelength spacing between adjacent channels. Spectral overlap of adjacent channels can cause crosstalk, resulting in reduced eye opening and a degradation in bit error rate (BER).

This chapter addresses the limitations of channel densification in WDM systems. This chapter first provides an overview of WDM link architectures, and the key metrics that channel filters must provide. Next, the static transfer function and several key parameters of microring resonators are derived, in both the spatial domain ‘loop analysis’ framework, and the coupled modes theory (CMT) time-domain framework. The optimal single-ring filter response is determined, and representative examples of different responses for different design targets are shown. In Section 3.4, a modeling framework to evaluate crosstalk and eye closure penalty in WDM links is presented. Section 3.5 presents the analysis results for a single ring drop filter, and provides guidelines when designing WDM links. Section 3.6 extends the analysis to dual-ring drop filters, and it is found that double ring filters can surpass single ring filters in technology processes where the intrinsic quality factor is high enough.

3.1 Overview of WDM Links

In WDM optical links, different channels of data are encoded on different wavelengths of light. Figure 3.1 shows a schematic of a WDM optical link. An external light source provides n distinct wavelengths on a single fiber, each wavelength providing an optical channel for data transmission and reception. Light is coupled from fibers into and out of the transmitter and receiver chips by means of optical couplers (grating couplers or edge couplers). The transmitter (TX) consists of n distinct resonant modulator devices, each tuned to modulate a single wavelength of light. In the schematic, n independent datastreams are driven by electrical drivers onto each TX resonant modulator, which act as multiplexers that combine data onto the common bus waveguide. The receiver (RX) consists of n distinct resonant filter devices, each tuned to a distinct wavelength. The RX filter device act as demultiplexers that separate the independent datastreams onto individual photodetectors and electrical receivers per channel. In Fig. 3.1, the resonant devices are depicted as microring resonators. Examples of ring-based WDM optical links can be found in [7, 35].

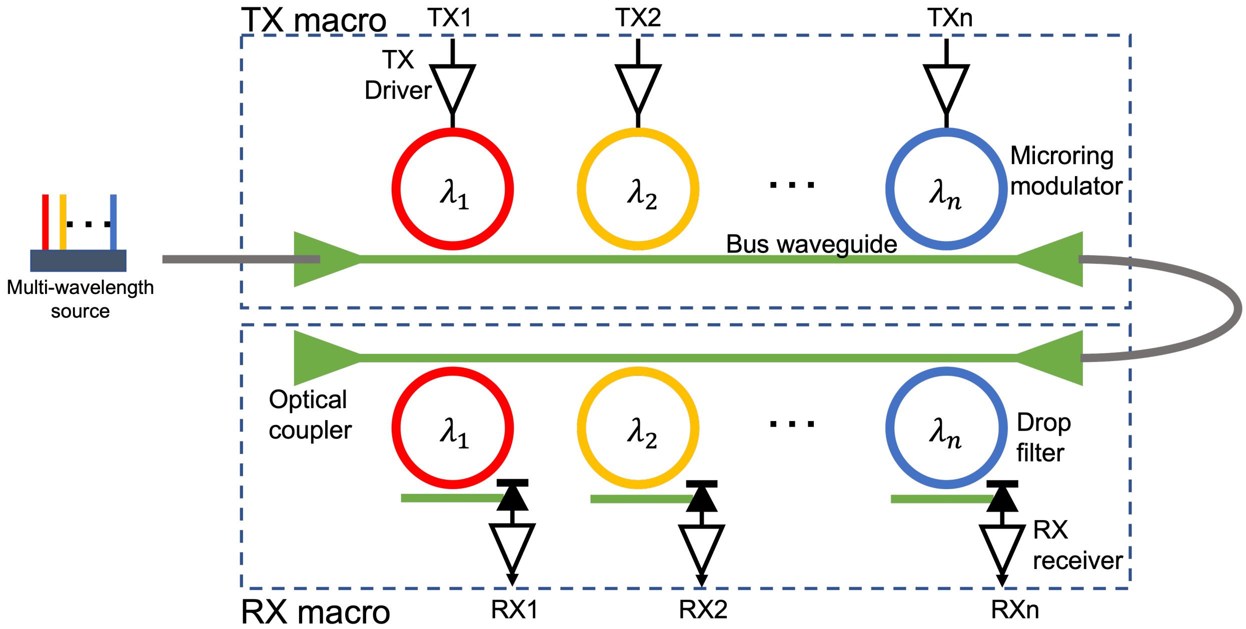

Figure 3.1: Schematic of WDM optical link. An external laser source provides n wavelengths on a single fiber. In the transmit (TX) macro, an array of n resonant devices, acting as modulators which are driven by CMOS transmitters, modulate data on each optical channel. In the receiver macro, an array of n resonant devices, acting as drop filters, each capture a single channel of data. In this schematic, microring resonators are used as both the resonant modulator and filter devices.

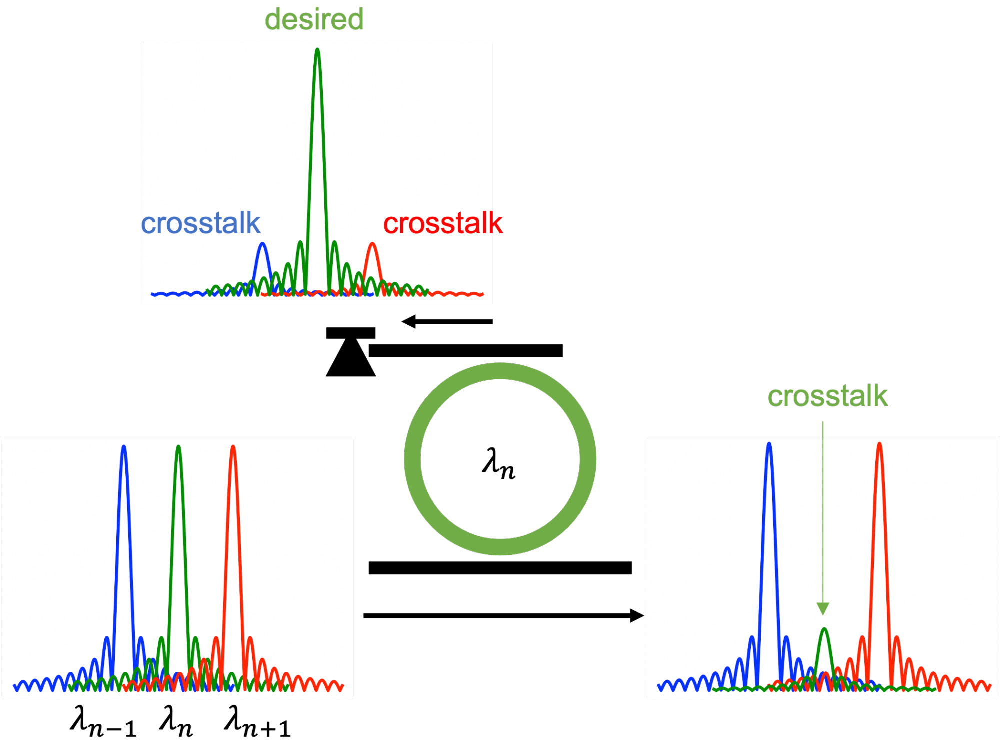

Figure 3.2: Example of crosstalk between channels in the receiver. Spectral content modulated around optical carriers λ_{n-1} and λ_{n+1} is picked up by the resonant filter for a channel centered around λ_n, which causes crosstalk for channel n. In addition, spectral content around λ_n which does not get captured by the channel n filter will act as crosstalk for subsequent channels.

As the optical signal passes through the receiver, each resonant filter 'drops' the energy around a particular wavelength onto the photodetector for that channel. However, energy from the adjacent wavelength channels can also be captured, Fig. 3.2. This is due to the broad filtering response of the channel filter, as well as the broad spectral content of the modulated signals [38], which causes spectral overlap between the filters' spectral response and the adjacent channels' data. In these cases, the adjacent channels act as crosstalk aggressors. In addition, limitations in the filter response cause some energy in channel n to pass through the filter into subsequent channels, thus contributing crosstalk into those channels.

The goal of an ideal drop filter is thus to capture 100% of the energy belonging to a particular channel, remove this content from subsequent filters, and also completely reject the spectral content in adjacent channels. Figure 3.3 shows an example of the filter responses for two drop filters for two adjacent optical channels. Key performance metrics are highlighted:

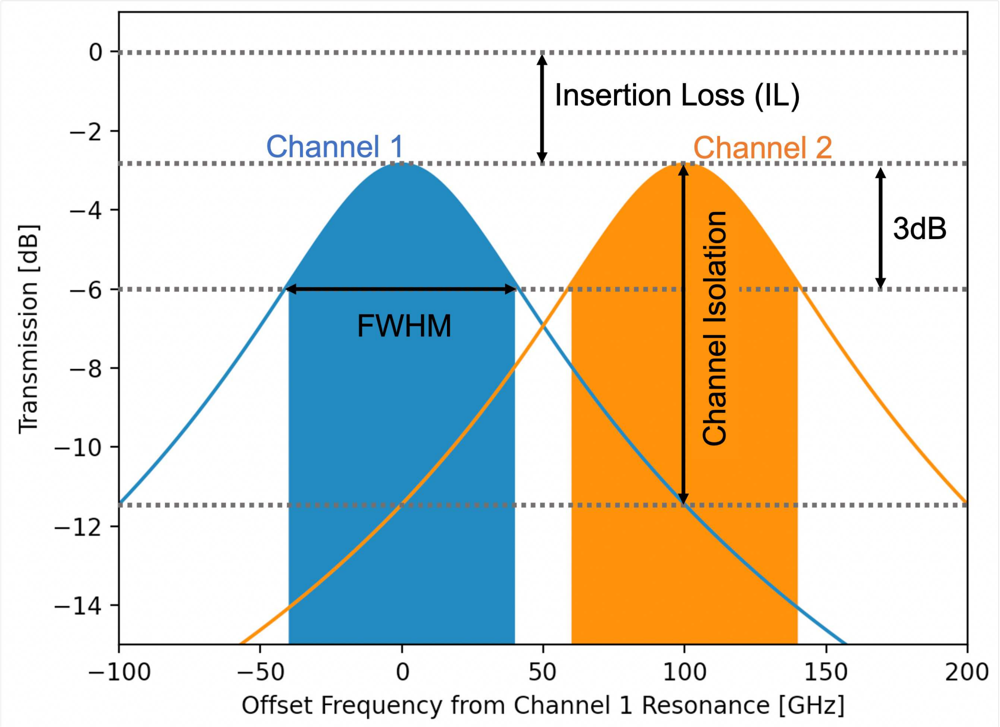

Figure 3.3: Sample filter responses of two drop filters for two adjacent optical channels.

insertion loss (IL), bandwidth (FWHM), and channel isolation. Insertion loss is a measure of the lost energy which is not captured by the filter, at is central resonant frequency, and should ideally be 0 dB. Bandwidth is measured by the full-width half-maximum (FWHM), which is the bandwidth of the filter measured at half its peak power (3 dB below the transmission at the center frequency). The bandwidth of the filter must be large enough such that the spectral content of the signal of interest may be captured without significant attenuation. Note that signals at the extremes of the FWHM bandwidth already suffer 3 dB attenuation. Finally, channel isolation measures the rejection of a filter's response to the energy in the adjacent channel. The channel isolation should ideally be as large as possible, but design constraints on the channel spacing, FWHM bandwidth, and filter order will limit this value.

In the next section, the behavior and pertinent properties of microring filters for use as resonant filter devices will be discussed.

3.2 Microring Filters

Microring filters are attractive elements for WDM communications, due to their compact footprint [39, 40] and sharp spectral response. A microring resonator consists of a looped silicon waveguide coupled to one or more access waveguides, with a die micrograph and

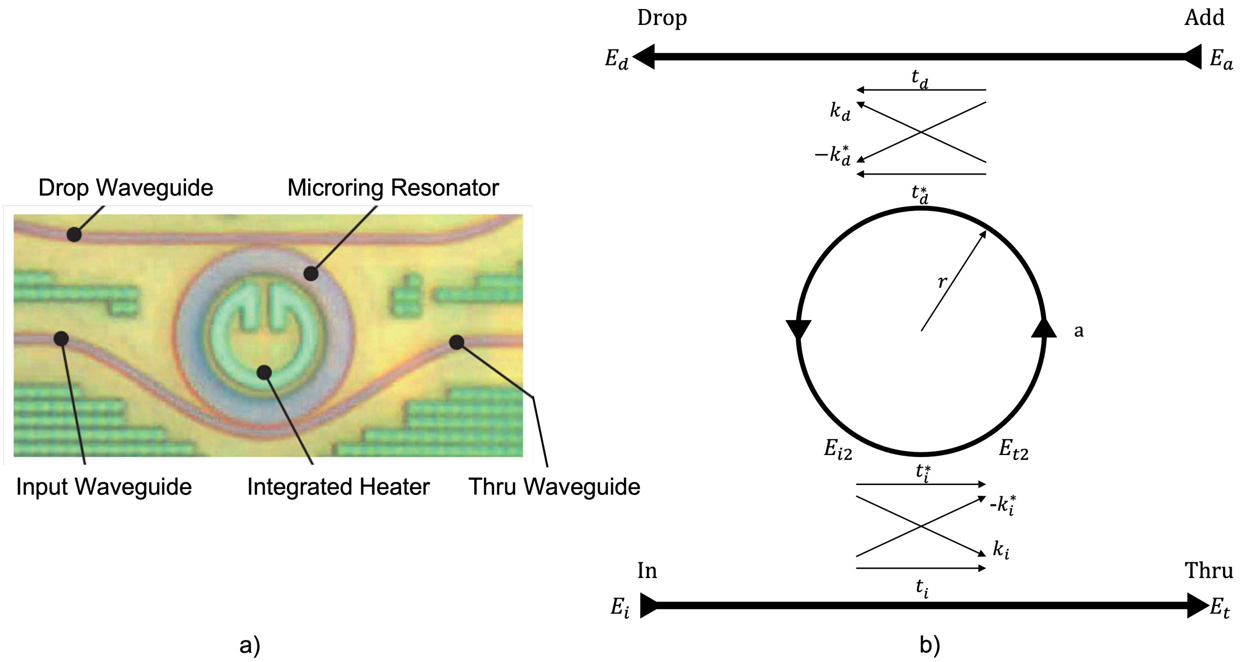

a)

b)

Figure 3.4: a) Die micrograph of a microring resonator (from [36]) in the GlobalFoundries 45nm RFSOI platform [41]. The ring radius is approximately 5 um. b) Schematic of a microring resonator.

schematic depicted in Fig. 3.4. When the wave in the loop accumulates a round trip phase which is an integer multiple of 2π, the waves interfere constructively and the ring is said to be ‘on resonance’. The phase accumulated by the light as it propagates around the ring is expressed as

$$\phi = \beta L = \frac{2\pi}{\lambda} n_{eff} L \tag{3.1}$$

where $L = 2\pi r$ is the circumference of the ring, n_{eff} is the effective index of refraction, and λ is the wavelength. The resonance wavelengths at which the ring is on resonance are found to be

$$\lambda_{res} = \frac{n_{eff} L}{m}, \qquad m = 1, 2, 3, \ldots \tag{3.2}$$

One other important ring parameter is the loss coefficient, a, which is equal to the single-pass amplitude transmission as light propagates around the ring, and captures bend, scattering, and other losses. Under lossless conditions, $a = 1$. a is related to the power attenuation coefficient α [1/m] by

$$a^2 = e^{-\alpha L} \tag{3.3}$$

The loss coefficient of the ring is dependent on the ring waveguide geometry (bend radius, waveguide cross section, etc.) and on the process technology.

Light is coupled into and out of the microring resonators by means of coupling regions. The coupling region has complex amplitude cross-coupling coefficient k and self-coupling coefficient t, which describe the fraction of light coupled from the access waveguide into the ring. Under the assumption that no reflections occur in the coupling region, the transmission matrix is unitary due to the reciprocity of the coupler [42]

$$\begin{pmatrix} E_t \\ E_{t2} \end{pmatrix} = \begin{pmatrix} t & k \\ -k^* & t^* \end{pmatrix} \begin{pmatrix} E_i \\ E_{i2} \end{pmatrix} \tag{3.4}$$

Here, E represents the energy amplitude of light in the waveguide, and is normalized such that $P = |E|^2$ represents the power flowing through a cross section of the waveguide. For lossless couplers, $|k|^2 + |t|^2 = 1$. However, in practical couplers, the coupling strength is strongly dependent on the waveguide-resonator coupling geometry, and proper consideration must be taken when designing ring couplers, to ensure that the desired fundamental mode coupling is achieved, without exciting undesired higher order ring modes [43].

3.2.0.1 Static Ring Response

The static transfer function of a ring resonator can by found from Eqs. 3.1, 3.4

$$E_{t2} = -k_i^* E_i + t_i^* E_{i2} \tag{3.5a}$$

$$E_{i2} = a t_d^* e^{j\theta} E_{t2} \tag{3.5b}$$

$$E_{i2} = a t_d^* e^{j\theta} \left(-k_i^* E_i + t_i^* E_{i2}\right) \tag{3.5c}$$

$$E_{i2} = \frac{-a t_d^* k_i^* e^{j\theta}}{1 - a t_d^* t_i^* e^{j\theta}} E_i \tag{3.5d}$$

$$E_t = t_i E_i + k_i E_{i2} \tag{3.5e}$$

$$E_t = \left(t_i + \frac{-a t_d^* |k_i|^2 e^{j\theta}}{1 - a t_d^* t_i^* e^{j\theta}}\right) E_i = \left(\frac{t_i - a t_d^* e^{j\theta}\left(|t_i|^2 + |k_i|^2\right)}{1 - a t_d^* t_i^* e^{j\theta}}\right) E_i \tag{3.5f}$$

Assuming a lossless coupler,

$$\frac{E_t}{E_i} = \frac{t_i - a t_d^* e^{j\theta}}{1 - a t_d^* t_i^* e^{j\theta}} \tag{3.6}$$

and

$$\frac{E_d}{E_i} = \frac{-k_i^* k_d e^{\frac{j\theta}{2}} \sqrt{a}}{1 - a t_d^* t_i^* e^{j\theta}} \tag{3.7}$$

The transmission power at the thru port is given by

$$P_t = |E_t|^2 = \frac{|t_i|^2 + a^2 |t_d|^2 - 2a|t_i||t_d| \cos\theta}{1 + a^2 |t_i|^2 |t_d|^2 - 2a|t_i||t_d| \cos\theta} \tag{3.8}$$

The power at the drop port is given by

$$P_d = |E_d|^2 = \frac{a|k_i|^2 |k_d|^2}{1 + a^2 |t_i|^2 |t_d|^2 - 2a|t_i||t_d| \cos\theta} \tag{3.9}$$

On resonance, θ is a multiple of 2π, and the power at the through and drop ports is

$$P_{t,res} = \frac{(|t_i| - a|t_d|)^2}{(1 - a|t_i||t_d|)^2} \tag{3.10a}$$

$$P_{d,res} = \frac{a|k_i|^2|k_d|^2}{(1 - a|t_i||t_d|)^2} \tag{3.10b}$$

A condition known as 'critical coupling' occurs when

$$a|t_d| = |t_i| \tag{3.11}$$

In this case, $P_t = 0$. Note that for a ring with loss, which will occur in all physical systems, the two coupling coefficients can always be engineered to achieve zero on-resonance power at the thru port. In the case of a lossless system, $a = 1$, and the critical coupling condition becomes $|t_i| = |t_d|$, that is, symmetric coupling of the input and drop waveguides results in zero on-resonance power at the thru port.

One important parameter of microring resonators is their free spectral range (FSR), defined as the wavelength spacing between two resonances. Because the value of the effective index depends on the wavelength, the FSR must be computed using the group index n_g, defined in Eq. 3.12

$$n_g = n_{eff} - \lambda \frac{\partial n_{eff}}{\partial \lambda} \tag{3.12}$$

Then

$$\frac{\partial \beta}{\partial \lambda} = -\frac{2\pi}{\lambda^2} n_{eff} + \frac{2\pi}{\lambda} \frac{\partial n_{eff}}{\partial \lambda} \tag{3.13a}$$

$$= -\frac{\beta}{\lambda} + \frac{2\pi}{\lambda} \frac{n_{eff} - n_g}{\lambda} \tag{3.13b}$$

$$= -\frac{\beta}{\lambda} + \frac{\beta}{\lambda} - \frac{2\pi}{\lambda} \frac{n_g}{\lambda} \tag{3.13c}$$

$$= -\frac{2\pi}{\lambda^2} n_g \tag{3.13d}$$

As the FSR is the difference in wavelengths between two adjacent resonance conditions,

$$\text{FSR} \cdot \frac{\partial \beta}{\partial \lambda} L = \pm 2\pi \tag{3.14}$$

Thus

$$\text{FSR} = -\frac{2\pi}{L} \frac{1}{\frac{\partial \beta}{\partial \lambda}} = -\frac{2\pi}{L} \frac{1}{-\frac{2\pi n_g}{\lambda^2}} = \frac{\lambda^2}{n_g L} \tag{3.15}$$

Note that the FSR does not depend on the coupling from the ring to the access waveguides. In designing rings for WDM applications, the FSR will dictate the radius of the microring resonators.

An example transmission spectrum of an add-drop microring resonator can be found in Fig. 3.6. The responses are shown across multiple FSRs and close to resonance. Note that the ring in this figure is not critically coupled, and thus has finite extinction at the thru port on resonance.

Another important parameter is the resonance linewidth, which is defined as the full width at half maximum (FWHM) or 3dB bandwidth of the spectral resonance. Using Eqs. 3.7, 3.10b

$$\left|\frac{-k_i^* k_d e^{\frac{j\theta}{2}}\sqrt{a}}{1-at_d^*t_i^*e^{j\theta}}\right|^2 = \frac{1}{2}\frac{a|k_i|^2|k_d|^2}{(1-a|t_i||t_d|)^2} \tag{3.16}$$

Under the assumption of lossless couplers, Eq. 3.16 implies

$$1+a^2|t_d|^2|t_i|^2-2a|t_d||t_i|\cos(\theta) = 2\left(1-a|t_i||t_d|\right)^2 \tag{3.17}$$

Under a small angle assumption for θ, suitable for microring resonators with sharp linewidths relative to their FSR, this becomes

$$\cos\theta \approx 1-\frac{\theta^2}{2} \tag{3.18a}$$

$$1+a^2|t_d|^2|t_i|^2-2a|t_d||t_i|\left(1-\frac{\theta^2}{2}\right) = 2\left(1-a|t_i||t_d|\right)^2 \tag{3.18b}$$

$$1+a^2|t_d|^2|t_i|^2-2a|t_d||t_i|+\frac{\theta^2}{2}2a|t_d||t_i| = 2+2a^2|t_i|^2|t_d|^2-4a|t_i||t_d| \tag{3.18c}$$

$$\theta = \frac{1-a|t_i||t_d|}{\sqrt{a|t_d||t_i|}} \tag{3.18d}$$

Using Eqs. 3.1, 3.13a, Eq. 3.18a implies

$$\text{FWHM} = \frac{\lambda_{res}^2\left(1-a|t_i||t_d|\right)}{\pi n_g L\sqrt{a|t_d||t_i|}} \tag{3.19}$$

Two other important ring parameters are the quality factor Q and finesse F. The quality factor measures the sharpness of the resonance relative to the resonance wavelength, while the finesse measures the sharpness relative to the FSR.

$$\text{Quality factor} = Q = \frac{\lambda_{res}}{\text{FWHM}} = \frac{\pi n_g L\sqrt{a|t_d||t_i|}}{\lambda_{res}\left(1-a|t_i||t_d|\right)} \tag{3.20}$$

$$\text{Finesse} = F = \frac{\text{FSR}}{\text{FWHM}} = \frac{\pi\sqrt{a|t_d||t_i|}}{1-a|t_i||t_d|} \tag{3.21}$$

The physical meaning of quality factor is the number of oscillations of the electric field before energy in the microring resonator is depleted, lost to internal losses and to the access waveguides, to $1/e$ of the initial energy in the resonator. Finesse, to a factor of of 2π, represents the number of round trips made by light around the ring before its energy is reduced to $1/e$ of its initial value [44]. Note that $F = \frac{Q}{m}$, where m is the resonance mode order (the number of wavelengths that fit in the circumference of the ring at a particular resonance wavelength).

The quality factor can be characterized as either the *loaded* or *unloaded* (or 'intrinsic') quality factor. Unloaded quality factor considers only the losses intrinsic to the ring resonator itself, when access waveguides are absent. Such losses can be due to bending loss, sidewall scattering, and material losses [39, 43, 45]. Under these conditions, $|t_i| = |t_d| = 1$, thus

$$Q_0 = Q_{unloaded} = \frac{\pi n_g L \sqrt{a}}{\lambda_{res}\left(1-a\right)} \tag{3.22}$$

The loaded quality factor includes coupling losses to the access waveguides. The loaded quality factor will always be lower than the unloaded quality factor. Unless otherwise specified, quality factor refers to the loaded quality factor.

One implication of the resonant nature of rings is energy buildup within the ring. From Eq. 3.6,

$$\frac{E_{ring}}{E_i} = \frac{-ak_i^* t_d^* e^{j\theta}}{1 - at_d^* t_i^* e^{j\theta}} \tag{3.23}$$

and the buildup factor is

$$B = \left|\frac{E_{ring}}{E_i}\right|^2 = \frac{a^2\left(1-|t_i|^2\right)|t_d|^2}{1 + a^2|t_i|^2|t_d|^2 - 2a|t_i||t_d|\cos\theta} \tag{3.24}$$

On resonance,

$$B_{res} = \frac{a^2\left(1-|t_i|^2\right)|t_d|^2}{\left(1-a|t_i||t_d|\right)^2} \tag{3.25a}$$

$$\underset{a=1,|t_i|=|t_d|=|t|}{=} \frac{|t|^2}{1-|t|^2} = \frac{1}{\pi}\text{Finesse} \tag{3.25b}$$

On resonance, the buildup factor can be quite significant, with the energy and intensity within the ring significantly higher than that of the input waveguide. This energy buildup can lead to self heating effects, which cause a change in the resonance linewidth shape, and can result in non-stable thermal feedback conditions [46].

3.2.0.2 Coupled Mode Theory: Time Domain

The coupled modes theory (CMT) time-domain formalism provides an alternative and elegant view of microring resonators, which is useful when designing filters for wavelength division multiplexed systems. In the CMT framework, adapted here from [40, 47], the ring is considered a lumped oscillator that supports energy amplitude $e(t)$ which is normalized

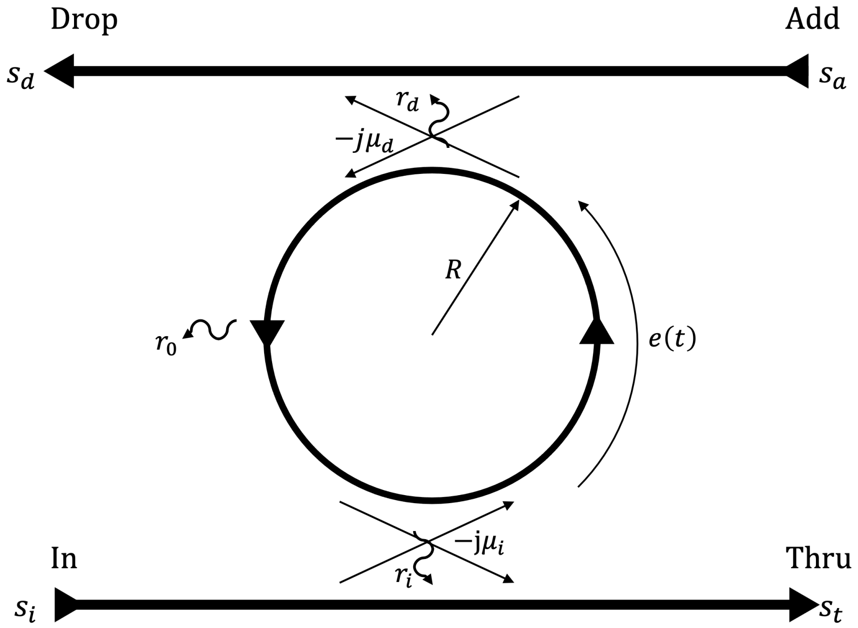

Figure 3.5: Schematic of microring resonator in the CMT framework. Loss rates r_0, r_i, and r_d represent energy amplitude loss rates.

such that $|e(t)|^2$ represents the total energy stored in the ring. The ring can also be considered to support a travelling wave with amplitude $E(t)$, such that $P(t) = |E(t)|^2$ represents the total power flowing through a cross section of the ring waveguide at time t. The energy and power within the ring are related by

$$p(t) = |e(t)|^2 = P(t)\frac{n_g L}{c} = |E(t)|^2\frac{n_g L}{c} \tag{3.26}$$

The ring has resonance frequency ω_0, and an amplitude decay time constant τ, such that $\frac{1}{\tau}$ represents the rate of amplitude decay. The decay time constant includes power lost to intrinsic losses ($\frac{1}{\tau_0} = r_0$), power coupled to/from the input waveguide ($\frac{1}{\tau_i} = r_i$), and power coupled to/from the drop waveguide ($\frac{1}{\tau_d} = r_d$). The decay rates add, such that

$$\frac{1}{\tau} = \frac{1}{\tau_0} + \frac{1}{\tau_i} + \frac{1}{\tau_d} \tag{3.27}$$

The ring is again coupled to two access waveguides, an input/thru waveguide and an add/drop waveguide, as in Fig. 3.5.

The time evolution of the energy in the ring oscillator thus follows the following behavior

$$\frac{d}{dt}e(t) = \left(j\omega_0 - \frac{1}{\tau}\right)e(t) - j\mu_i s_i(t) \tag{3.28}$$

Here, $s_i(t)$ represents the energy amplitude, normalized such that $|s_i(t)|^2$ is the power flowing through the cross section of the input waveguide, and μ_i represents the coupling strength between the input waveguide and ring. The $-j$ phase factor is arbitrarily chosen by the choice of reference planes when considering the coupling response. $-j$ is selected to align most closely with spatial mode-coupling phase conventions.

The transmitted wave can be written by inspection as

$$s_t(t) = s_i(t) - j\mu_i e(t) \tag{3.29}$$

The power at the drop port can be written as

$$s_d(t) = -j\mu_d e(t) \tag{3.30}$$

and should obey $|s_d(t)|^2 = |s_i(t)|^2 - |s_t(t)|^2$ by power conservation.

The coupling coefficient μ can be related to the spatial power coupling coefficient k (from the static 'loop equation' analysis above (Fig. 3.4 and Eq. 3.4)) by considering energy conservation in the power and energy views of the decay rate. Recall that $|k|^2$ represents the fraction of power coupled from the ring to the waveguide, and vice versa. In the power domain, the travelling wave in the ring of amplitude $E(t)$ couples into the amplitude wave of an access waveguide $s(t)$ such that, from Eq. 3.26,

$$|s(t)|^2 = |k|^2 P(t) \tag{3.31a}$$

$$= |k|^2 |E(t)|^2 \tag{3.31b}$$

$$= |k|^2 \frac{c}{n_g L} |e(t)|^2 \tag{3.31c}$$

In the energy domain, consider a ring which is coupled to a single waveguide such that the decay rate of the energy due to just this waveguide coupling is $\frac{1}{\tau_i}$ and all other losses (such as intrinsic loss) are neglected (i.e. $\frac{1}{\tau_0} = 0$). If the ring is excited to initial energy $|e_0|^2$ and no incident signal is present ($s_i = 0$), then from Eq. 3.28,

$$e(t) = e_0 e^{j\omega_0 t} e^{-\frac{t}{\tau_i}} \tag{3.32a}$$

$$|e(t)|^2 = |e_0|^2 e^{-\frac{2t}{\tau_i}} \tag{3.32b}$$

The power leaving the ring is equal to the rate of change in the energy of the ring. Thus, equating the derivative of Eq. 3.32a to Eq. 3.31a and noting that $s_t(t) = -j\mu_i e(t)$ when $s_i = 0$,

$$\mu_i^2 = |k_i|^2 \frac{c}{n_g L} = \frac{2}{\tau_i} \tag{3.33}$$

By similar reasoning, the intrinsic decay rate can be related to the amplitude loss coefficient a

$$\frac{2}{\tau_0} = \left(1 - a^2\right) \frac{c}{n_g L} \tag{3.34}$$

The static transfer function of the ring can now be found by assuming that $s_i(t) = s_i e^{j\omega t}$, and solving for the steady state solution to Eq. 3.28. The energy in the ring is found to be

$$\frac{e}{s_i} = \frac{-j\mu_i}{j\left(\omega - \omega_0\right) + \frac{1}{\tau}} \tag{3.35}$$

while the thru and drop transfer functions are

$$\frac{s_t}{s_i} = \frac{j\left(\omega - \omega_0\right) + \frac{1}{\tau} - \mu_i^2}{j\left(\omega - \omega_0\right) + \frac{1}{\tau}} \tag{3.36}$$

and

$$\frac{s_d}{s_i} = \frac{-\mu_i \mu_d}{j\left(\omega - \omega_0\right) + \frac{1}{\tau}} \tag{3.37}$$

respectively.

Calculating the power at the drop waveguide,

$$\left|\frac{s_d}{s_i}\right|^2 = \frac{\frac{4}{\tau_i \tau_d}}{\left(\omega - \omega_0\right)^2 + \frac{1}{\tau^2}} \tag{3.38}$$

the classic Lorentzian ring resonance shape can be observed. The FWHM can be quickly determined to be

$$\mathrm{FWHM}_\omega = \frac{2}{\tau} = 2\left(r_0 + r_i + r_d\right) \tag{3.39}$$

where $r_x = \frac{1}{\tau_x}$. Note that the amplitude decay rates for the intrinsic loss, input port, and drop port all contribute directly to the FWHM.

Using $\omega = 2\pi\frac{c}{\lambda}$ and assuming small ω/λ deviation,

$$\omega_0 + \Delta\omega = 2\pi\frac{c}{\lambda_0 - \Delta\lambda} \approx 2\pi\frac{c}{\lambda_0}\left(1 + \frac{\Delta\lambda}{\lambda_0}\right) = \omega_0\left(1 + \frac{\Delta\lambda}{\lambda_0}\right) \rightarrow \frac{\Delta\omega}{\omega_0} = \frac{\Delta\lambda}{\lambda_0} \tag{3.40}$$

Combining Eqs. 3.39, 3.40 yields

$$\begin{aligned}\mathrm{FWHM}_\lambda &= \frac{2}{\tau}\frac{\lambda_0^2}{2\pi c} \\ &= \frac{\lambda_0^2}{2\pi c}\left(1 - a^2 + |k_i|^2 + |k_d|^2\right)\frac{c}{n_g L} \\ &= \frac{1}{2}\frac{\lambda_0^2}{\pi n_g L}\left(1 - a^2 + |k_i|^2 + |k_d|^2\right)\end{aligned} \tag{3.41}$$

Figure 3.6 shows sample transmission responses for the ‘loop analysis’ and CMT analysis. Note that while the loop analysis captures the repeating spectral pattern (i.e. the FSR), the CMT model misses this feature. However, close to resonance (Fig. 3.6, center and right) the CMT and loop models are in close agreement.

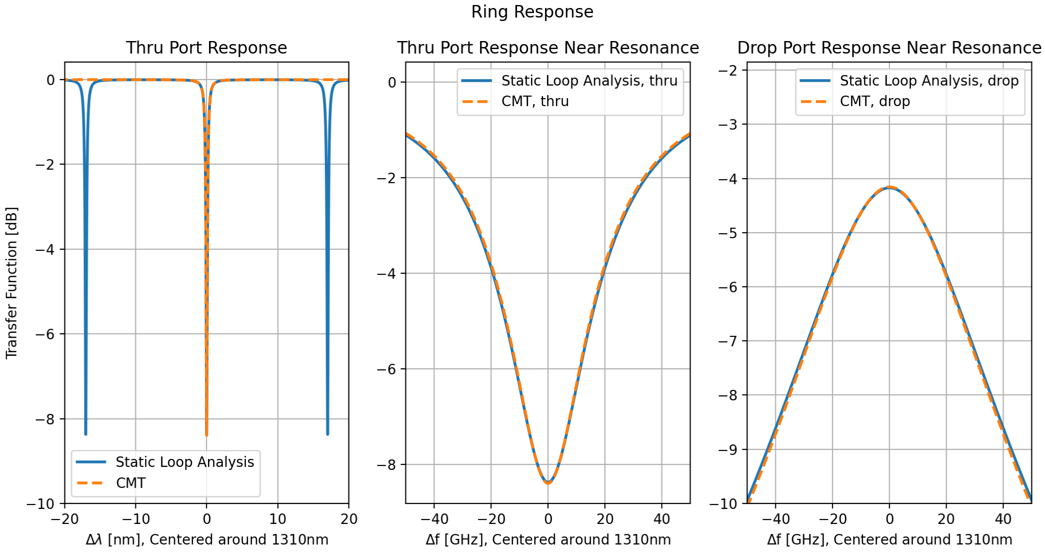

Figure 3.6: Ring resonator response for the static 'loop analysis' and CMT analysis. Plot of thru port response power ($10\log_{10}$ dB scale) across multiple FSRs (left) and near resonance (center). These correspond to Eq. 3.8 and the magnitude squared of Eq. 3.36. (right) Plot of drop port power response ($10\log_{10}$ dB scale) corresponding to Eqs. 3.9 and 3.38. The ring is designed with FSR $= 17\,\text{nm}$, $Q_0 = 10{,}000$, $\lambda_0 = 1310\,\text{nm}$, and a drop-port FWHM $= 60\,\text{GHz}$.

3.3 Optimized Drop Port Filters

The goal of the drop filter is to maximize the amount of power captured on resonance and delivered to the drop port. Consider the CMT response of a drop ring filter with intrinsic, input coupling, and output coupling amplitude decay rates of r_0, r_i and r_d, respectively. From Eq. 3.38, the peak drop port response on resonance is

$$P_{d0} = \frac{4 r_i r_d}{\left(r_0 + r_i + r_d\right)^2} \tag{3.42}$$

From Eq. 3.39, the FWHM bandwidth is $\omega_{3\text{dB}} = 2\left(r_0 + r_i + r_d\right)$. Thus, for a given target FWHM bandwidth, the peak drop power can be rewritten as

$$P_{d0} = \frac{16 r_i \left(\frac{\omega_{3\text{dB}}}{2} - r_0 - r_i\right)}{\omega_{3\text{dB}}^2} \tag{3.43}$$

The derivative is taken with respect to r_i, so that the input coupling can be optimized.

$$\frac{d}{dr_i} P_{d0} = \frac{16}{\omega_{3\text{dB}}^2} \left(\frac{\omega_{3\text{dB}}}{2} - r_0 - 2r_i\right) \tag{3.44}$$

Thus the optimal r_i is

$$r_i = \frac{\omega_{3\text{dB}}}{4} - \frac{r_0}{2} \tag{3.45}$$

Finally, from Eq. 3.39, the optimum drop port coupling is

$$r_d = \frac{\omega_{3\text{dB}}}{2} - r_0 - r_i = \frac{\omega_{3\text{dB}}}{4} - \frac{r_0}{2} \tag{3.46}$$

For symmetrically coupled drop rings, the on-resonance power at the drop port is given by

$$P_{d0,sym} = \frac{\left(\omega_{3\text{dB}} - 2r_0\right)^2}{\omega_{3\text{dB}}^2} \tag{3.47}$$

Note that maximum power is provided to the drop port when the input and drop waveguides are equally coupled. It is interesting that this optimum condition does not occur for a critically coupled ring, as one might expect since on resonance, critically coupled rings delivered no power to the thru port.

The on-resonance power for a critically coupled ring can be found by noting the critical coupling condition $r_i = r_0 + r_d$. Then for a given $\omega_{3\text{dB}}$,

$$\omega_{3\text{dB}} = 2\left(r_0 + r_i + r_d\right) = 4r_i \rightarrow r_i = \frac{\omega_{3\text{dB}}}{4}, \quad r_d = \frac{\omega_{3\text{dB}}}{4} - r_0 \tag{3.48}$$

For critically coupled drop rings, the on-resonance power at the drop port is thus given by

$$P_{d0,crit} = \frac{\omega_{3\text{dB}} - 4r_0}{\omega_{3\text{dB}}} \tag{3.49}$$

A comparison of the peak on-resonance power at the drop port for symmetric versus critical coupling is shown in Fig. 3.7. Note that as expected from the above optimization, the drop power on resonance when using symmetrically coupled rings is always greater than the drop power when using critically coupled rings. The improvement is larger as the ring bandwidth approaches the limit achievable for a given intrinsic quality factor. However, the improvement extends into the more ‘comfortably’ targetable ring design space (towards the top-right of the figure).

To highlight the need for sufficiently high intrinsic quality factors, Figure 3.8 shows the thru and drop port responses for both symmetric and critical coupling, for the same ring design target in two illustrative process nodes. Table 3.1 enumerates the CMT and static loop ring parameters for each of these designs. In the left figure, the target FWHM is 100 GHz, and the intrinsic Q_0 of this process is 6000 which represents a highly lossy and poor-quality photonic process. This represents an ‘aggressive’ design, which is close to the limit of what can be targeted in this technology. The symmetric response is clearly superior to the critically coupled response. However, because of the aggressive design target, the drop port still fails to capture a significant portion of the input light when on resonance. This is because, in order to achieve the FWHM design target, the drop port must be relatively

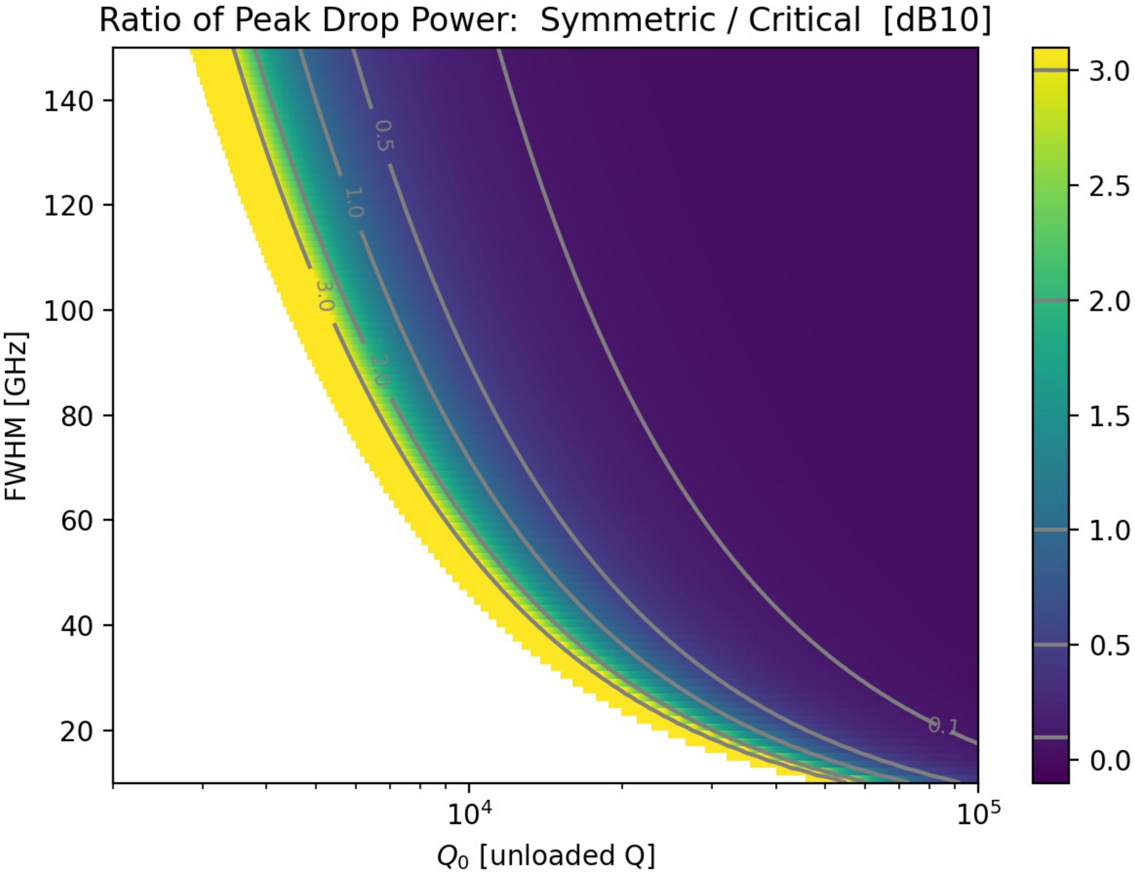

Figure 3.7: Ratio of the peak drop powers achieved for optimal symmetric versus critical coupling. Value is expressed in dB10 units. The ratio is plotted versus different intrinsic quality factors and target drop-port FWHM bandwidths. Note that symmetric coupling is always better than critical coupling. The white region indicates FWHM bandwidths that are not achievable with the quality factor. Contours are demarcated for particular ratios (3, 2, 1, 0.5, and 0.1 dB).

weakly coupled. In addition, significant energy is also lost to intrinsic loss in the ring, which can be observed in Table 3.1, as the $2r_0$ decay rate is larger than the drop port decay rate.

The second case in Fig. 3.8 targets the same FWHM bandwidth of 100 GHz but assumes a technology node which supports an intrinsic quality factor of $Q_0 = 70,000$. This intrinsic quality factor is more representative of what can be achieved in lightly doped drop ring filters in the GlobalFoundries Fotonix platform (discussed below). For this design target, the intrinsic loss decay rate is negligible compared to the input and drop port decay rates (Table 3.1), which results in nearly all power reaching the drop port when the ring is on

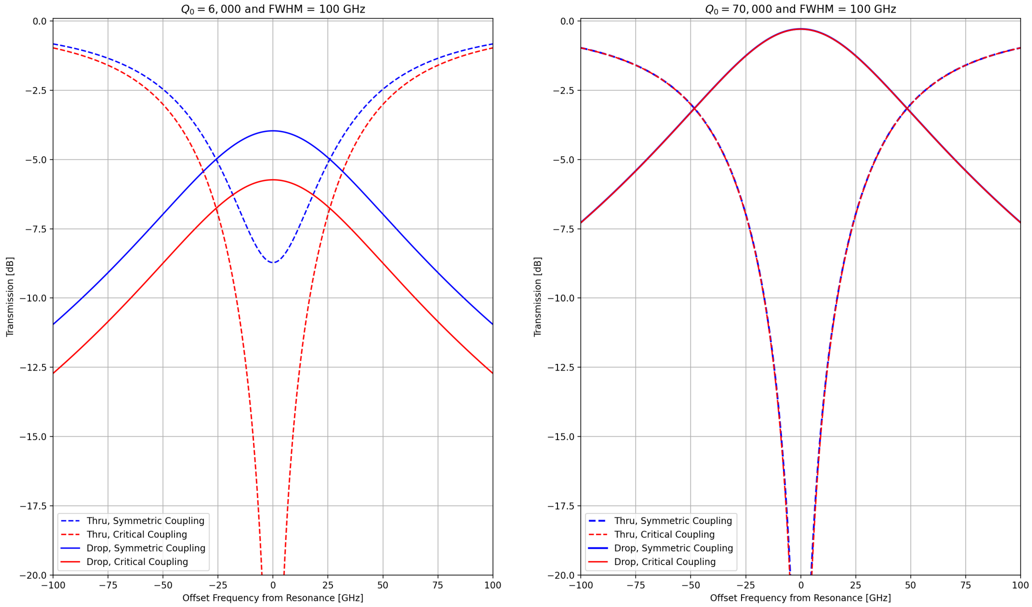

Figure 3.8: Thru and drop port responses for symmetric and critical coupling. The plot on the left shows a more 'aggressive' drop filter design, where the drop port coupling term is relatively weak to achieve the target FWHM. The plot on the right shows a case where the intrinsic loss is negligible; in this case, the symmetric and critically coupled designs are nearly identical.

resonance. In addition, the symmetric coupling and critical coupling responses are nearly identical. This result is consistent with Eqs. 3.45, 3.46, 3.48: as the intrinsic quality factor increases, r_0 decreases, and the symmetric and critically coupled decay rates become equal.

In addition to providing superior drop response, the symmetric drop filter design is superior to the critically coupled design in handling fabrication variation. Process and fabrication variation can result in chip to chip and wafer to wafer variation of waveguide and gap dimensions and material properties, which affect key parameters of photonic devices, such as effective and group index [48, 49]. As these variations exhibit spatial correlation [50], the ring filters designed with symmetric coupling are more likely to remain symmetrically coupled when variation occurs.

The key parameters (IL, FWHM, and channel isolation) can now be explored for the optimal symmetric drop filter design. Note that Q_0 impacts the range of target FWHM bandwidths that can be achieved. This makes intuitive sense– if the internal loss of the filter is too large (i.e. low Q_0 corresponding to large r_0 amplitude decay rates), narrow bandwidths

Table 3.1: Symmetric versus critically coupled drop ring designs for the three cases in Fig. 3.8. The upper half of the plot shows the CMT amplitude decay rate parameters, in units of GHz, and shows how each loss source contributes to the overall bandwidth of the filter. The lower half of the table presents the same information in the spatial 'loop analysis' view. Values specified show the self-coupling amplitudes of the input and output couplers, and the single-pass round trip loss factor.

			CMT Parameters		
FWHM [GHz]	Q_0		$2r_0$ [GHz]	$2r_i$ [GHz]	$2r_d$ [GHz]
100	6000	Symmetrically Coupled	36.6	31.7	31.7
		Critically Coupled	36.6	50.0	13.4
100	10000	Symmetrically Coupled	3.3	48.4	48.4
		Critically Coupled	3.3	50.0	46.8
			Static Loop Parameters		
FWHM [GHz]	Q_0		a	t_i	t_d
100	6000	Symmetrically Coupled	0.960	0.966	0.966
		Critically Coupled	0.960	0.946	0.986
100	10000	Symmetrically Coupled	0.996	0.947	0.947
		Critically Coupled	0.996	0.946	0.950

cannot be achieved.

The values of intrinsic (unloaded) quality factor (Q_0) which are achievable depend highly upon the technology platform being used and the design of the ring. The largest possible Q_0 occurs for rings with large radii, which avoid bending losses, and for undoped rings which avoid absorption losses [45, 51]. In the zero-change monolithic silicon photonics platform developed in GlobalFoundries 45nm SOI platform [36, 41], the intrinsic, undoped quality factor can be up to $Q_0 = 227000$ [52]. However, doping the resonator to be used as a modulator device results in a decreased loaded quality factor of roughly $Q_0 = 18000$ (for a 5 um ring). For a microring resonator used as a drop filter, lighter doping levels are required as compared to modulators. In the filter, the purpose of the doping is to perform carrier sweepout required to remove the electron-hole pairs generated during two-photon absorption and associated free carrier absorption [53]. The intrinsic quality factor for a drop filter will thus lie somewhere between. Other work reports lightly doped modulator microrings with $Q_0 = 39000$ [51], and simulated undoped intrinsic quality factor of $Q_0 = 88000$ [45]. The achievable range for Q_0 for lightly doped microring filters is thus likely below 100000 in current platforms.

The IL versus Q_0 and target FWHM bandwidth is plotted in Fig. 3.9, where for each design point, an optimal symmetric filter is used. Contours for several IL values are plotted. Note that as the design target approaches 'aggressive' design targets (left edge of the contour), the insertion loss increases. This is because for a given FWHM, as Q_0 decreases, r_0 increases, and thus the ring must be more weakly coupled to the access waveguides to

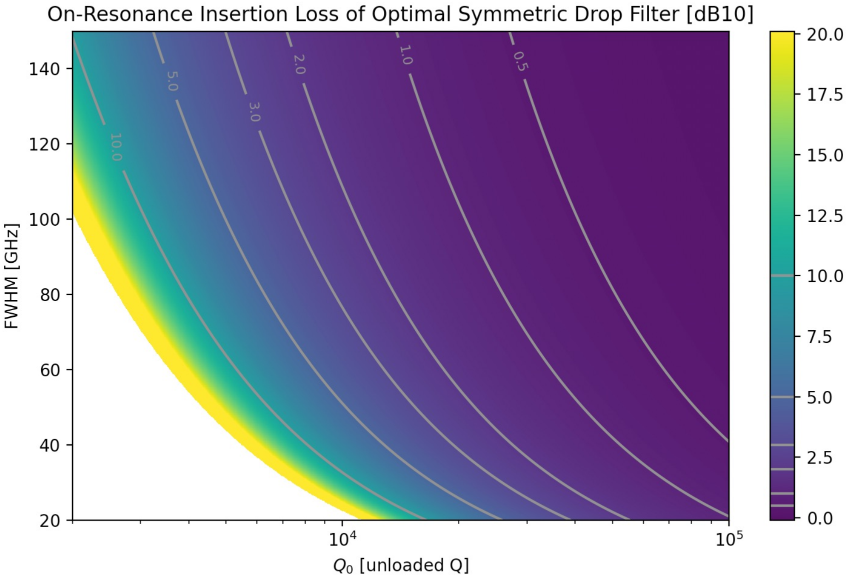

Figure 3.9: Insertion loss (IL) versus unloaded Q_0 and FWHM bandwidth. Contours are drawn for 0.5, 1.0, 2.0, 3.0, 5.0, and 10.0 dB of IL.

achieve the target FWHM. This implies less energy will couple to the drop port, and hence larger IL. Even at more 'conservative' design targets with larger Q_0 and FWHM, there can still be significant IL on resonance.

The final metric of interest is channel isolation. Channel isolation does not depend on Q_0– it only depends on the ratio of the channel separation to the target FWHM bandwidth. As the channel separation increases, the channel isolation will improve, at the roll-off rate of the filter. At the minimum channel spacing, in which there is no guardband between the spectrum occupied by adjacent optical channels, the channel isolation is 3 dB at band-edge, or ≈ 7 dB at band-center. At a more conservative channel spacing for which the band-edge to band-edge separation equals the ring filter bandwidth, isolation above 12 dB is achieved across the entire channel. An optimally designed link must balance the tradeoffs between inter channel crosstalk and filter IL to optimize the signal quality at the receiver.

3.4 Optical Channel Model

In order to evaluate the effect drop filter design on overall link performance, a optical channel model of the WDM link is created. The optical channel and drop filter response can be modeled as a linear time invariant (LTI) system, through which baseband data is transmitted. The optical channel is assumed to be dispersion free, limiting the results of this analysis to short-reach optical links. Such LTI channel models are often used in high-speed electrical wireline link analysis.

In such analyses, given an overall channel impulse response $h(t)$, the output of a single wavelength of modulated data can be written as

$$y(t) = \sum_k a_k h(t - kT) + n(t) \tag{3.50}$$

where a_k represent data symbols which are chosen with equal and independently distributed probability [54]. $n(t)$ represents additive Gaussian noise and T represents the period of the data pulses. If the signal is sampled at time points $t = \tau + mT$, where τ represents the sampling phase, then

$$y(\tau + mT) = \sum_k a_k h(\tau - (m - k)T) + n(\tau + mT) \tag{3.51}$$

Intersymbol interference (ISI) between the transmitted bit of interest and other transmitted bits in the same optical channel (same wavelength) clearly impacts the output amplitude. In addition, the output amplitude is sensitive to the timing phase at which the digital output data is sampled from the output waveform. In link implementations, a clock and data recovery circuit (CDR) is used to select the optimal sampling phase [55].

In this analysis, a worst-case channel model is assumed, in which all other bits are assumed to destructively interfere with the bit of interest. This is done to simplify the analysis and create a single value to represent the link performance. From Eq. 3.51, this means that the main cursor (i.e. the signal amplitude at time $t_m = \tau + mT$) will be attenuated by all the pre and post cursors

$$y_m(\tau) = h(\tau + mT) - \sum_{i \neq m} |h(\tau + iT)| \tag{3.52}$$

where the Gaussian noise has been neglected. To determine the optimal sampling point, the final post-ISI eye opening is computed for the entire bit period. Rather than selecting the peak eye opening value, which in higher order systems might be impacted by overshoot and undershoot to create narrow windows of artificially high eye opening with low timing margin, the following algorithm was used.

1. Determine peak eye opening
2. Determine start and end times at which the eye opening reaches 50% of the maximum
3. Select optimal sampling time as the time half-way between these start and end times
4. Eye opening is computed at this ‘optimal’ time point.

The eye opening computed by this procedure closely matches the peak eye opening that is found at the end of the bit period for first order systems, while maximizing timing margin.

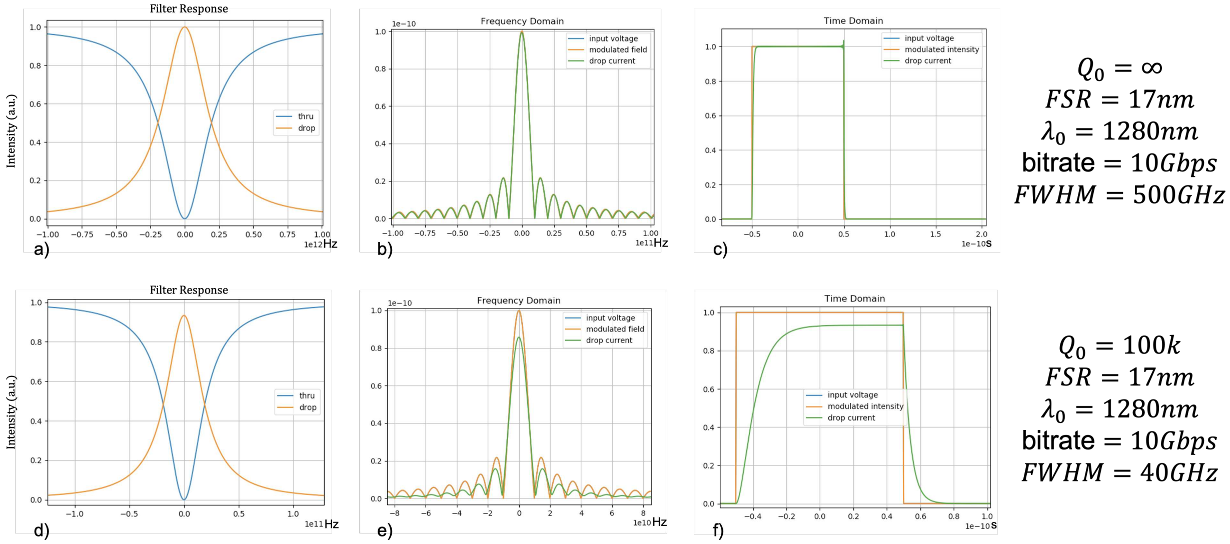

Figure 3.10: Channel model response for a single bit pulse at 10Gbps bitrate. a-c) Sample model response for idealized filter design, to validate coding for an 'perfect' channel response. a) Filter design with $Q_0 = \infty$, FSR = 17 nm, and FWHM = 500 GHz. b) Frequency domain of the modulated optical field and drop port current. c) Time-domain waveforms of the input voltage and output current, showing nearly identical behavior. d-f) Same plots for a more realistic filter design with $Q_0 = 100000$ and FWHM = 40 GHz.

In the model, an idealized Mach-Zehnder modulator modulates a single bit pulse into the optical domain, representing a single bit in a non-return to zero (NRZ) signaling scheme. The modulator is assumed to have an infinite bandwidth and 100% extinction ratio. The filter response is applied in the frequency domain, and the output current is translated back into the time domain. In this model, the photodetector is assumed to have responsivity of $R = 1\,\text{A/W}$, and both the photodetector and receiver circuits are assumed to have infinite bandwidth. This is done to isolate the design of the drop filter from other design variables. The impulse response $h(t)$ is thus determined, from which the eye opening and eye closure penalty can be calculated. Because the optical channel is assumed to be lossless (other than the drop ring filter), the modulator is ideal, and the responsivity has amplitude 1, the ideal response due to a pulse of amplitude 1 should be a pulse at the output also of amplitude 1.

The responses of the channel model for two example ring designs are shown in Fig. 3.10. For this motivating example, a bit pulse at a datarate of 10Gbps (pulse width of 100 ps) is used. The top row (Fig. 3.10a-c) shows the model response for an idealized filter design. For this filter, $Q_0 = \infty$ which represents a lossless photonic platform, and the filter bandwidth is approximated to be infinitely wide by setting FWHM = 500 GHz. As can be seen in Fig. 3.10c, the output drop current response (green) closely matches the input pulse. This is expected, as a lossless drop filter with infinite bandwidth should not lose any energy.

The bottom row (Fig. 3.10d-f), shows the response for a more realistic ring, designed with an intrinsic quality factor of $Q_0 = 100000$, and a bandwidth of FWHM = 40 GHz. The slow rise and fall times at the leading and trailing edges of the pulse are due to the finite bandwidth of the channel. In addition, note that the final '1' level does not settle to the same height as in the ideal case. This is due to the losses from the finite intrinsic quality factor.

The next component of the link model that must be accounted for is crosstalk. Crosstalk from adjacent channels will create an interfering photocurrent that distorts the desired eye opening. In the worst case assumption used in this model, the crosstalk is assumed to create a current that always opposes the desired bit. In contrast with Eq. 3.52, the worst case distortion from crosstalk can be found by summing all the cursors of the channel response

$$\text{xtalk}_m(\tau) = \sum |h_{xtalk}(\tau + iT)| \approx P_d(\text{channel spacing}) \cdot \sum |h(\tau + iT)| \tag{3.53}$$

where the effect of the crosstalk transferring into the channel of interest on a different part of the drop filter transfer function is approximated as a constant attenuation by the channel isolation between the drop filter of interest and the interfering channel. This allows for rapid calculation of the effect of crosstalk as the channel spacing varies.

In addition, it should be noted that the channel in question has itself passed through some number of drop filters tuned to other optical channels, and has thus itself been attenuated by the thru response insertion loss of the preceding filters. This means that the energy reaching the drop filter for each channel depends on the index of that channel in the overall WDM array. While this is technically true, it can be seen from the thru response for realistic drop filters (Fig. 3.8), that beyond the immediately adjacent channel, the thru port insertion loss is practically negligible. Furthermore, the model assumes that no additional loss mechanisms are present in the ring (for example, coupler loss), such that completely off resonance, the insertion loss to the thru port is 0 dB (i.e. no loss). Thus, to get a representative figure of merit that does not depend on the channel's index in the array, it is assumed that the energy belonging to the channel in question has already been attenuated by the thru port insertion loss of one and only one immediately adjacent drop filter.

In summary, the eye opening is calculated using the following 'representative' equation:

$$\begin{aligned}\text{eye opening} =& P_t(\text{channel spacing}) \cdot h_0 && \longleftarrow \text{main cursor} \\ &- P_t(\text{channel spacing}) \cdot \sum_{i \neq 0} |h_i| && \longleftarrow \text{ISI} \\ &- P_d(\text{channel spacing}) \cdot \sum |h_i| && \longleftarrow \text{crosstalk}\end{aligned} \tag{3.54}$$

P_t and P_d are the thru and drop port responses, and are functions of the ring design parameters (FWHM, FSR), as well as technology parameters (Q_0). The (channel spacing) is meant to indicate that the model frequency-shifts the ring response by the channel spacing, to account for the effects of adjacent channels (note that h_i already includes the effect of the ring belonging to the channel of interest). Note again that this model only captures the effects of

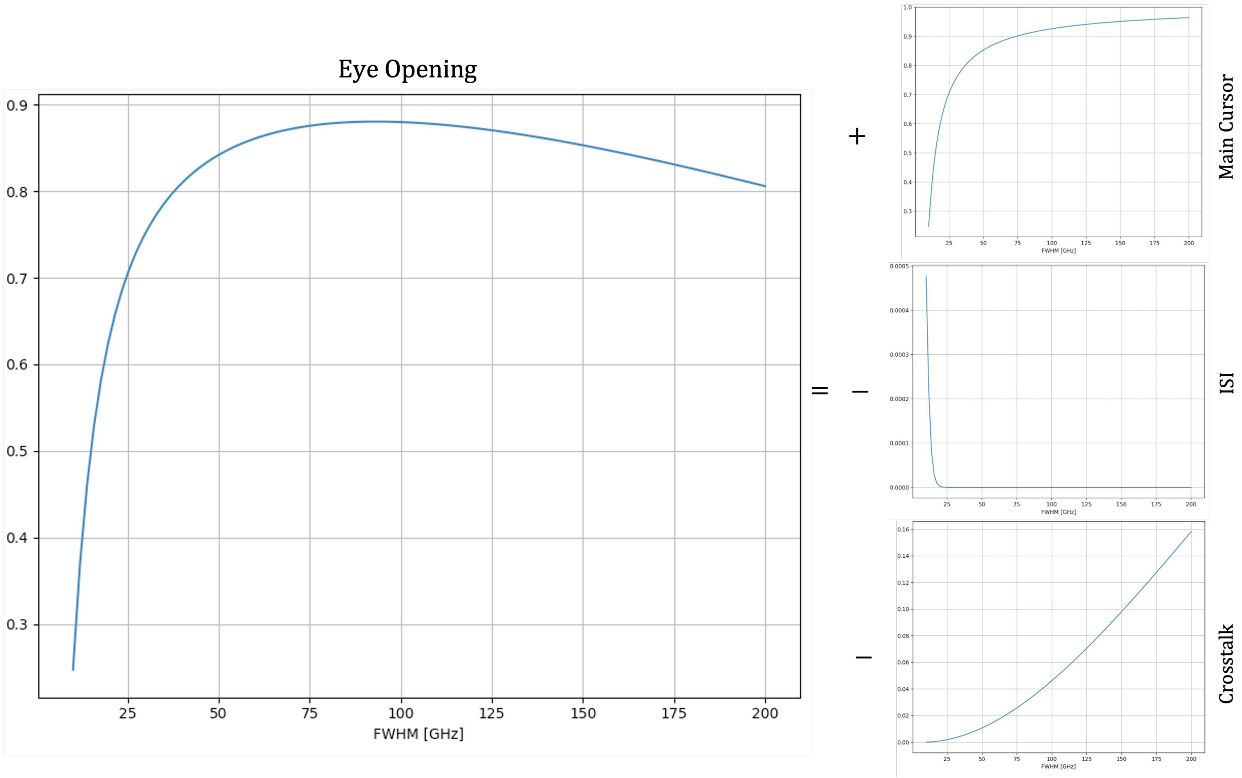

Figure 3.11: Eye opening versus FWHM design bandwidth for a single drop ring filter. The relevant ring parameters are: $Q_0 = 100000$, FSR $= 17\,\text{nm}$, and $\lambda_0 = 1280\,\text{nm}$. The bitrate is 10Gbps. The channel spacing is 500 GHz The subplots on the right show the contributions to eye opening from the main cursor, ISI, and crosstalk (from top to bottom). The optimum eye opening occurs for a ring bandwidth of FWHM $= 87\,\text{GHz}$.

the optical filters; in reality, finite bandwidth of the photodetector and receiver circuit may cause additional ISI, but may also attenuate some of the high frequency components of the crosstalk signal.

3.5 Single Ring Filter Optimization

The model described above is now used to evaluate the impact of ring filter design on link performance. Figure 3.11 shows the eye opening as a function of the drop ring FWHM bandwidth for a representative optical channel. The optical parameters for the ring are $Q_0 = 100000$, FSR $= 17\,\text{nm}$, and $\lambda_0 = 1280\,\text{nm}$, and the bitrate is 10Gbps. As mentioned above, the eye opening represents the signal amplitude in the electrical domain after the photodetector in the link, and is normalized such that 1 represents an ideal lossless eye (as

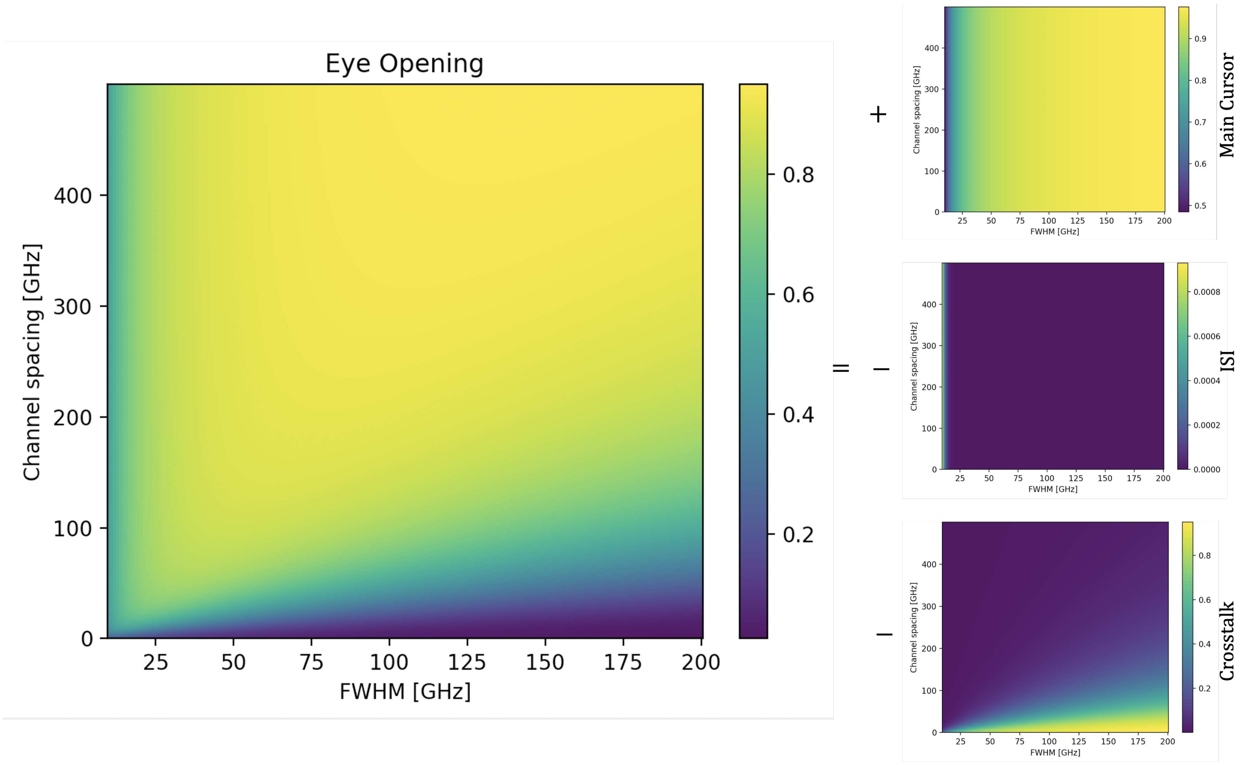

Figure 3.12: Eye opening versus FWHM design bandwidth and channel spacing for a single drop ring filter. The relevant ring parameters are: $Q_0 = 100000$, FSR $= 17\,\text{nm}$, and $\lambda_0 = 1280\,\text{nm}$. The bitrate is 10Gbps. The subplots on the right show the contributions to eye opening from the main cursor, ISI, and crosstalk (from top to bottom).

the optical system is passive, there is no gain, so the eye opening cannot be larger than 1).

The channel spacing assumed for this figure is 500 GHz, which implies that 6 channels can fit in the 17 nm $\approx$ 3.2 THz FSR.

Note that the eye opening has a peak at roughly FWHM = 87 GHz. This optimum can be explained by investigating the contributions of the main cursor, ISI, and crosstalk amplitudes (Fig. 3.11, right, top to bottom). The signal amplitude captured in the main cursor (h_0) increases as the FWHM increases, as less energy is lost from the drop filter response. However, as the ring bandwidth increases, the crosstalk increases as well, and begins to dominate any improvement from the main cursor. Note that ISI also decreases with increasing filter bandwidth; however, its contribution is small even at low filter bandwidths.

The above channel spacing of 500 GHz is rather generous. According to the CW WDM MSA [56], a new standard for O-band laser sources targeting optical interconnect applications, WDM links with 8, 16, and even 32 channels are being targeted. With FSR spans of 9 nm, 18 nm, and 36 nm, these correspond to channel spacings of 100 GHz, 200 GHz, and

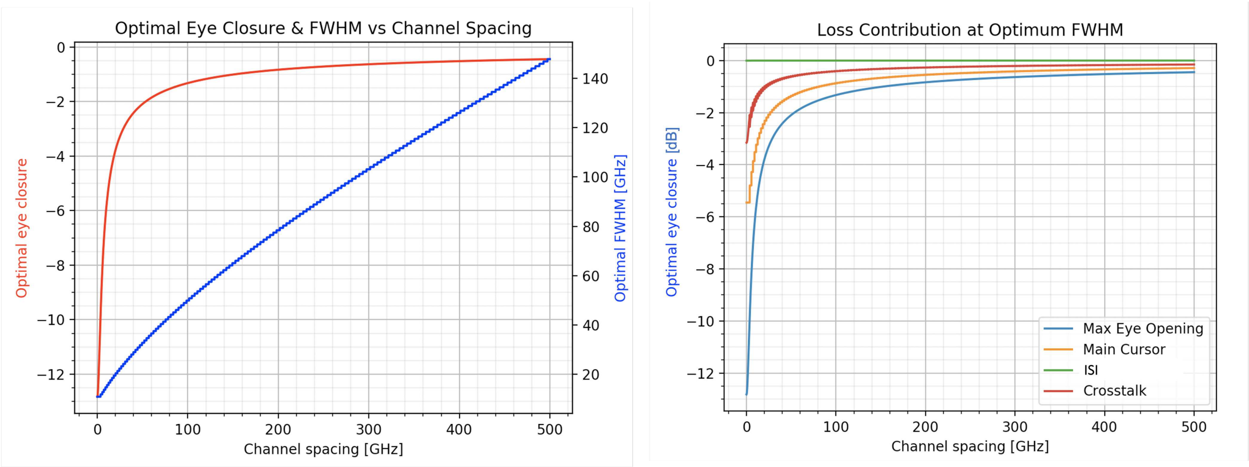

a)

b)

Figure 3.13: a) Optimum FWHM and minimum eye closure achievable versus channel spacing. b) Eye closure total and contributions from in-band attenuation (‘main cursor’), ISI, and crosstalk. Each curve represents the contribution to total eye closure (in dB) from each loss source. The relevant ring parameters are: $Q_0 = 100000$, $\mathrm{FSR} = 17\,\mathrm{nm}$, and $\lambda_0 = 1280\,\mathrm{nm}$. The bitrate is 10Gbps.

400 GHz, with a channel spacing of 800 GHz only specified for the 32-channel 36 nm span.

It is therefore interesting to investigate the impact of crosstalk, ISI, and in-band channel attenuation against both channel spacing and FWHM bandwidth. Figure 3.12 shows the eye opening (and main cursor, ISI, and crosstalk breakdowns) for the same ring parameters used in Fig. 3.11. Observing vertical cuts of Fig. 3.12 shows that for a given FWHM bandwidth, eye opening increases monotonically as channel spacing increases, as is intuitively expected. Observing horizontal cuts of Fig. 3.12 show that for a given channel spacing, there is an optimal FWHM bandwidth that maximizes the eye opening by optimally trading off degradation from ISI, crosstalk, and in-band attenuation.

For each channel spacing in the optical system described above, the optimal FWHM which provides the largest eye opening is plotted in Fig. 3.13a. Also plotted is the eye closure, which is measured as eye closure $= 20\log_{10}(\text{eye opening})$. For the 10Gbps datarate used in this simulation, the eye closure penalty at a channel spacing of 100 GHz is 1.3dB, and is achieved at a FWHM bandwidth of approximately 50 GHz. The contributions to eye closure from in-band attenuation (channel loss), ISI, and crosstalk are plotted in Fig. 3.13b. At each channel spacing, the optimal FWHM design is chosen. The primary source of eye closure penalty for all channel spacing is from the attenuation to the main cursor due to in-band loss in the channel. The secondary source of loss is from crosstalk. Finally, it can be seen that the optical channel imposes negligible ISI eye closure penalty. (Note- this conclusion does not implying that optical links do not suffer from ISI in general; rather, the

Table 3.2: Eye closure [dB] for various datarates. Optical parameters are FSR = 17 nm, $\lambda_0 = 1280\,\text{nm}$, and $Q_0 = 30000$.

	Channel Spacing [GHz]		
Datarate [Gbps]	100	200	400
10	-2.8	-1.8	-1.1
25	-2.9	-1.8	-1.1
56	-3.0	-1.9	-1.2

results indicate that bandwidth limitations from properly designed drop filters should not create ISI that impacts the signal.)

The impact of limited intrinsic quality factor is investigated. Figure 3.14 shows the optimal eye closure (minimum loss) and the optimal FWHM bandwidth which maximize eye opening for three different NRZ data rates: 10, 25, and 56 Gbps. For each datarate, the eye closure is plotted for multiple intrinsic quality factors as channel spacing is increased. First, note that as Q_0 decreases, the eye closure gets worse. This makes sense, as a lower Q_0 corresponds to greater energy lost in the ring filter. In addition, note that as Q_0 decreases, the FWHM which optimizes the eye opening increases; this makes sense as a lower Q_0 causes a larger lower-bound to the achievable FWHM bandwidth. Note that as Q_0 improves (increases), there is a diminishing return in the improvement to eye closure.

It is interesting to compare the eye closure penalties for different target data rates at the various CW WDM MSA channel spacings. Table 3.2 shows the eye closure penalty for the three datarates (10, 25, and 56 Gbps) at the three channel spacing frequencies of 100, 200, and 400 GHz. Note that at larger channel spacing (400 GHz), there is very little difference between the eye closures at the three data rates. Even at the smallest channel spacing of 100 GHz, which is less than 2x the fastest channel datarate and yet 10x the slowest channel datarate, the difference between eye closure is still small. These results indicate that the dense 100 GHz channel spacing in the CW WDM MSA standard [56] is suitable for NRZ datarates beyond even 56 Gbps.

Finally, fabrication variation is often a concern for the performance of silicon photonic devices [57–59]. Variation in layer thickness, ring dimensions, and waveguide width can affect the quality factor of microring resonators [57], which will impact the eye closure of the overall link. The effect of Q can be seen by noting the change in eye closure for a given channel spacing in Fig. 3.14. Precise impacts on link performance require knowledge of the variation in physical parameters and Q factor for a particular fabrication process, as well as knowledge of the datarate and channel separation being targeted for the system. As an illustrative example, results from one 150mm SOI wafer process [60] suggest maximum Q variation from 10000 to 30000 for a nominal ring design. Applying this spread to the 56 Gbps target datarate, the spread in eye closure penalties is presented in Table 3.3. It can be seen that at more aggressive channel spacings, the impact of Q_0 variation on eye closure is more significant.

Process variation can also impact the realized bandwidth of a ring filter nominally de-

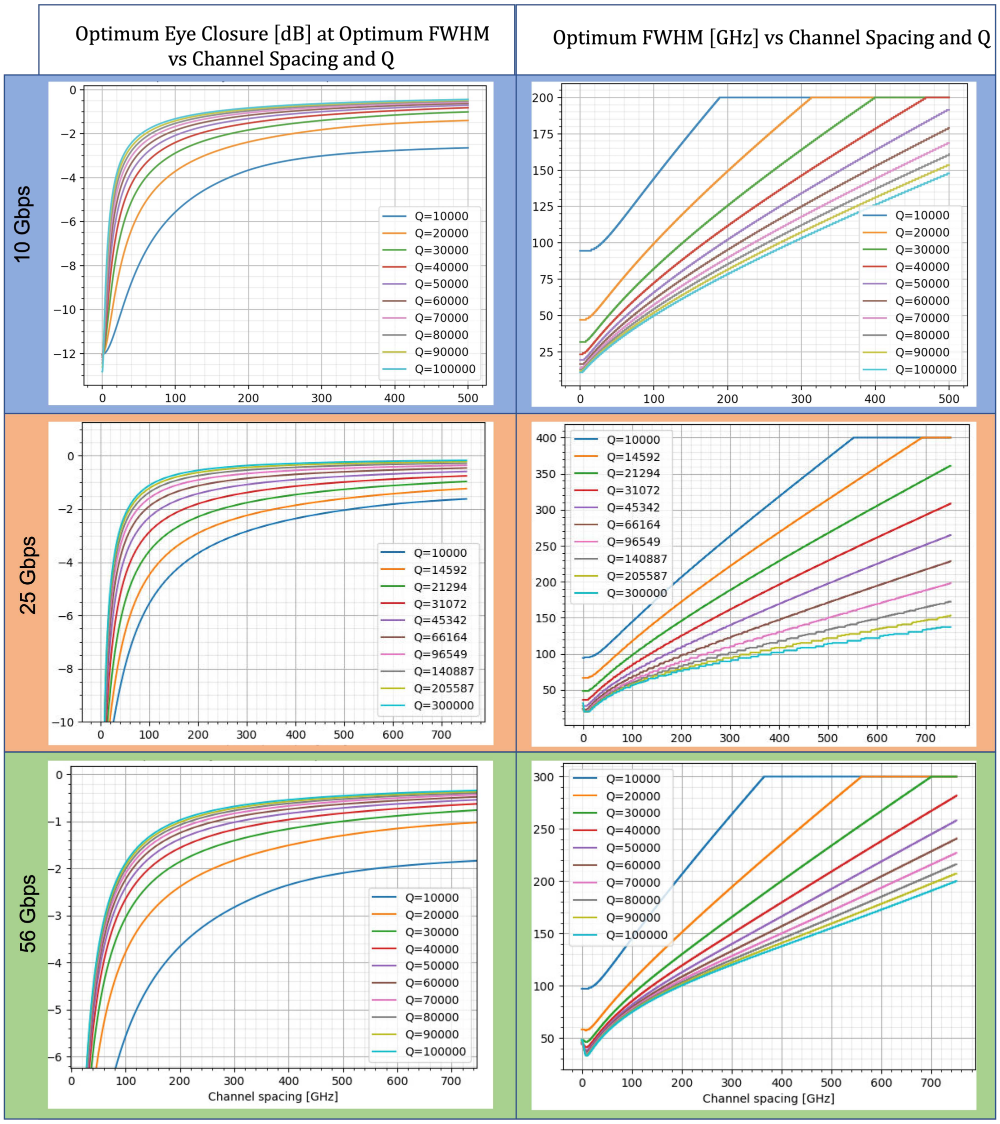

Figure 3.14: Optimized eye closure (left column) and optimal FWHM bandwidth (right column) at which the eye opening is maximized. From top to bottom, the datarate is 10, 25, and 56 Gbps. At each datarate, the ring design is optimized across channel spacing for multiple Q_0 values. The FSR of the rings are designed to be 17 nm at a center wavelength of 1280 nm. Note: at high channel spacing and low Q_0 values, the FWHM appears to saturate. This is an artifact of the limited sweep range used in the study. This also leads to the eye closure at these saturated channel space and Q_0 points not representing the most optimal eye achievable.

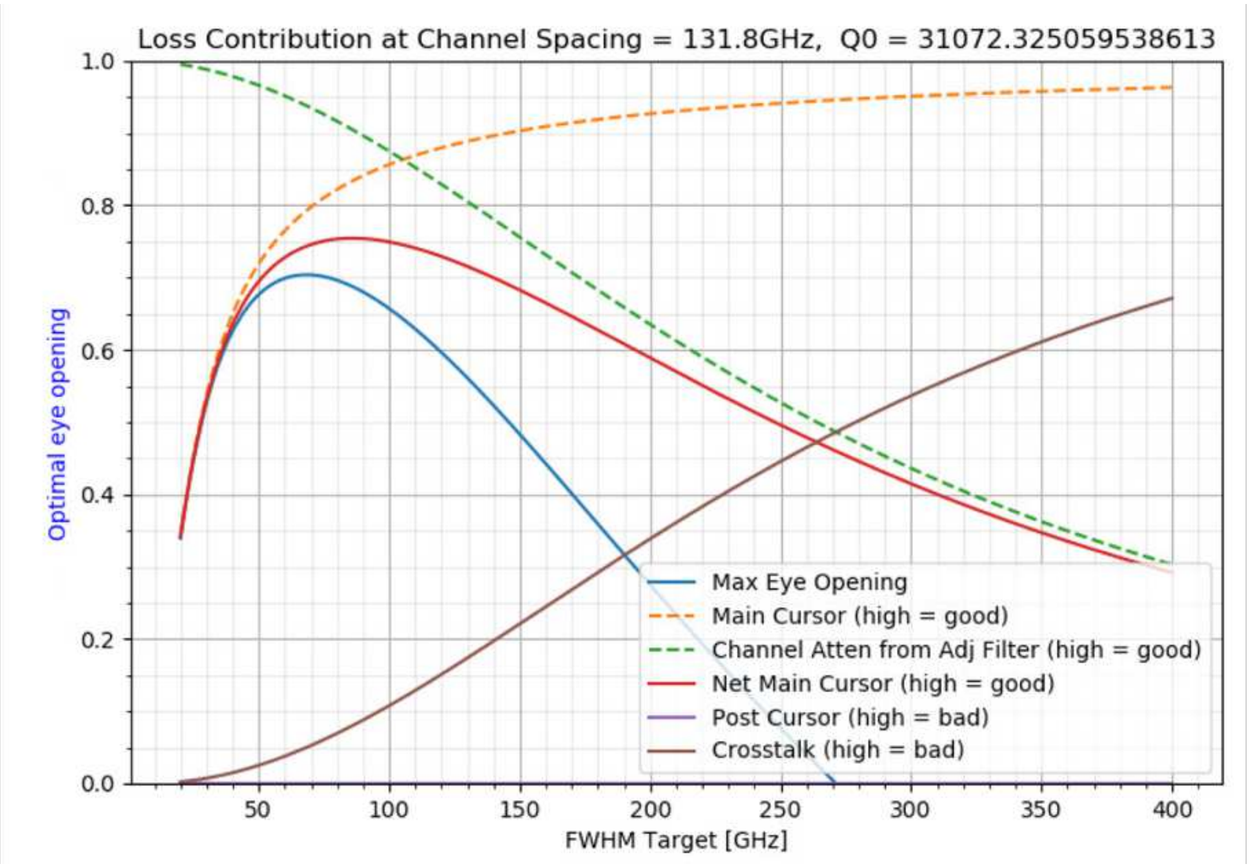

Figure 3.15: 25Gbps NRZ loss contribution (as impact on eye-opening) from in-band and adjacent filter attenuation, crosstalk, and ISI versus FWHM design bandwidth. Individual loss contributions multiply together to result in the overall eye opening, shown in blue.

signed for a target FWHM. To investigate how eye closure is impacted by this variation, Figure 3.15 plots the loss contribution from the various sources (ISI, channel attenuation, and crosstalk) versus FWHM target for a particular channel spacing and intrinsic quality factor. The optimum FWHM, which provides the peak eye opening, shows a relatively broad maximum. A change in waveguide width of 10nm, which falls within the variation range in

Table 3.3: Eye closure [dB] range for Q_0 variation $(10000 - 30000)$ at 56 Gbps and CW WDM MSA channel spacings. Optical parameters are FSR $= 17\,\text{nm}$ and $\lambda_0 = 1280\,\text{nm}$.

	Channel Spacing [GHz]		
	100	200	400
Eye Closure [dB]	-5.6 to -3.0	-3.7 to -1.9	-2.4 to -1.2

[60], affects a FWHM change of less than 10 GHz, which keeps the eye opening to within 1% of the peak. This optimal design point thus shows good stability against process variation.

In addition, Figure 3.15 can be used to investigate the eye closure breakdown between the various loss sources. For this particular link example, the majority of eye closure penalty is due to intrinsic ring losses (65% of total eye closure). The next most significant loss contribution (20%) comes from adjacent channel filtering, in that the prior drop filter in the WDM link attenuates the channel of interest. Finally, crosstalk contributes to roughly 15% of the overall eye closure. This breakdown highlights the sensitivity of performance to technology parameters.

While precise quantitative impacts of fabrication variation need to be determined using statistical information for a given process, the link model developed here can serve as a useful framework to translate statistical variation data on physical parameters (such as etch width and SOI thickness) into higher level link margin predictions.

3.6 Multi-Ring Filters

As observed in Section 3.4, the optimization of microring drop filter performance requires selecting a FWHM bandwidth that balances eye closure due to attenuation within the signal band and eye closure from crosstalk. A FWHM that is too large results in low in-band attenuation but causes crosstalk to dominate the eye response, and vice-versa for a small FWHM. High order microring filters, in which multiple microrings are coupled together to produce a higher order filter response, have been proposed to achieve larger channel isolation (through sharper out-of-band rejection) and a flatter in-band frequency response [61–64].

A summary of high order microring filter results is presented in [65]. Many of these results are from devices fabricated in custom photonics platforms which are tailored to provide low loss. In Table 3.4, several of these results are reported, along with the estimated intrinsic quality factor available in the platforms used (from directly reported data or extracted from waveguide loss data reported in the publications). Even using platforms that support relatively high Q_0, the total loss of these multi-ring filters often exceeds 1 dB.

Table 3.4: Reported filter order and insertion loss per element, and estimated intrinsic quality factor for various high order ring filters.

Work	Filter Order	Insertion Loss [dB/element]	Intrinsic Q (Q_0)
[66]	4	0.37	130000
[63]	5	0.36	180000*
[65]	5	0.28	260000*

* Upper bound, estimated from reported linear loss only.

In order to evaluate more directly the impact of higher-order microring drop filters, the above channel model is extended to utilize the drop response of second order ring filters.

The drop and thru responses are derived using the Mason gain formula [67]

$$\frac{E_d}{E_i} = \frac{-jk_1k_{12}k_2\sqrt{a_1a_2}e^{\frac{j}{2}(\theta_1+\theta_2)}}{1-(t_1t_{12}a_1e^{j\theta_1}+t_{12}t_2a_2e^{j\theta_2}-t_1t_2(1-t_{12}^2)e^{j\theta_1}e^{j\theta_2})+t_1t_{12}^2t_2a_1a_2e^{j\theta_1}e^{j\theta_2}} \tag{3.55}$$

$$\begin{aligned}\frac{E_t}{E_i} =& \frac{1}{1-(t_1t_{12}a_1e^{j\theta_1}+t_{12}t_2a_2e^{j\theta_2}-t_1t_2(1-t_{12}^2)e^{j\theta_1}e^{j\theta_2})+t_1t_{12}^2t_2a_1a_2e^{j\theta_1}e^{j\theta_2}}\cdot \\ & (t_1\big(1-\big(t_1t_{12}a_1e^{j\theta_1}+t_{12}t_2a_2e^{j\theta_2}-t_1t_2(1-t_{12}^2)e^{j\theta_1}e^{j\theta_2}\big)+t_1t_{12}^2t_2a_1a_2e^{j\theta_1}e^{j\theta_2}\big) \\ & -k_1^2t_{12}a_1e^{j\theta_1}\big(1-\big(t_{12}t_2a_2e^{j\theta_2}\big)\big) \\ & +k_1^2k_{12}^2t_2a_1a_2e^{j\theta_1}e^{j\theta_2})\end{aligned} \tag{3.56}$$

Unlike in [40], the intrinsic losses have not been neglected, as they play a role in the overall performance.

A comparison of sample single and double ring responses is shown in Fig. 3.16 For each value of Q_0, both ring types were designed with the same FWHM bandwidth of 60 GHz. The double ring filters were designed to have a maximally-flat Butterworth response. The ring coupling parameters to achieve this bandwidth were determined by numerically solving for the pole placement, based on the analytic ring response which includes intrinsic loss, Eqs 3.55 and 3.56. Note that the double ring filter response offers a flatter response within the filter band, as well as sharper out of band rejection. However, this comes at the cost of increased peak insertion loss. Note also that the discrepancy between peak insertion loss for the single and double rings becomes larger as the Q_0 decreases.

Similar to the case for single-ring drop filters, the channel model was evaluated for various intrinsic quality factors. For each channel separation, the optimal filter bandwidth was determined which optimizes eye opening against the impairments of in-band channel attenuation, ISI, and crosstalk. Figure 3.17 shows the difference between the optimal double-ring and single-ring channel responses at three different datarates and for multiple intrinsic quality factors and channel spacings. The figure presents the difference (in dB) between the eye closure penalty for double-ring and single-ring filters. Positive values on the plot indicates that double-rings have less eye closure penalty (i.e. positive values indicate where double-ring filters outperform single-ring filters). The model was evaluated for datarates of 10Gbps, 25Gbps, and 56Gbps.

There are several trends worth noting in Fig. 3.17. First, note that at all datarates, as the intrinsic quality factor is increased, double ring filters begin to outperform single ring filters. This is because the insertion loss due to the larger number of rings is not as significant, and thus, the benefits of flatter in-band response and out-of-band isolation become apparent. Note that at low Q_0 single ring filters outperform double ring filters. Second, note that at higher datarates, double ring filters tend to outperform single ring filters in general. This can be explained in that higher signal bandwidth are more affected by the non-ideal in-band channel attenuation from single ring filters. The flatter in-band response of double-ring filters is more impactful for higher bandwidth signals. Next, it can be seen that as channel spacing

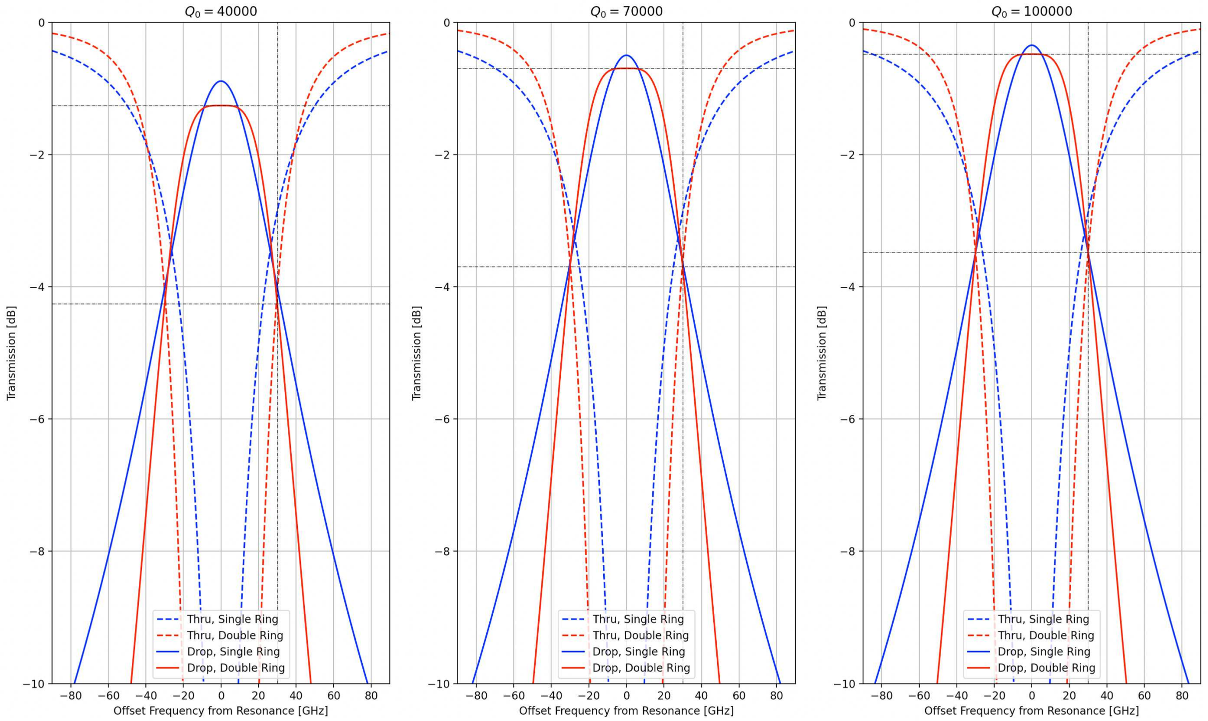

Figure 3.16: Thru and drop port transmission responses for single (blue) and double (red) ring filters. The Q_0 is 40000 (left), 70000 (center), and 100000 (right). Faint black dashed lines mark the FWHM bandwidth, IL, and 3-dB loss values. The optical parameters are FSR = 17 nm, λ_0 = 1280 nm, and a target FWHM bandwidth of 60 GHz.

increases, the difference in eye closure penalty across intrinsic quality factors decreases. This is because at large channel spacing, crosstalk has a reduced impact, so the optimal drop filters can afford to target high FWHM bandwidths which have reduced in-band attenuation.

A limited sweep range for FWHM bandwidths causes slight inaccuracies in the calculated eye closure for high channel spacing and low intrinsic quality factors. This causes the contours to cross at high channel spacings in the 10Gbps and 25Gbps plots, Fig. 3.17. The contours as Q_0 changes should not cross: higher Q_0 always results in reduced eye closure, and better performance for dual-ring filters over single-ring filters. The behavior at very low channel spacing is because the crosstalk falls within the BW of the filter, which leads to poor performance and optimization, and does not reflect realistic operating conditions.

While dual ring filters might outperform single ring drop filters, it is important to fully consider the benefits and drawbacks to a multi-ring filter. For example, at 56Gbps and with a practical $Q_0 \approx 70000$, double ring filters afford a 2.9dB, 1.9dB, and 1.2dB improvement over single rings at the CW-WDM-MSA channel separation frequencies of 100GHz, 200GHz, and 400GHz [56]. This improvement in eye-opening comes at the cost of complex tuning

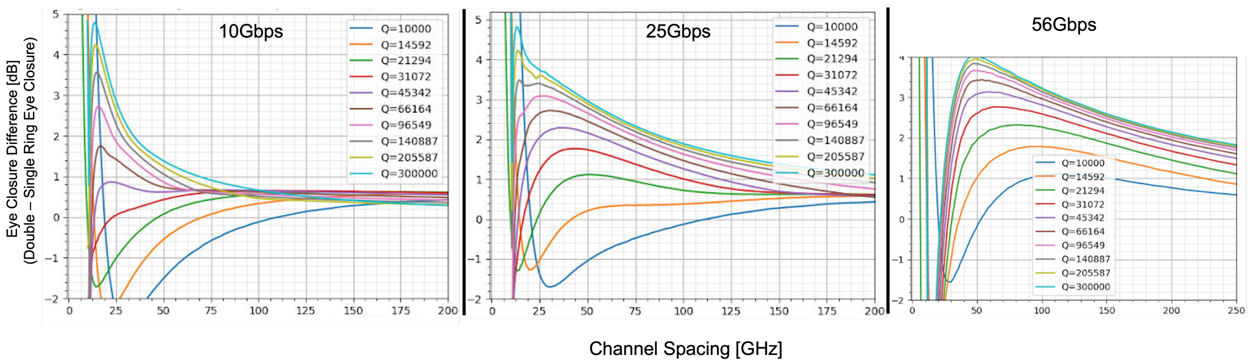

Figure 3.17: Comparison of double ring drop filters versus single ring drop filters. The plots show the difference in eye closure when using double-ring filter or single-ring filters at the same datarate, channel separation, and intrinsic quality factor. Positive values indicate the double ring shows smaller eye closure penalty (i.e. positive values indicate where double-rings outperform single ring filters). Note that at very large channel spacing and low Q_0, the limited sweep range of the FWHM during optimization causes inaccurate eye closure values. The optical parameters are $\mathrm{FSR} = 17\,\mathrm{nm}$ and $\lambda_0 = 1280\,\mathrm{nm}$.

and increased thermal power. Process and fabrication variation cause the radii and coupling strengths of each ring in multi-ring filters to be offset from their ideal values. To obtain the optimal filter performance, thermal tuning is most frequently used to adjust the resonance wavelength of each ring. Additional complexity is added to tune multi-ring filters, which require more complicated calibration routines and control algorithms [68]. Thermal tuning efficiency depends highly on the platform [69], but is roughly $1.5\frac{mW}{nm}$ in GlobalFoundries' 45nm monolithically integrated CMOS platform [6]. This heater power is per-ring, as FEM simulations indicate that roughly only 20% of heat can be 'shared' between adjacent rings in the filter. In terms of optimizing holistic link performance under a constrained energy budget, this link model can be used to provide guidance whether higher order rings are truly beneficial, or whether spending power on other parts of the link could have more significant impact.

3.7 Conclusion

Understanding the limitations of channel densification is crucial to maximizing the performance of WDM links. To this end, this chapter provided an overview of WDM links and derived the equations governing the behavior of microring drop filters. It was found that symmetric add-drop coupling provides superior performance over critically-coupled ring filters at the same intrinsic quality factor and FWHM bandwidth, though this improvement diminishes as Q_0 increases. Furthermore, the impact of limited intrinsic quality factor was specifically noted as the primary source of insertion loss in drop ring filters.

The chapter next introduced a channel modeling framework to evaluate the impact of crosstalk and insertion loss on eye closure in WDM links. It was found that an optimum design point for FWHM bandwidth exists for a given channel spacing and Q_0. While the loss contributions depend on exact link specifications, it was found that for a representative channel spacing and quality factor, loss from limited quality factor contributed most significantly to eye closure, followed by filtering from the adjacent channel, and lastly from crosstalk. Finally, the channel model was extended to investigate the performance improvement that dual-ring drop filters can offer over single-ring filters. It was found the performance of double ring filters can surpass that of single ring filters in technology processes where the intrinsic quality factor is high enough, and for high enough datarates. However, and more realistic intrinsic quality factors and channel spacing, dual-ring filters offer only moderate performance gains.

Chapter 4

Analog Modulation of Microring Resonators

In this chapter, the performance of optical links under analog modulation is investigated. In Section 4.1, a model of the optical link is presented which treats the laser-modulator-receiver system as a single Gm stage. The transconductance and intrinsic gain of the link are derived. Section 4.2 presents an overview of the noise sources in optical links, and derives the link noise figure. Section 4.3 demonstrates a case study in which analog optical links are shown to provide power-saving benefits over conventional digital style links in massive MIMO basestations or radar arrays. The linearity of microring modulators for analog optical links is explored in Section 4.5, and experimental measurements verifying the predicted linearity performance are presented.

4.1 Optical Links as a Gm Stage

Let us begin the study of analog modulation by considering the system shown in Fig. 4.1. Unmodulated light from a laser is input to an external amplitude modulator, which driven by some sinusoidal voltage waveform. After propagating some distance along an optical fiber, the modulated optical signal impinges on a photodetector, which converts the signal back into the electrical domain. Such a link is called an intensity modulation direct detection (IMDD) link.

At the output of the laser, before the modulator, the electric field is

$$E_L = E_0 e^{j\omega_0 t} \tag{4.1}$$

where $E_0 = \sqrt{P_0}$ is the square root of the laser output power.

The modulator has a transfer function which describes the relationship between the output electric field and the input voltage applied to the modulator, Fig. 4.2. The DC term

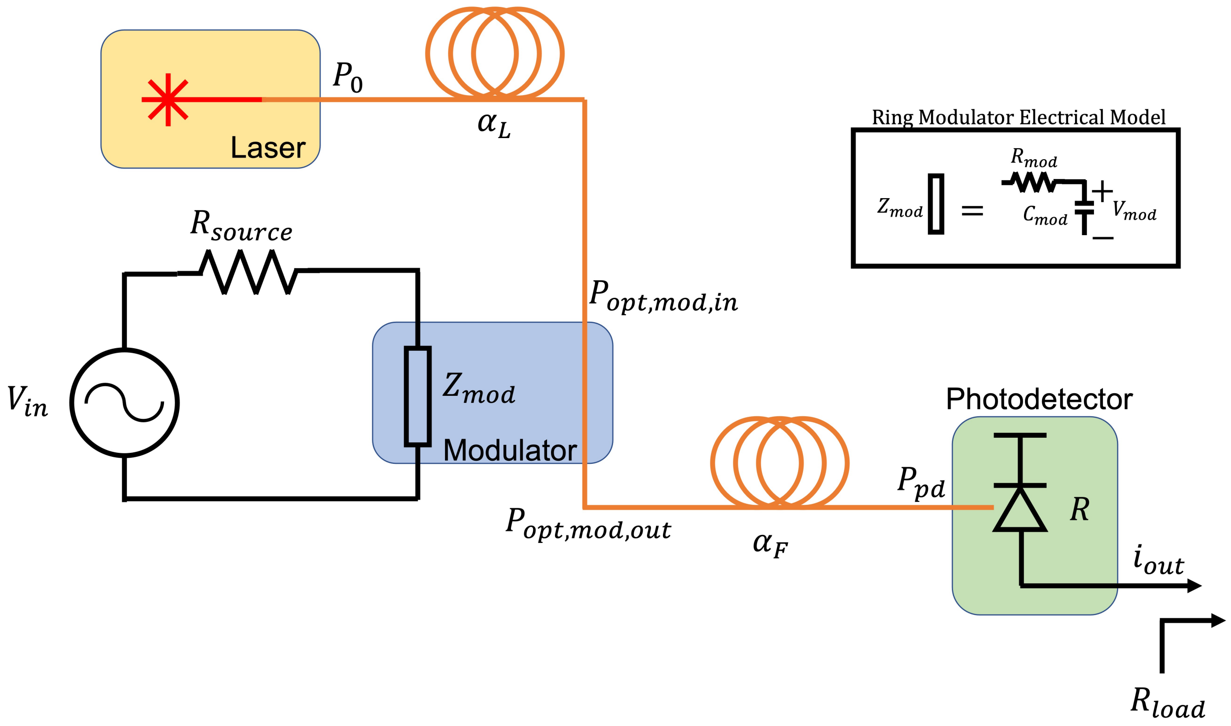

Figure 4.1: Schematic of a passive IMDD optical link. Inset: Simple electrical model for a microring modulator.

h_0 describes the insertion loss of the modulator (in terms of field):

$$h_0 = \left|\frac{E_{out}}{E_{in}}\right|_{DC} \qquad H_0 = |h_0|^2 = \frac{P_{opt,mod,out}}{P_{opt,mod,in}} \tag{4.2}$$

and a linear modulation term h_1 which describes the modulation of the electric field versus an input voltage

$$h_1 = \frac{\partial |E_{mod}|}{\partial v_{in}} \tag{4.3}$$

Under a modulation voltage of $V_{in}(t) = v_{in} \cdot \cos(\omega_{RF} t + \phi(t))$, the electric field at the output of the modulator is given by

$$E_{mod,out} = E_0 e^{j\omega_0 t} \left(h_0 + h_1 \left(v_{in} \cdot \cos(\omega_{RF} t + \phi(t))\right)\right) \tag{4.4}$$

such that intensity of the modulated optical power in the sideband is given by $\Delta P_{mod} = \frac{|h_1|^2}{4} \cdot |v_{in}|^2 \cdot P_{opt,mod,in}$. h_1 can therefore be seen as a measure of the sideband modulation efficiency, defined with slightly different parameters in other work [70].

Let the link comprise an optical fiber with total optical power transmission fraction T_{fiber} (such that $IL = 10^{\frac{T_{fiber}}{10}}$) and a photodetector with responsivity R. The optical loss is broken down into $T_{fiber} = \alpha_L \cdot \alpha_F$, where $\alpha_L = \frac{P_{opt,mod,in}}{P_0}$ is the optical loss from the laser output to the modulator input, and $\alpha_F = \frac{P_{pd}}{P_{opt,mod,out}}$ is the optical loss from the modulator output to the photodetector. At the photodetector, the optical carrier beats with the modulation sidebands to produce a current

$$\begin{aligned} i_{out} &= R \cdot P_{pd} \\ &= R \cdot T_{fiber} \cdot P_{mod,out} \\ &= R \cdot T_{fiber} \cdot |E_{mod,out}|^2 \\ &= R \cdot T_{fiber} \cdot P_0 \bigg(\qquad h_0^2 + \frac{1}{2} h_1^2 v_{in}^2 \\ &\qquad\qquad + 2h_0 h_1 \cdot v_{in} \cos(\omega_{RF} t + \phi(t)) \\ &\qquad\qquad + \frac{1}{2} h_1^2 \cdot v_{in}^2 \cos\left(2\omega_{RF} t + 2\phi(t)\right) \bigg) \end{aligned} \tag{4.5}$$

The resulting current has been broken up into three terms: the DC photocurrent, the AC photocurrent at the frequency of interest, and the second harmonic AC photocurrent that results from the beating of the two sidebands generated by the electro-optic modulator.

Let us consider the ‘effective transconductance’ g_m of the link, $g_m = \frac{i_{out}}{v_{in}}$, which is the ratio of signal current at the output of the link to modulation voltage at the input of the link, Fig. 4.3. From Eq. 4.5, we find that

$$g_m = P_0 \cdot T_{fiber} h_0 \cdot R \cdot 2h_1 \tag{4.6}$$

In general, the modulation coefficient h_1 (and therefore g_m) is a function of modulation frequency, $h_1 = h_1(\omega_{RF})$. The dynamics of the modulation coefficient are affected by both electrical and optical effects, including the mechanism for optical modulation, the electrical interface between the modulator and the signal source, and type of optical modulator and its particular design.

One of the most common mechanisms to achieve optical modulation in silicon photonics platforms is the plasma dispersion effect, which will be discussed in Section 4.4.1. The inset in Fig. 4.1 shows a simple electrical model for such plasma dispersion modulators, which consist of a series resistance and junction capacitance. To achieve the largest optical modulation, the series resistance of both the source and modulator must be minimized, such that the voltage across the junction capacitance can be maximized. The junction capacitance and resistance for microring devices in GlobalFoundries 45nm are on the order of 10s of femto-Farads and 100’s of Ohms respectively [71], resulting in an electrical pole in the 10s of GHz. To achieve optimal modulation at even higher frequencies, appropriate electrical matching networks may be required between the signal source and modulator load.

In additional to electrical effects, the modulator’s optical architecture can impose frequency dependent behavior. Mach-Zehnder modulators, for example, are often long devices due to the weak electro-optic coefficient in silicon photonic platforms [72]. Because of their

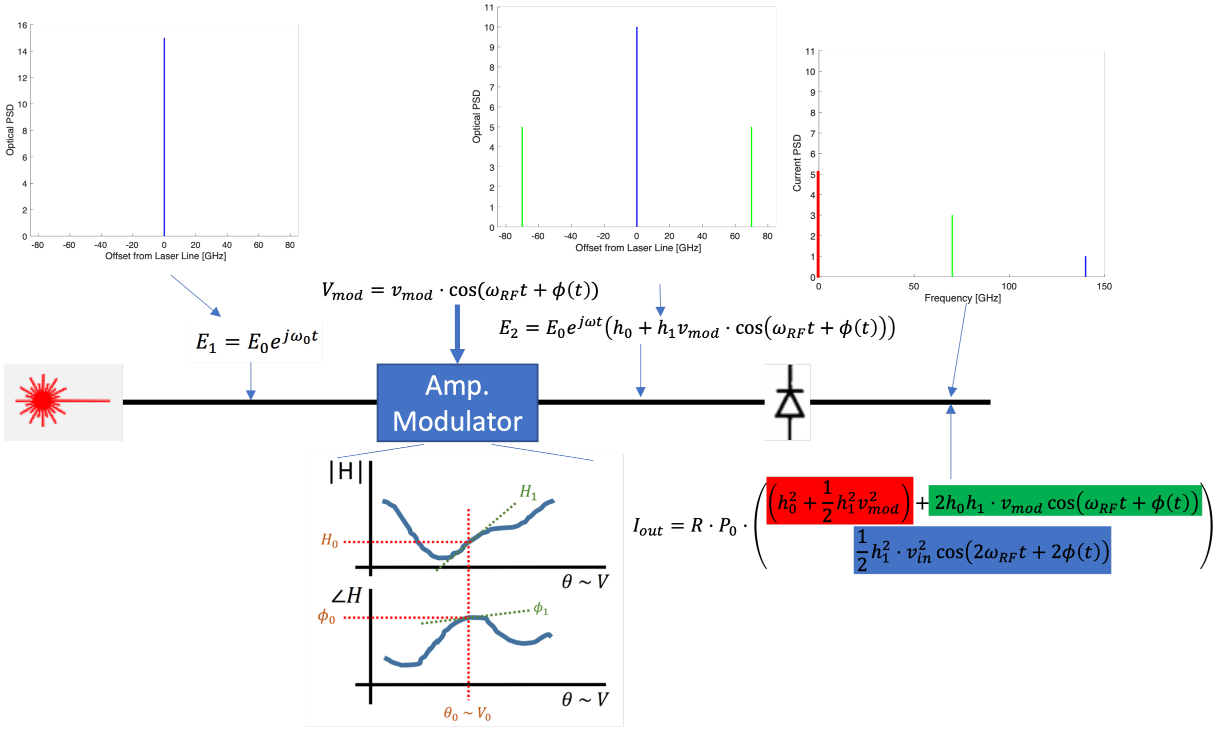

Figure 4.2: Schematic of a passive optical link.

long length, traveling-wave effects cause modulation strength to roll-off with frequency unless traveling-wave electrodes are used to compensate this effect [73]. The dynamics of microring modulators have been studied in numerous works [74, 75], and depend on the optical bandwidth of the Lorentzian resonance, the laser detuning from resonance, and the coupling strength of the ring to bus waveguide. For low modulation frequencies, well below the optical bandwidth of the rings, these frequency effects can be ignored, and the electro-optic modulation strength can be optimized by suitable design choice, as will be shown in Section 4.4.2. For high modulation frequencies, special optical architectures such as dual-ring microring modulators [76] are required to achieve sufficient optical modulation. For the remainder of this study, it is assumed that modulation is occurring at a single frequency, such that $h_1(\omega_{RF})$ already represents the modulation efficiency at the frequency of interest.

Equation 4.6 is broken into different sections. It can be seen that the transconductance gain depends on the optical power P_0 from the laser, the insertion loss along the link $T_{fiber} h_0$, the responsivity of the photodetector R, and the modulation slope h_1. To achieve the highest transconductance gain, each of these factors must be maximized. The following numerical example serves to demonstrate a best-case transconductance that might be achievable in an optical link.

The responsivity of photodetectors depends on their quantum efficiency and the oper-

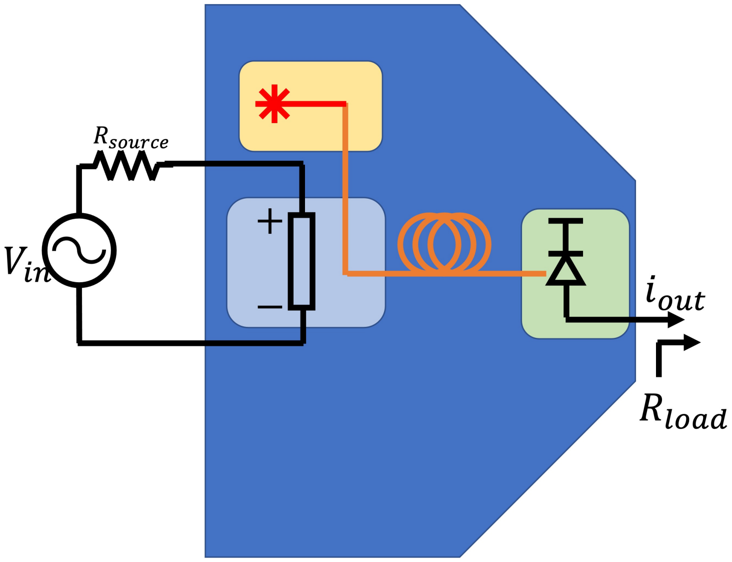

Figure 4.3: Optical link as a Gm stage, which accepts an input voltage and produces an output current.

ating wavelength. Values of $R = 0.6\frac{A}{W} \sim 1\frac{A}{W}$ are achievable with monolithically integrated photodetectors in GlobalFoundries 45nm platform [71]. The next term $T_{fiber}h_0$ must be maximized by minimizing the insertion loss through the link. The peak value, assuming no active optical amplification, is 1, though any actual link will suffer insertion loss from connectors, optical coupling to the chip, and loss from the modulator itself, which typically total to several dB even in well designed links. The modulation slope h_1 depends on the type and design of the electro-optic modulator. As will be derived in later sections, for a microring modulator with resonance shift efficiency of $5\,\mathrm{GHz/V} - 30\,\mathrm{GHz/V}$ (typical for well-designed modulators in GlobalFoundries 45nm platform [77–79]), the linear modulation slope can approach values of roughly $h_1 \approx 0.5\,\mathrm{V^{-1}} - 3\,\mathrm{V^{-1}}$. Thus, we find that the best case transconductance of a well-designed optical link, with an ideal $0\,\mathrm{dB}$ insertion loss, is on the order of $g_m \sim P_0 \cdot 1 \cdot 1\frac{A}{W} \cdot 1V^{-1} \sim P_0\frac{A}{V}$ (with laser power P_0 in Watts). The final parameter is the laser power P_0, which should be maximized to achieve the largest transconductance. While any transconductance can be theoretically achieved by increasing P_0, in practice limitations on laser output power as well as nonlinear absorption in photonics devices limits realistic output laser powers to at most $P_0 = 10\,\mathrm{mW}$. Thus the optimistically best-case optical link transconductance is on the order of $g_m \sim 0.01\frac{A}{V} - 0.05\frac{A}{V}$. In practice, as shall be discussed below, insertion loss ($\sim 6\,\mathrm{dB}$) and limited laser power ($\sim 1\,\mathrm{mW}$) limit the transconductance closer to $g_m \sim 10^{-5} - 10^{-4}\frac{A}{V}$.

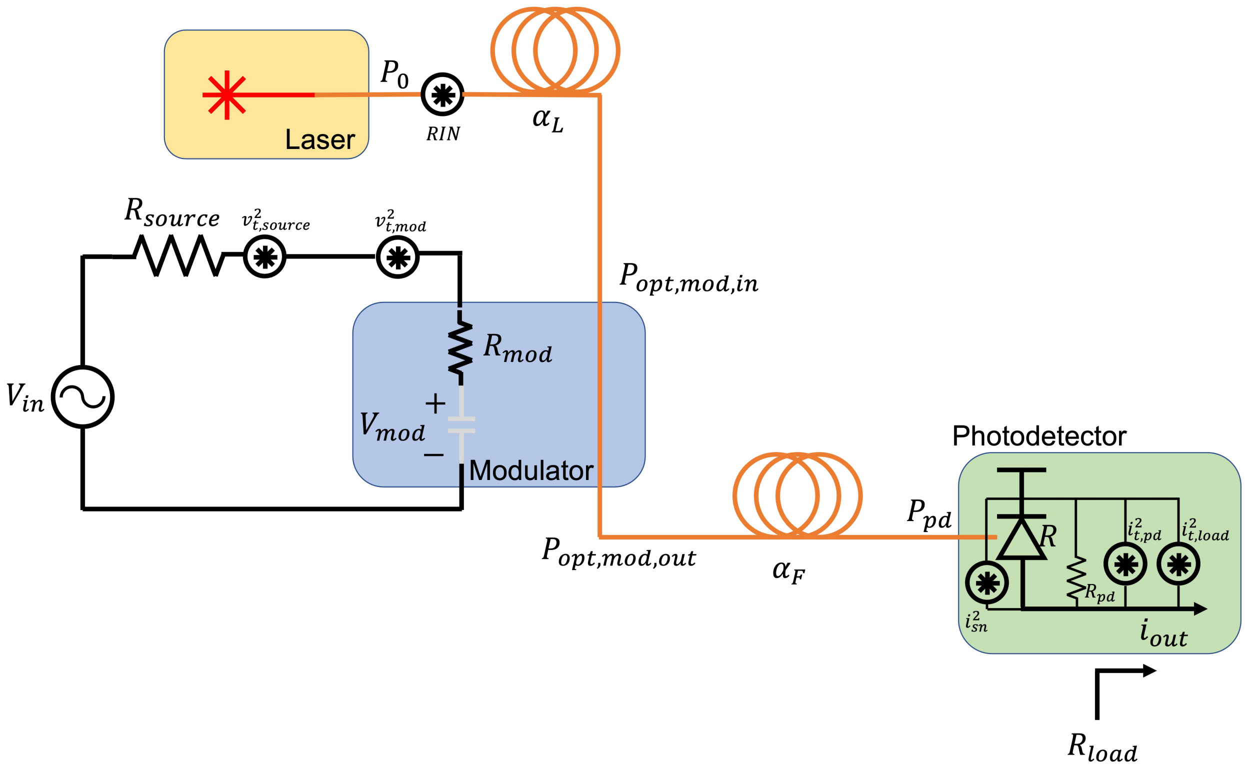

Figure 4.4: Schematic of a passive optical link with noise sources included.

4.2 Noise in Analog Links

In this section, the noise sources affecting analog optical links are discussed. The predominant regions of operation are described, as well as the scaling trends. The noise figure of optical links is then derived. The section concludes by motivating preamplifiers as a means of improving link noise figure. Throughout the following discussion, consider the optical link shown in Figure 4.4. Note that in this analysis, the simplified electrical model shown in the inset of Fig. 4.1 is assumed. Furthermore, it is assumed that the junction capacitance acts as an open circuit (i.e. the reactance is much larger than the modulator resistance or source resistance), which is valid for modulation frequencies sufficiently below the $\sim$ 50 GHz pole frequency.

4.2.1 Noise Sources in Analog Links

4.2.1.1 Thermal Noise

Thermal noise, or Johnson noise, is a fundamental noise source that arises due to the random movement of charge carriers in conductors. Any physical resistor will produce thermal noise.

The mean square noise voltage across a resistor of value R at a temperature T is

$$\left\langle v_t^2 \right\rangle = 4kTR\Delta f \tag{4.7}$$

where $k = 1.38 \times 10^{-23}$ J/K is the Boltzmann constant and Δf is the bandwidth over which the noise is measured. Thermal noise is a white noise source with constant spectral density.

In the optical link represented in Fig. 4.4, there are several elements which contribute thermal noise. First, as mentioned above the input source is assumed to has a physical resistance that contributes a reference input noise into the system, represented by $v_{t,source}^2$. Next, the modulator device has Ohmic resistance which also contributes noise at the input of the system, represented by $v_{t,mod}^2$. The photodetector has Ohmic resistance which contributes thermal noise $i_{t,pd}^2$. Finally, the electrical receiver which loads the photodetector is assumed to have an equivalent input referred thermal noise $i_{t,load}^2$.

4.2.1.2 Shot Noise

Shot noise is a fundamental noise source that arises from the discrete nature of charge flow. The total photocurrent produced by a photodetector can be written as

$$i(t) = \langle I \rangle + i_{sn}(t) \tag{4.8}$$

where $\langle I \rangle$ represents the average photocurrent and $i_{sn}(t)$ represents the shot noise. Because the electron transit through the photodetector follows a Poisson distribution, the noise current has spectral noise density

$$S_{sn}(f) = 2q\langle I \rangle \tag{4.9}$$

where $q = 1.602 \times 10^{-19}$ C is the fundamental charge and the 2 arises from a single-sided PSD [80]. This implies that the mean square shot noise can be expressed as

$$\left\langle i_{sn}^2 \right\rangle = 2q\langle I \rangle \Delta f \tag{4.10}$$

Shot noise spectral density is constant up to frequencies far above the operating bandwidths of links, and thus represents a white noise source. Shot noise can be related to the optical power by noting that $\langle I \rangle = R\langle P_{pd} \rangle$ where R is the responsivity of the photodetector and $\langle P_{pd} \rangle$ is the average power incident on the photodetector.

4.2.1.3 Relative Intensity Noise

Relative intensity noise (RIN) is a fundamental noise source of lasers, which describes the noise fluctuations of the output laser power (intensity). Intensity noise from a laser originates partly from quantum noise sources such as spontaneous emission and partly from classical sources such as thermal fluctuations and cavity vibrations [81]. RIN is defined as

$$RIN = \frac{\langle \Delta P(t)^2 \rangle}{P_0^2} \tag{4.11}$$

where P_0 is the average optical power of the laser and $\Delta P(t)$ is the fluctuation of laser power such that $P_0(t) = P_0 + \Delta P(t)$. RIN is often expressed in the units dB/Hz, and can be related to the photodetector's current as

$$RIN = 10 \log \left(\frac{2 \left\langle i_{rin}^2(t) \right\rangle}{\left\langle I_0 \right\rangle^2 \Delta f} \right) \tag{4.12}$$

where the 2 comes from the single-sided power spectral density, and $\langle i_{rin}^2 \rangle$ and $\langle I_0 \rangle$ represent the mean-square noise current due to RIN and the DC photocurrent. The responsivity cancels out because both optical powers are squared in Eq. 4.11. Equivalently, the mean-square noise current can be expressed as

$$\left\langle i_{rms}^2 \right\rangle = \frac{\left\langle I_0 \right\rangle^2}{2} 10^{\frac{RIN}{10}} \Delta f \tag{4.13}$$

The power spectral density of RIN is not flat, but peaks due to relaxation oscillations in the laser, Fig. 4.5, after which the RIN reduces to the shot noise limit. This implies that for frequencies below the relaxation peak, rms current noise due to RIN scales with average photodetector current squared, whereas above the relaxation frequency RIN current noise scales in the same manner as shot noise, i.e. with a linear relation to photodetector current [80]. Laser data sheets commonly report a single RIN value and bandwidth. For the following discussion, unless otherwise noted, it is assumed that the RIN noise density is constant (valid for sufficiently low frequency links), and where an rms value is required, the RIN is integrated up to the reported bandwidth.

4.2.1.4 Total Output Noise

The contributions from each noise source can be summed to find the total noise current at the output of the photodetector. Using superposition, each noise term is output referred to an equivalent noise current at the photodetector. Recall that because noise power adds, each noise term must be multiplied by the square of the transfer function from the noise source to the output.

$$\begin{aligned} i_{n,total}^2 =& i_{t,source}^2 + i_{t,mod}^2 + i_{rin}^2 + i_{sn}^2 + i_{t,pd}^2 + i_{t,load}^2 \\ =& 4kTR_{source} g_m^2 + 4kTR_{mod} g_m^2 + 10^{\frac{RIN}{10}} \cdot \frac{(P_0 T_{fiber} h_0 R)^2}{2} \\ &+ 2qP_0 T_{fiber} h_0 R + \frac{4kT}{R_{pd}} + i_{t,load}^2 \end{aligned} \tag{4.14}$$

where kT is the Boltzman constant times temperature, R is the responsivity of the photodetector, R_x represents the Ohmic resistance of component x, and g_m represents the transconductance gain of the link (Eq. 4.6). The receive circuit which loads the photodetector is assumed to have an input referred (to the photodetector) current noise power of $i_{t,load}^2$, and

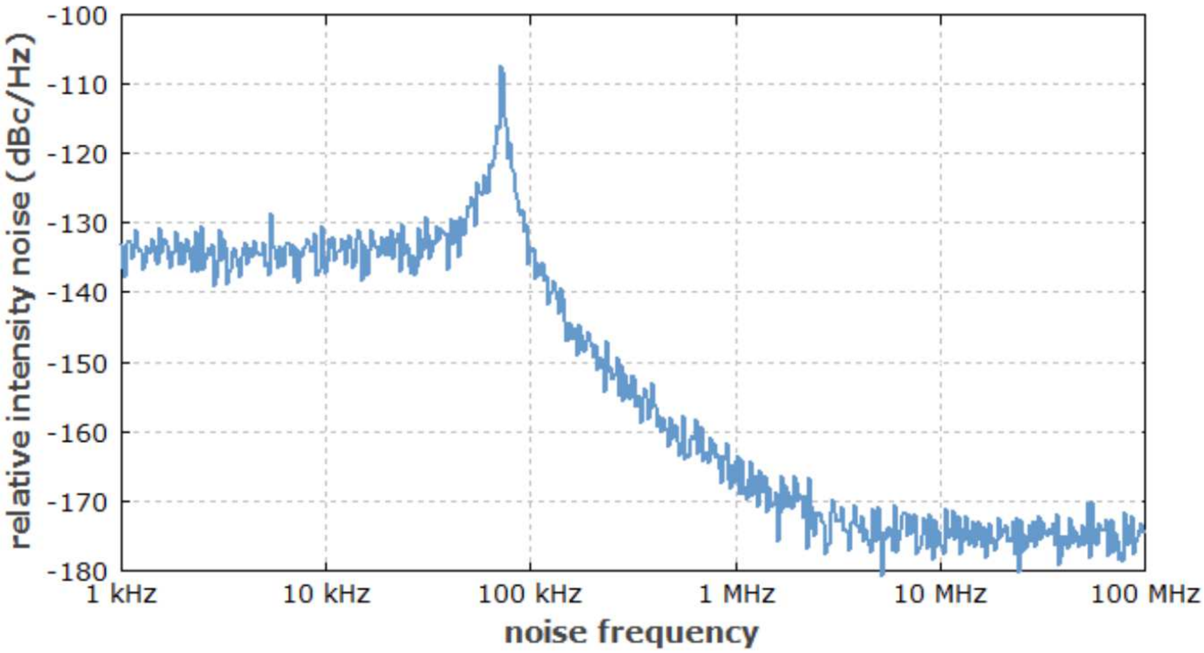

Figure 4.5: RIN power spectral density for a Nd:YAG laser. From [82].

is often dominated by $i^2_{t,load} = \frac{4kT}{R_{fb}}$, where R_{fb} is the feedback resistance of the transimpedance amplifier circuit that loads the photodetector.

Figure 4.6 shows total current noise power and its breakdown as a function of optical power incident on the photodetector for two different RIN levels, and when RIN becomes shot noise limited. The values assumed for responsivity, modulator efficiency, and source and load resistances are typical values that can be achieved in the GF 45nm platform. On the left and center plots, in the RIN-dominated regime, the modulation frequency of interest is lower than the RIN relaxation peak, and the RIN noise power scales as optical power squared. For the left plot RIN $= -145\,\mathrm{dB/Hz}$, which represents a high-end benchtop laser source (such as Santec TSL-570). In this case, there are three regions of optical power in which different noise sources dominate. At very high optical powers, RIN dominates the total output noise. RIN noise scales with optical power squared, as do the thermal noise contributions of R_{source} and R_{mod}. However, because of the low electro-optic coefficient, the optical RIN noise dominates the total output current noise. In addition, it makes sense that RIN dominates over the remaining noise sources at high enough optical power, because the shot noise and other thermal noise sources are either linear with optical power or are constant. At low optical powers, the thermal noise due to the load circuit dominates. This again makes sense, as in the limit as optical power goes to 0, there will be no RIN or shot

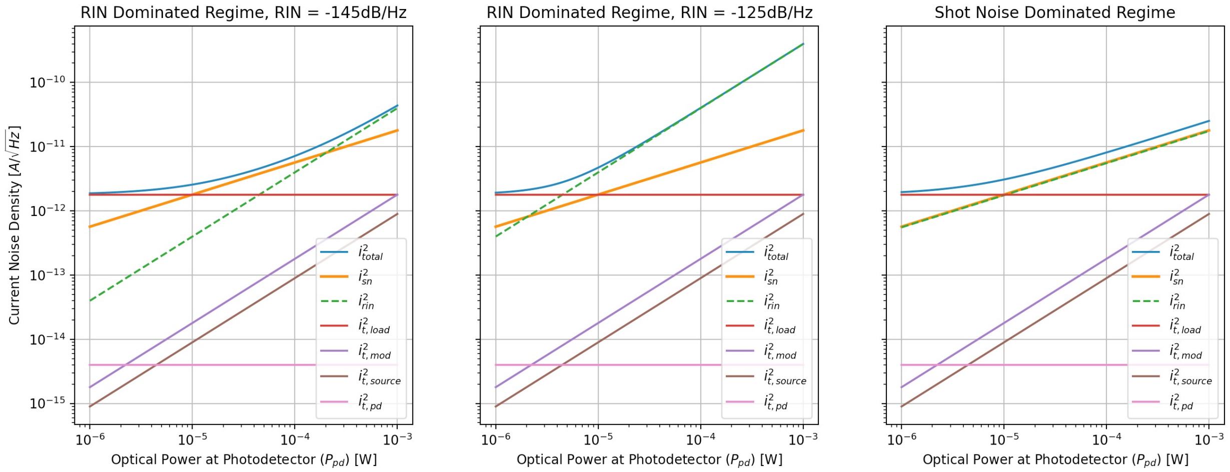

Figure 4.6: Current noise at photodetector output versus incident optical power at the photodetector. (left) RIN dominated regime for modulation frequencies below the RIN relaxation peak, with RIN = $-145\,\mathrm{dB/Hz}$. (center) RIN dominated regime for modulation frequencies below the RIN relaxation peak, with RIN = $-125\,\mathrm{dB/Hz}$. (right) Shot noise dominated regime for modulation frequencies above the RIN relaxation peak. Parameters used are: $T = 290\,\mathrm{K}$, $R = 1\frac{A}{W}$, $R_{pd} = 1\,\mathrm{G}\Omega$, $h_1 = 0.5V^{-1}$, $R_{mod} = 200\Omega$, and $R_{source} = 50\Omega$. The optical parameters leading to h_1 are $\lambda_0 = 1310\,\mathrm{nm}$, $FSR = 17\,\mathrm{nm}$, and a resonance shift efficiency of $5\,\mathrm{GHz/V}$. It is assumed that the input-referred noise current due to the load circuit is $i^2_{t,load} = 2.8 \times 10^{-24} A^2/Hz$ which is roughly the input thermal noise due to a TIA with $5k\Omega$ transimpedance resistor.

noise, and because transconductance drops to 0 as optical power goes to 0, no source or modulator noise will make it to the output of the link. At intermediate optical power levels, shot noise dominates the total current noise. Note that the total noise contributions from the thermal noise of the photodetector itself and from the modulator resistance are very low, and can often be neglected. In the center of Fig. 4.6, RIN = $-125\,\mathrm{dB/Hz}$, which represents the RIN in a multi-wavelength comb laser source (such as the Innolume 1310 Comb). In this regime, the RIN dominates even at low optical powers, and there is no region in which shot noise limits the total output noise current. At sufficiently low optical powers, the thermal noise of the receiver once again dominates the total output noise.

The plot on the right of Fig. 4.6 shows the scenario in which modulation frequency is higher than the relaxation peak in the RIN spectrum. In such cases, RIN drops to the shot noise limit [80]. In these cases, there are only two regions of operation. For sufficiently high optical power, the link noise is limited by shot noise. For low optical powers, thermal noise at the receiver again dominates the link.

4.2.2 Noise Figure

Noise figure is a common measure of the degradation in signal-to-noise ratio (SNR). Noise figure is defined as the ratio of the total output noise power (per unit bandwidth) to the output noise caused by the input source. For matched inputs at standard temperature (290 K), noise figure is found to be

$$NF = 10\log\left(\frac{SNR_i}{SNR_o}\right) = 10\log\left(\frac{s_i/n_i}{s_o/n_o}\right) \tag{4.15}$$

An ideal link should not degrade the SNR at all, which implies $SNR_o = SNR_i$, or $NF = 0\,\mathrm{dB}$. If the entire optical link is treated as a single gain stage, as shown in Fig. 4.3, the output signal and noise powers can be related to the input by

$$s_o = g_i s_i \tag{4.16}$$

$$n_o = g_i n_i + n_a \tag{4.17}$$

where g_i is the intrinsic power gain of the link, and n_a represents the output-referred noise added by the link due to all noise sources (apart from the input source).

This allows the noise factor to be rewritten as

$$NF = 10\log\left(1 + \frac{n_a}{g_i n_i}\right) \tag{4.18}$$

Equation 4.18 is convenient because it highlights that the NF does not depend on the signal, but rather only on the gain and amount of noise added by the link.

The noise figure for the optical link under consideration is computed by substituting Eq. 4.14 into Eq. 4.18

$$NF = 10\log\left(1 + \frac{\left(i^2_{t,mod} + i^2_{rin} + i^2_{sn} + i^2_{t,pd} + i^2_{t,load}\right)R_{load}}{g_i n_i}\right) \tag{4.19}$$

The denominator in Eq. 4.19 is equal to the output noise power, which can be related to the input noise voltage due to an ideal source with resistance R_{source} by

$$\text{output noise power} = g_i n_i = 4kTR_{source} \cdot g_m^2 R_{load} \tag{4.20}$$

resulting in

$$NF = 10\log\left(1 + \frac{i^2_{t,mod} + i^2_{rin} + i^2_{sn} + i^2_{t,pd} + i^2_{t,load}}{4kTR_{source} \cdot g_m^2}\right) \tag{4.21}$$

Plugging in the various expressions for each noise source results in

$$NF = 10\log\left(1 + \frac{4kTR_{mod}g_m^2 + 10^{\frac{RIN}{10}} \cdot \frac{(P_0 T_{fiber} h_0 R)^2}{2} + 2qP_0 T_{fiber} h_0 R + \frac{4kT}{R_{pd}} + i^2_{t,load}}{4kTR_{source} \cdot g_m^2}\right) \tag{4.22}$$

In the regime where RIN is at the shot noise floor, Eq. 4.22 (and Eq. 4.21) can be simplified. In the numerator, the term corresponding to $i_{t,mod}^2$ scales with the square of optical power, as does the denominator term (due to the squared dependence on g_m, Eq. 4.6). Note that all the other noise power terms in the numerator are either constant ($i_{t,pd}^2$ and $i_{t,load}^2$) or scale linearly with optical power (i_{sn}^2 and i_{rin}^2 in the shot-noise regime). Thus at sufficiently high optical powers, the noise figure limits to

$$\lim_{P_{opt}\to\infty} NF = \lim_{P_0\to\infty} = 10\log\left(1+\frac{R_{mod}}{R_{source}}\right) \tag{4.23}$$

At low optical powers, equivalent to low intrinsic link gain, only the constant terms in the numerator are significant as the terms that scale with optical power will approach 0. Thus the output thermal noise due to the load resistance will dominate,

$$\lim_{P_{opt}\to 0} NF = 10\log\left(\frac{1}{g_m^2 R_{source} R_{load}}\right) \tag{4.24}$$

These two equations can be combined to form a limit for noise figure

$$NF >= 10\log\left(1+\frac{R_{mod}}{R_{source}}+\frac{1}{g_m^2 R_{source} R_{load}}\right) \tag{4.25}$$

In Figure 4.7, noise figure is plotted versus optical power at the photodetector for a reference optical link, with the same parameters as used in Fig. 4.6. Three different modulator shift efficiencies (discussed below) are assumed: 5 GHz/V which is achievable using interleaved lateral junctions in GF 45nm platform, 30 GHz/V which can be achieved using MOS-capacitor modulator rings [78], and 50 GHz/V and 100 GHz/V which represents a yet-to-be-achieved shift efficiency targets.

There are several trends worth noting in Fig. 4.7 and Eq. 4.21. First, note that at high optical powers, in the shot-noise RIN regime (right of Fig. 4.7), the NF approaches 7 dB as expected from Eq. 4.25. In the RIN dominated regime (left of Fig. 4.7), even for high optical powers, the NF will never reach this limit, but will be bounded by the RIN of the laser. Next, note the importance of modulator efficiency (represented here by the resonant shift efficiency of a ring modulator) on the NF. A 10 dB improvement to modulator efficiency (and equivalently to the effective link transconductance) results in a 20 dB improvement to NF. Also important to noise figure is the optical power reaching the photodetector. At low optical powers, a 10 dB increase in optical power results in a 20 dB improvement in NF. At higher optical powers, this improvement diminishes as the RIN or 7 dB limits are reached.

It is important to note that while sufficiently high optical power can theoretically reduce the noise figure to acceptable levels in an end-to-end link system, such power levels can rarely be reached in practice. The maximum power is limited by nonlinear absorption effects in the photonic platform or in the modulator, as well as limits to how much output power lasers can produce. In addition, even for reasonable laser powers around 0 dBm to 10 dBm, a significant portion of the power is lost to insertion losses before reaching the photodetector.

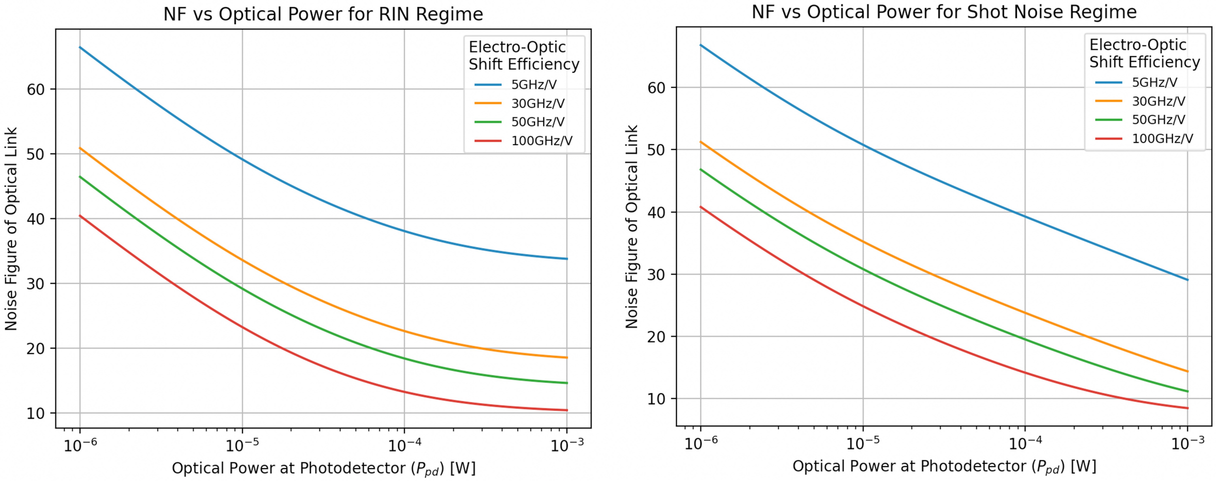

Figure 4.7: Noise figure versus optical power at the photodetector. (left) RIN dominated regime, in which RIN scales with optical power squared. (right) Shot noise dominated regime, in which RIN is at the shot noise limit. Parameters used are: $RIN = -145\frac{dB}{Hz}$, $T = 290\,\mathrm{K}$, $R = 1\frac{A}{W}$, $R_{pd} = 1\,\mathrm{G\Omega}$, $R_{mod} = 200\Omega$, and $R_{source} = 50\Omega$. The optical parameters leading to h_1 are $\lambda_0 = 1310\,\mathrm{nm}$ and $FSR = 17\,\mathrm{nm}$, and the various resonance shift efficiencies are indicated. It is assumed that the input-referred noise current due to the load circuit is $i^2_{t,load} = 2.8 \times 10^{-24} A^2/Hz$ which is roughly the input thermal noise due to a TIA with $5k\Omega$ transimpedance resistor.

While grating couplers have reached peak reported efficiencies of $-0.36\,\mathrm{dB}$ [83], practical coupling efficiencies that could be repeatably achieved in this work peaked at $-2\,\mathrm{dB}$ for individually positioned fibers on a lab setup, or even $-4\,\mathrm{dB}$ per grating when packaging a fiber array with the chip. As three such interfaces are present in most link systems (laser into transmitter, transmitter to fiber, fiber to receiver), total insertion losses can be above $10\,\mathrm{dB}$, resulting in practical optical powers at the photodetector below $100\,\mu\mathrm{W}$. With these limitations, the noise figure can easily reach levels that are unacceptably high for the system.

4.2.3 Preamplification to Improve Noise Figure

In order to improve the noise figure of the link, an amplifier with superior noise performance and sufficient gain can be introduced before the electro-optic modulator. Per the Friis noise formula for an amplifier cascade

$$F = F_1 + \frac{F_2 - 1}{G_1} \tag{4.26}$$

where F is the total noise factor ($NF = 10\log(F)$), F_i is the noise factor of the i^{th} amplifier in the cascade, and G_1 is the gain of the first amplifier. The gain and noise requirements of the preamplification stage depend on the overall link specifications as well as the intrinsic optical link gain achievable in a given technology node. The above analysis provides a framework by which the overall electro-optic link noise figure can be designed.

4.3 Motivating Example of Analog Links for Data Remoting

To motivate the use of analog links, a case study for mm-wave data remoting is presented. Next generation wireless communication systems will rely on massive MIMO (multiple input multiple output) antenna arrays as a mechanism to increase network capacity [84]. Such systems can utilize these large networks of antennas to perform beamforming, enabling spatial-division multiplexing that can transmit and receive multiple streams of data that occupy the same frequency and times. These MIMO arrays can scale to thousands of antennas whose signals must be aggregated across the array to produce the final data streams.

Consider the 'Hydra' multi-user massive MIMO system meant to demonstrate real-time, hardware-efficient, distributed beam-forming at mm-wave carrier frequencies [85]. The receiver frontend that has been designed for the system can target 16 separate data streams (users/beams) and 16 antenna elements, and has a total noise figure of $NF \approx 10\,\mathrm{dB}$ [86]. The frontend bandwidth supported by the receiver is roughly 2 GHz [87]. This system targets the E band (60 GHz to 90 GHz), and has a flexible system architecture that was designed to enable scaling to massive numbers of antennas and users.

Part of Hydra's ability to scale to large numbers of users is its choice of hybrid beam forming architecture, Fig. 4.8. Unlike in a centralized beamforming architecture, in which the data streams from all antennas are remoted to a central processing site, in a hybrid beamforming architecture data streams from groups of antennas are combined at the subarray level to produce a smaller number of user data streams, which are finally aggregated at the central site. This architecture was chosen in particular partially in recognition of the I/O scaling problems that face large antenna arrays: as datarates, signal bandwidths, and number of scale, the cost of remoting the data from the receivers to the central processing site can become prohibitive.

To highlight how analog optical links can help resolve the I/O scaling issue, the power required to remote data from a receiver to a central site is estimated for a digital versus an analog architecture, as shown in Fig. 4.9. In this example, let the system in question have a total RF bandwidth of 10 GHz modulated around a 70 GHz carrier, and assume that the signal is quantized to 10 bits. In the digital remoting scheme in Fig. 4.9a, the received signal is downconverted and amplified via the receiver frontend. The data is then quantized by an ADC, and the digital bits are transmitted to the receiver. The link which remotes the data does not necessarily need to be an optical link in this architecture; however, digital optical links offer power and datarate advantages over electrical links if the transmit distance is long enough [88]. In the analog remoting scheme in Fig. 4.9b, the received signal again passes

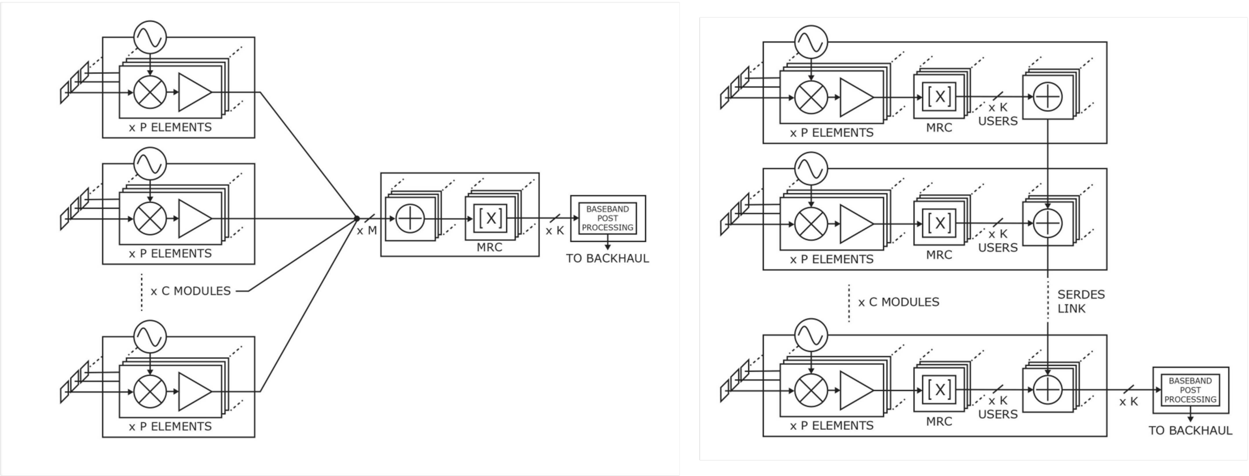

Figure 4.8: Example architectures for beamforming MIMO systems. The signal from each antenna passes through a per-antenna receiver frontend. The signals must then be aggregated and processed at a central site. (left) Centralized beamforming MIMO system in which all receiver streams are remoted to a central site. (right) Distributed / hybrid beamforming MIMO system in which data streams are combined at sub-array level to reduce the information sent to the central site. From [85].

through a receiver frontend. However, unlike in the digital link, the data is not quantized before being modulated into the optical domain. At the end of the optical link, the data is recovered in the electrical domain, and quantized at the central processing site. If desired by the link architecture, and as highlighted in Fig. 4.9b, signal downconversion can be performed in the optical domain by premodulating the optical carrier with LO sidebands. At the photodetector, the modulated optical signal with beat with the LO sideband to produce the IF electrical current output.

The power consumption of the digital style links comes from the power of the RF receiver frontend, the power of the digital optical link, and the power of the quantizer. For this power estimation, the quantizer specifications are designed to be identical between the digital and analog style links, are are therefore ignored in the calculation. Let the electrical receiver have a noise figure of $NF = 10\,\text{dB}$ and consume roughly $10\,\text{mW}$ of power, similar to the performance of the E-band receiver in [87]. The optical digital link is assumed to have a total end-to-end energy efficiency of $1\,\text{pJ/bit}$, which represents a ‘holy grail’ energy efficiency target for digital optical links, which currently achieve best case energy efficiencies of 5-10 pJ/bit [7, 88]. Thus the total power in the digital style link can be computed as:

$$P_{digital} = P_{\text{RX frontend}} + \text{Datarate} \cdot \text{Number bits} \cdot 1\,\text{pJ/bit} \tag{4.27}$$

The analog link is designed to achieve the same bandwidth and end-to-end noise figure as the RF receiver in the digital style link. This is done so that the two link architectures

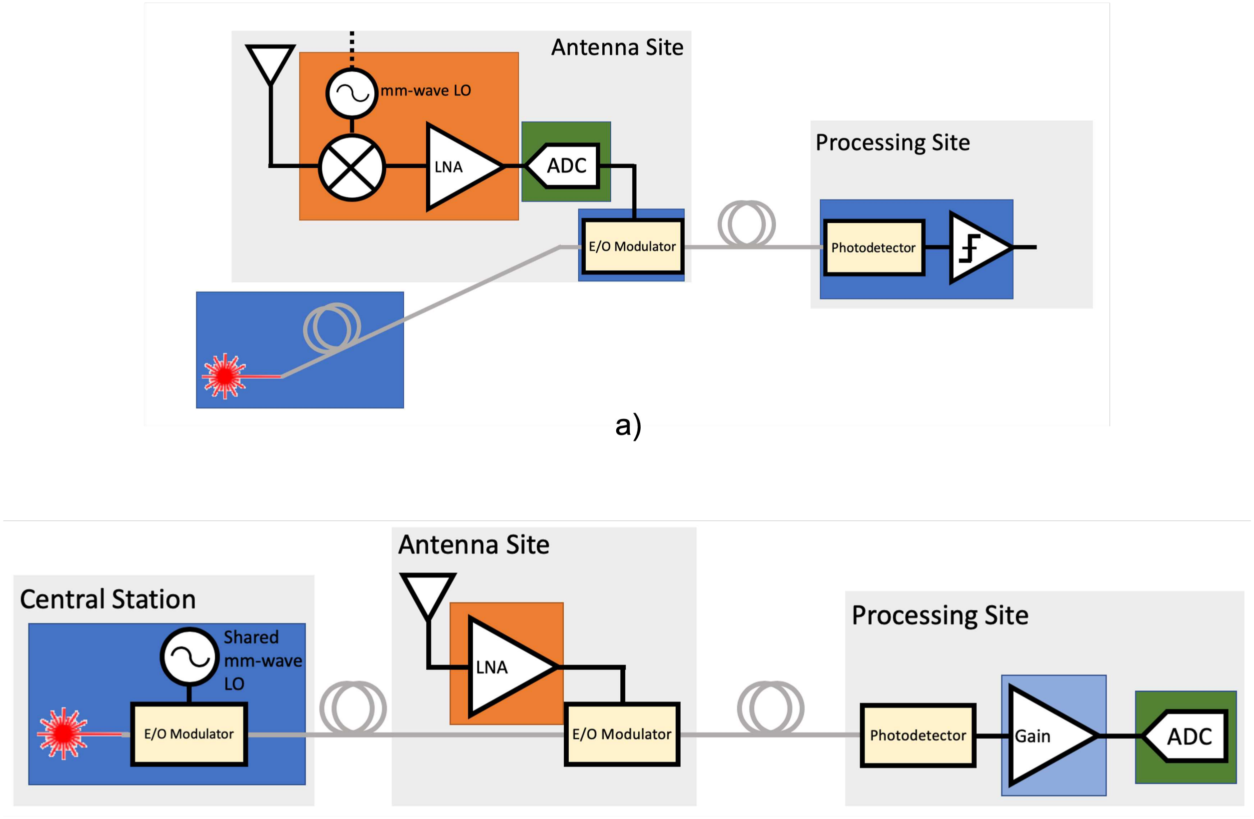

a)

b)

Figure 4.9: a) Digital data remoting architecture. After the receiver, data is quantized, and digital bits are sent to the receiver over the optical link. b) Analog data remoting architecture. After the amplifying receiver, the analog link is modulated with the analog data. Beating at the photodetector against a reference LO sideband can produce a downconverted signal in the electrical domain. The data is quantized at the central site. Components of the link are color coded for clarity: orange represents the RX frontend, blue represents the 'optical link' component, and green represents the quantizer component.

can be compared as equally as possible. Furthermore, the receiver circuit in the central processing site is provisioned to provide sufficient swing such that the ADC specifications in the analog link are identical to the ADC required in the digital link. The optical power and link's intrinsic gain depend on various technology parameters including the required optical bandwidth and the shift efficiency. For this estimation, the optical modulator is designed as a single-ring modulator with optical bandwidth of 75 GHz required to support the E-band signal. Note that the modulator must support the bandwidth of the full RF carrier, rather than just the signal bandwidth. Using the noise figure model presented above, the optical

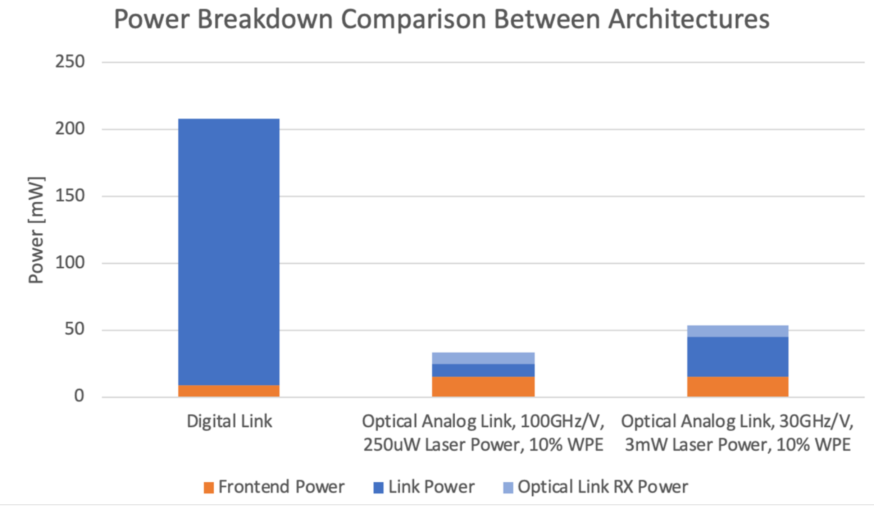

Figure 4.10: Power breakdown for digital versus analog style links. Digital link assumes 1 pJ/bit energy efficiency of the optical link. Analog link assumes a responsivity of 0.5 A/W, 4 dB insertion loss across the link, and shift efficiencies of 100 GHz/V and 30 GHz/V.

power required to achieve a given optical link noise figure can be determined. In order to reduce the overall noise figure, it is assumed that a series of cascaded E-band LNAs can be used to amplify the signal from the antenna. For this model, the LNA is assumed to achieve similar performance to [89]: 12 dB gain with $NF = 4$ dB in the W-band while consuming 5 mW. Finally, to calculate the true power cost of the optical link, a wallplug efficiency of 10% is assumed for the laser. Thus the total power in the analog style link can be computed as

$$P_{analog} = P_{\text{RX LNA frontend}} + \frac{P_{laser,opt}}{\text{Laser Wallplug Efficiency}} + P_{\text{RX central site}} \tag{4.28}$$

Figure 4.10 shows the results of the power estimation for two different parameters. Note that the colors in Fig. 4.10 correspond to the colors of the different components in Fig. 4.9. On the left, the digital link power consumption is shown to be nearly 200 mW for this channel. The power consumed by the RX frontend is dominated by the ‘link power’ of the 1 pJ/bit digital optical transceiver. The central column shows the power breakdown for an analog optical link, assuming a shift efficiency of 100 GHz/V, which requires an output laser power of only 250 μW (or wallplug power of 2.5 mW. The right column shows the power breakdown for an analog optical link assuming 30 GHz/V shift efficiency. This efficiency requires 3 mW output laser power, or 30 mW total wallplug power. The RX frontend of the analog style links uses more power than the RX frontend in the digital style link because the analog link requires several LNA stages to provide sufficient gain such that the noise figure of the analog link is equal to that of the digital style link.

This example shows the potential power savings that analog style optical links can provide over digital style links. The primary benefit comes as the bandwidth and resolution of the system increase. In the digital style link, a fixed energy cost is paid for every additional bit that is transmitted. In the analog style link, some power is spent to provide sufficient electrical gain and sufficient optical power needed to achieve a reasonable noise figure, but does not scale as steeply with increased effective datarate.

4.4 Analog Modulation of Microring Resonators

In the preceding sections, the noise performance of analog optical links was derived without any special attention to the behavior of the optical modulator itself. The performance of microring resonators as optical modulators for analog style links is now evaluated. The section begins by providing an overview of the mechanisms by which a modulating voltage affects a change in optical behavior. Next, the static sensitivity of microring modulators is discussed, and the optimal sensitivity is derived. In the following sections, the linearity and noise performance of microring modulator based analog links is evaluted.

4.4.1 Overview of Electro-Optic Modulation

The primary building block for electro-optic modulators is the optic phase shifter. Optical phase shifters convert a change in voltage into a phase change of the propagating optical wave, and can be used to create constructive or destructive interference that leads to intensity modulation.

In silicon photonic platforms, the primary electro-optic modulation mechanism is the plasma dispersion effect [90]. The plasma dispersion effect relates the change in refractive index and loss of a material to the concentration of free charges in the material, and can be phenomenologically expressed as

$$\Delta n(\lambda) = -A\lambda^2 \Delta N^a - B\lambda^2 \Delta P^b \tag{4.29}$$

$$\Delta \alpha(\lambda) = C\lambda^2 \Delta N^c + D\lambda^2 \Delta P^d \tag{4.30}$$

where n is the refractive index; α is the loss; ΔN and ΔP represent changes in the electrical carriers in the medium; and A, B, C, D, a, b, c, and d represent fitting coefficients [91]. For silicon, these constants are given in Table 4.1 [92] (note that for wavelength-specific coefficients, the λ^2 term is excluded from Eqs. 4.29 and 4.30).

Carrier concentration is modulated by means of a PN junction. A changing electrical voltage applied across a PN junction will alter the depletion width of the junction, thus changing the effective number of free carriers seen by the optical mode, which changes the optical material properties per Eqs. 4.29 and 4.30. A thorough exploration of the behavior and design tradeoffs in modulator junction design is given in [93].

Microring resonators, discussed at length in Section 3.2, can be used as microring modulators by embedding PN junctions within the ring structure. Figure 4.11b shows a schematic

	WL Independent	1310nm	1550nm
A	3.64×10^{-10}	2.98×10^{-22}	5.4×10^{-22}
B	3.51×10^{-6}	1.25×10^{-18}	1.53×10^{-18}
C	3.52×10^{-6}	3.48×10^{-22}	8.88×10^{-21}
D	2.4×10^{-6}	1.02×10^{-19}	5.84×10^{-20}
a	1	1.016	1.011
b	0.8	0.835	0.838
c	1	1.229	1.167
d	1	1.089	1.109

Table 4.1: Coefficients for plasma dispersion effect in silicon, from [92]

representation of a microring modulator with lateral interleaved PN junctions. The optical mode confined within the looped waveguide of the ring overlaps with the depletion region formed by these PN junctions, and thus allows for modulation of the effective index of the ring. A 3D rendering of the microring modulator showing the silicon PN junctions and the anode and cathode wiring is shown in Fig. 4.11c.

Recall from Eq. 3.8 that a ring resonator has thru port power transmission given by

$$P_t = |E_t|^2 = \frac{|t_i|^2 + a^2|t_d|^2 - 2a|t_i||t_d|\cos\theta}{1 + a^2|t_i|^2|t_d|^2 - 2a|t_i||t_d|\cos\theta} \tag{4.31}$$

and that θ represents the round trip phase accumulated by light as it propagates once around the ring

$$\phi = \beta L = \frac{2\pi}{\lambda} n_{eff} L \tag{4.32}$$

and from Eq. 3.3, $a = e^{-\frac{\alpha L}{2}}$ is the amplitude loss factor for a single trip around the ring. For a microring modulator, these equations can be updated by noting the voltage dependence of θ and α, i.e. $\theta = \theta(V) = \frac{2\pi L}{\lambda} n_{eff}(V)$ and $a = a(V) = e^{-\frac{\alpha(V)L}{2}}$.

Figure 4.12 demonstrates how a microring modulator can be used to perform intensity modulation. The index modulation is calculated using the diode depletion model, with doping concentrations $N_D = 5 \times 10^{17}$ cm^{-3}, $N_A = 5 \times 10^{17}$ cm^{-3}, a feature width of 500 nm, and an optical confinement factor of 1. The ring is designed to be critically coupled, and has a total $Q = 8200$ and FWHM bandwidth of 28 GHz. The transmission response versus wavelength is shown for three different voltage biases. As the voltage is changed, the ring resonance wavelength shifts. In this case, a 1 V change in voltage results in a 16 pm or 2.8 GHz shift in resonance; the ring is said to have a shift efficiency of 2.8 GHz/V. For a fixed input wavelength, this shift in ring response corresponds to a change in transmission power at the thru port, resulting in intensity modulation. From Fig. 4.12, it is clear that the laser offset (or bias) relative to the ring's resonance greatly affects the intensity modulation efficiency of the ring.

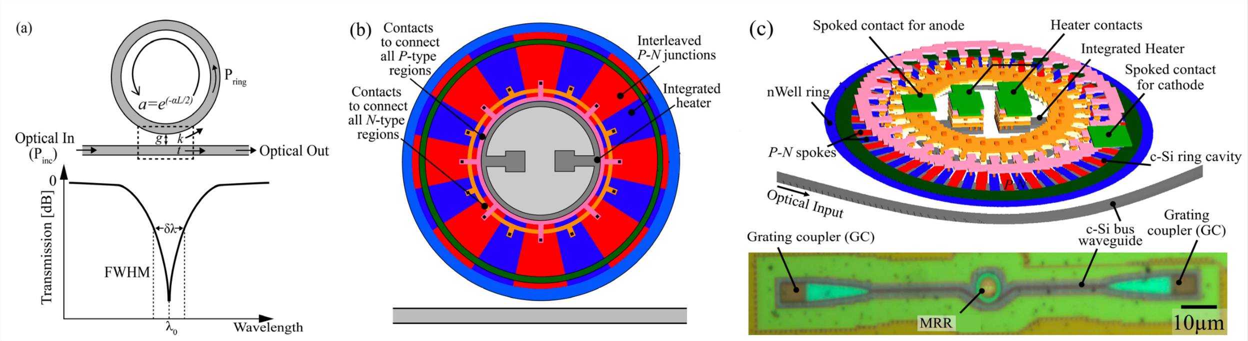

Figure 4.11: Microring modulator structure, from [71]. a) The schematic representation of a microring modulator, and the static spectral transmission response from input port to thru port. b) A schematic showing the alternating P and N doping regions that form the spoked lateral PN junctions within the microring. c) (top) 3D structure of a microring modulator, showing the wiring required to contact each anode and cathode segment. (bottom) A micrograph of a microring modulator implemented in GlobalFoundries 45RFSOI platform.

As seen in Section 4.2.2, achieving the largest intensity modulation for a given voltage change will result in the best noise figure for the link. Thus, it is critical to optimize the design of the modulator and select the optimal bias wavelength of the laser to create the largest modulation efficiency. The next section derives these optimal conditions for static or low frequency ring modulation.

4.4.2 Static Ring Modulator Sensitivity Optimization

In order to find the optimal ring design parameters and laser offset condition for intensity modulation, consider the input to thru port ring transfer function, derived by the coupled-modes in time (CMT) formalism Eq. 3.36, and reproduced below

$$\frac{s_t}{s_i} = \frac{j\left(\omega - \omega_0\right) + \frac{1}{\tau} - \mu_i^2}{j\left(\omega - \omega_0\right) + \frac{1}{\tau}} \tag{4.33}$$

The CMT formalism is chosen over the spatial-mode coupling equations because the elegance of the results emerge more clearly; the two formalisms produce identical results. To determine the optimal bias point which provides maximum modulation efficiency, the power transfer function is calculated

$$\frac{P_{thru}}{P_{in}} = \left|\frac{s_t}{s_i}\right|^2 = \frac{\Delta\omega^2 + \left(r - 2r_i\right)^2}{\Delta\omega^2 + r^2} \tag{4.34}$$

where $\Delta\omega = \omega - \omega_0$ is the bias point of the laser with respect to the ring resonance, $r = r_i + r_t + r_d = \frac{1}{2}\text{FWHM}_\omega$ is the total loss rate of energy in the ring, and $r_i = \frac{\mu_i^2}{2}$ is the energy loss rate due to coupling between the ring resonator and the input waveguide. The

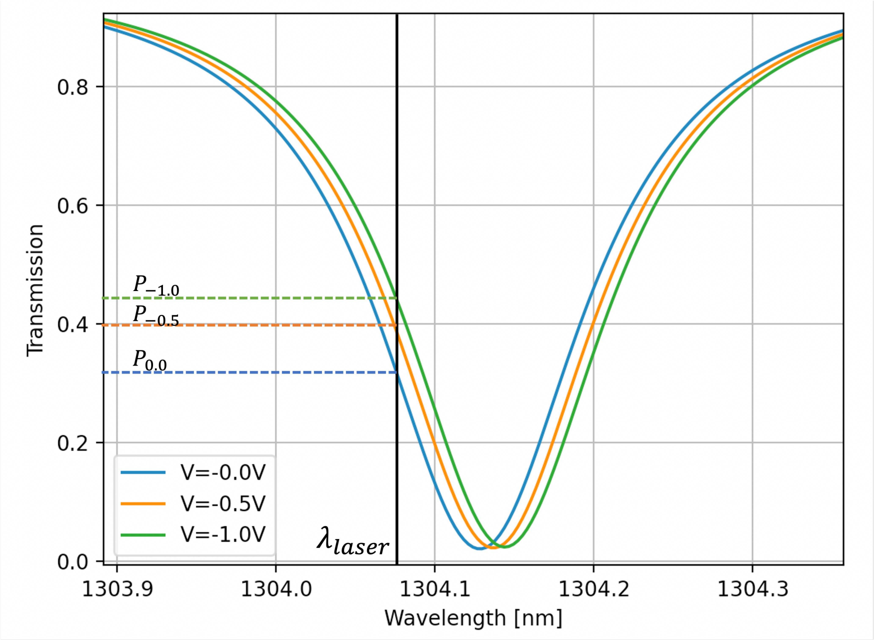

Figure 4.12: Modeled power transmission spectra for a microring modulator under three bias voltages. The ring has a FWHM bandwidth of 28 GHz and is designed to be critically coupled. The quality factor is $Q = 8200$.

relationship between $\Delta\omega$ and $\Delta\theta$ from the spatial mode formalism (or $\partial\omega$ and $\partial\theta$) can be found by

$$\Delta\theta = \Delta\omega \frac{n_g L}{c} \quad \rightarrow \quad \Delta\omega = \left(\frac{c}{n_g L}\right)\Delta\theta = \left(\frac{c \cdot FSR_\lambda}{\lambda^2}\right)\Delta\theta \tag{4.35}$$

Note that in this analysis, it is assumed that a change in voltage only induces a change in refractive index n, which induces a change in θ or ω. It ignores changes to α, which would affect the parameter r in Eq. 4.34. From Fig. 4.12 it can be seen that this is a safe assumption as the transmission on resonance does not change significantly with voltage and the resonance shape remains similar across voltage.

Maximum modulator efficiency occurs when the change in output current of the photodetector is maximized for a given change in applied input voltage. For intensity modulated direct detection links, in which the intensity of the modulated light is directly impinged on a photodetector, maximizing change in photocurrent is equivalent to maximizing the change in thru port power of the modulator. Using the static Lorentzian transfer function, the sensitivity of the modulator is defined as

$$S_\omega = \frac{\partial \frac{P_{thru}}{P_{in}}}{\partial \Delta\omega} = \frac{8\Delta\omega r_i \left(r - r_i\right)}{\left(\Delta\omega^2 + r^2\right)^2} \tag{4.36}$$

Note that the sensitivity depends not only on the ring design parameters but also on the bias offset $\Delta\omega$ at which the laser is located relative to the ring resonance. Note also that this sensitivity is defined with respect to changes in ω, or resonance detuning. If sensitivity to applied voltage is desired, this can be found by the chain rule

$$S_V = \frac{\partial \frac{P_{thru}}{P_{in}}}{\partial V} = \frac{\partial \frac{P_{thru}}{P_{in}}}{\partial \Delta\omega} \cdot \frac{\partial \Delta\omega}{\partial V} \tag{4.37}$$

where $\frac{\partial \Delta\omega}{\partial V}$ is often expressed as the resonance shift efficiency (in GHz per volt) and is found through modeling or experiment. Thus, S_ω represents the 'photonic sensitivity' and captures the optimal optical design parameters.

The optimal bias offset between the laser wavelength and resonance wavelength can be found by maximizing Eq. 4.36 over $\Delta\omega$:

$$\begin{aligned} 0 &= \frac{\partial S_\omega}{\partial \Delta\omega} = \frac{8r_i(r-r_i)\left(r^2-3\Delta\omega^2\right)}{\left(\Delta\omega^2+r^2\right)^3} \\ \rightarrow \Delta\omega_{opt} &= \pm\frac{r}{\sqrt{3}} = \pm\frac{\text{FWHM}_\omega}{2\sqrt{3}} \\ \rightarrow f_{offset} &= \pm\frac{\text{FWHM}_{\text{Hz}}}{2\sqrt{3}} \end{aligned} \tag{4.38}$$

It is found that the change in power is maximized when the laser is offset from the ring resonance by $\frac{\text{FWHM}_{\text{Hz}}}{2\sqrt{3}}$. Note that this optimum does not depend on the ring coupling parameters, and thus applies regardless of if the ring is over, under, or critically coupled. Plugging Eq. 4.38 into Eq. 4.36 yields

$$S_{\omega,max} = \frac{3\sqrt{3}r_i\left(r-r_i\right)}{2r^3} \tag{4.39}$$

The coupling parameters which optimize sensitivity and modulator efficiency can now be determined. A given process technology, ring geometry, and doping structure will determine the intrinsic quality factor, which sets r_0. In some schemes, ring modulators require a target FWHM bandwidth, which therefore constrains the total r. The free parameter which must therefore be set is r_i (the input port coupling strength), from which r_d (the drop port coupling strength) is determined. Differentiating Eq. 4.39 with respect to r_i, and assuming r is fixed by choice of FWHM bandwidth, it can be found that $S_{\omega,max}$ is maximized as

$$r_i = \frac{r}{2} = \frac{\text{FWHM}_\omega}{4} \tag{4.40}$$

$$r_d = r - r_0 - r_i = \frac{\text{FWHM}_\omega}{2} - r_0 - \frac{\text{FWHM}_\omega}{4} = \frac{\text{FWHM}_\omega}{4} - r_0 \tag{4.41}$$

$$S_{\omega,max} = \frac{3\sqrt{3}}{8r} = \frac{3\sqrt{3}}{4\text{FWHM}_\omega} = \frac{3\sqrt{3}}{8\pi\text{FWHM}_{\text{Hz}}} \tag{4.42}$$

It is interesting to note that at the optimal laser bias f_{offset}

$$\frac{P_{thru}}{P_{in}} = \frac{\Delta\omega^2 + (r - 2r_i)^2}{\Delta\omega^2 + r^2} \overset{r_i=\frac{r}{2}}{=} \frac{\Delta\omega^2}{\Delta\omega^2 + r^2} \overset{\Delta\omega_{opt}=\frac{r}{\sqrt{r}}}{=} \frac{\frac{r^2}{3}}{\frac{r^2}{3} + r^2} = \frac{1}{4} \tag{4.43}$$

the output power is one quarter the input power (i.e. an insertion loss of −6 dB) regardless of FWHM bandwidth. Note also that with $r_i = \frac{r}{2}$, then at resonance

$$\frac{P_{thru}}{P_{in}} = \left|\frac{s_t}{s_i}\right|^2 = \frac{\Delta\omega^2 + (r - 2r_i)^2}{\Delta\omega^2 + r^2} \overset{\Delta\omega=0}{=} \frac{(r - 2r_i)^2}{r^2} \overset{r_i=\frac{r}{2}}{=} 0 \tag{4.44}$$

This implies that in the cases where FWHM bandwidth constrains the ring design, the optimum sensitivity occurs for rings designed to be critically coupled. Figure 4.13 shows the ring transfer functions and peak sensitivities for different FWHM targets. The sensitivity traces are calculated numerically to validate the derived optimization points. Note that all the optimized rings are critically coupled, and that the insertion loss is $-6dB$ at the optimal sensitivity points.

If FWHM bandwidth is not a system constraint, then maximizing Eq. 4.39 can be done over two free variables: r_i and r_d. In the special case of an all-pass ring configuration, in which there is no drop port and thus $r_d = 0$, the maximum sensitivity becomes

$$S_{\omega,max,ap} = \frac{3\sqrt{3}r_i\left((r_0 + r_i + r_d) - r_i\right)}{2(r_0 + r_i + r_d)^3} = \frac{3\sqrt{3}r_i r_0}{2(r_0 + r_i)^3} \tag{4.45}$$

As r_0 is fixed by technology constraints, Eq. 4.45 can be optimized over r_i,

$$0 = \frac{\partial S_{\omega,max,ap}}{\partial\Delta\omega} = \frac{3\sqrt{3}}{2}\frac{r_0\left(r_0 - 2r_i\right)}{\left(r_0 + r_i\right)^4} \tag{4.46}$$

$$\rightarrow r_i = \frac{r_0}{2} \tag{4.47}$$

$$\rightarrow S_{\omega,max,ap} = \frac{2\sqrt{3}}{9r_0} = \frac{4\sqrt{3}}{9}\frac{Q_0}{\omega_0} = \frac{2\sqrt{3}}{9\pi c}Q_0 \cdot \lambda_0 \tag{4.48}$$

$$\text{at} \qquad \mathrm{FWHM_{Hz}} = \frac{3r_0}{2\pi} = \frac{3}{4\pi}\frac{\omega_0}{Q_0} = \frac{3c}{2}\frac{1}{Q_0 \cdot \lambda_0} \tag{4.49}$$

where we have used $Q = \frac{\omega_0}{\mathrm{FWHM}_\omega} \rightarrow 2r_0 = \frac{\omega_0}{Q_0}$ to relate the intrinsic quality factor with the amplitude decay rate. Note that in this all-pass filter case, the optimum sensitivity occurs in the undercoupled regime ($r_i < r_0$) as opposed to the FWHM-constrained case, in which optimum sensitivity occurs for critical coupling ($r_i = \frac{r}{2} = r_0 + r_d$). Figure 4.14 shows the peak sensitivity and FWHM of an optimally designed allpass modulator versus the intrinsic quality factor.

In this section, the optimal design to maximize modulator sensitivity has been derived. For intensity modulated direct detection links, the optimal sensitivity decreases linearly with FWHM bandwidth. The optimal laser offset was found to be proportional to the FWHM bandwidth. These results provide guidelines for designers when considering ring design requirements.

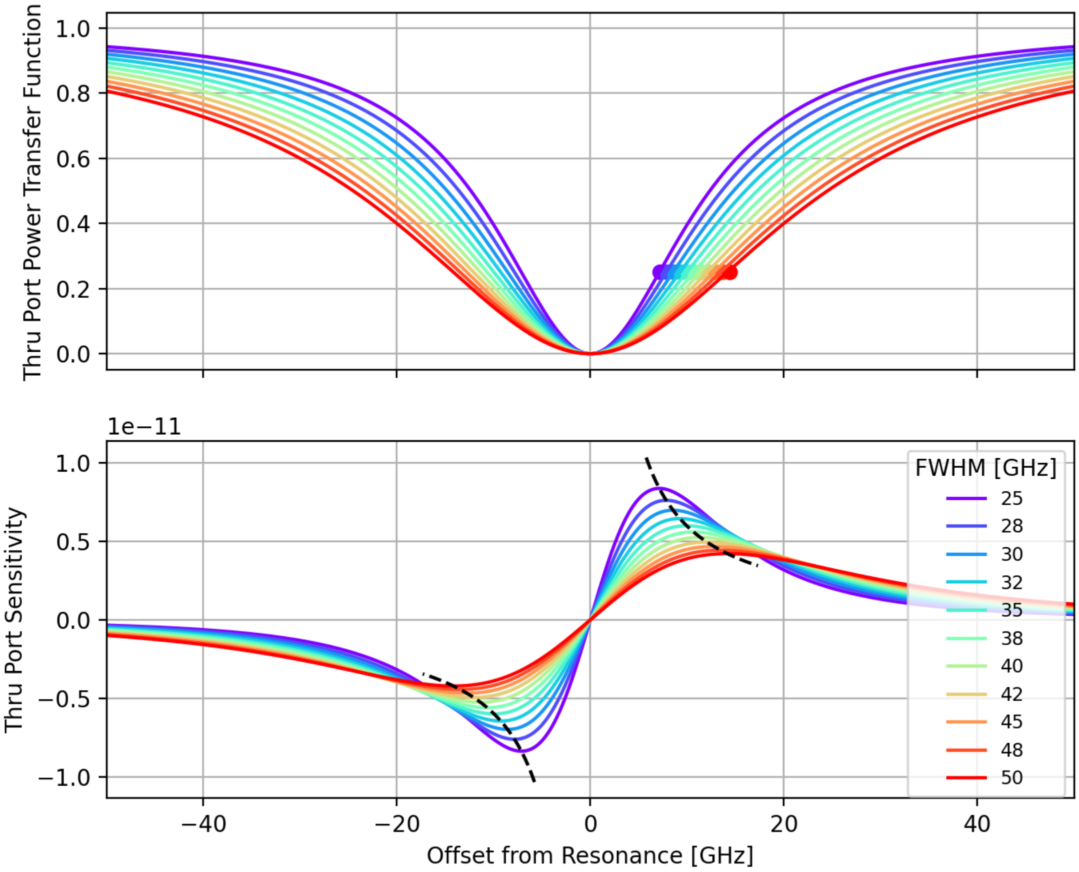

Figure 4.13: Optimal ring design to maximize sensitivity S_ω at a given FWHM bandwidth and for a given Q_0. (top) Ring transfer functions for each target FWHM bandwidth. (bottom) Sensitivity versus laser bias offset from resonance. The black dashed line plots the derived maximum. Optical parameters are $Q_0 = 20000$, $FSR = 17nm$ and $\lambda_0 = 1310nm$.

4.5 Linearity and Noise in Microring Modulators

In addition to noise performance, another key metric for analog modulation is linearity. In RF systems, linearity is critical to avoid generating distortions that can cause in-band and out-of-band interference that lead to poor signal integrity. In this section, a brief review of linearity metrics is provided. The linearity of microring modulators is then investigated, followed by an analysis of the noise performance of microring modulators. Finally, the theoretical linearity behavior of microrings is verified through measurement of a microring

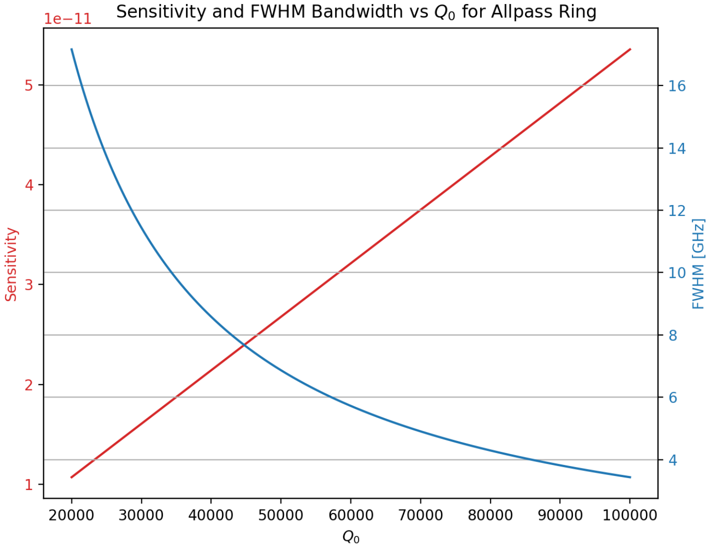

Figure 4.14: Peak sensitivity S_ω and FWHM bandwidth for an optimally designed allpass modulator versus intrinsic quality factor. Optical parameters are $FSR = 17nm$ and $\lambda_0 = 1310nm$.

modulator implemented in GlobalFoundries 45nm CLO platform.

4.5.1 Review of Linearity Metrics

Unlike an ideal linear amplifier, physical amplifiers and modulators exhibit nonlinear behavior that can impact signal quality. It is assumed that the input/output transfer function can be described by a power series

$$s_o = a_1 s_i + a_2 s_i^2 + a_3 s_i^3 \ldots \tag{4.50}$$

If the input signal is a sinusoidal waveform $s_i = S_i \cos(\omega t)$, the odd order distortion power produce additional linear terms that depend on signal amplitude and contribute to gain compression or expansion. In addition to gain compression, the higher order terms generate sidebands in the frequency domain which can cause interference with signals both inside and outside the signal-band of interest.

Of particular interest are the ratios between the fundamental output tones and the second and third order intermodulation products that are generated when two different modulation frequencies are applied to the input. These distortion metrics can be found from the power series in Eq. 4.50 as

$$IM2 = \frac{\text{Amplitude of Second Order Intermodulation Tone}}{\text{Amplitude of Fundamental Tone}} = \frac{a_2}{a_1}S_i \tag{4.51}$$

$$IM3 = \frac{\text{Amplitude of Third Order Intermodulation Tone}}{\text{Amplitude of Fundamental Tone}} = \frac{3}{4}\frac{a_3}{a_1}S_i^2 \tag{4.52}$$

As the input signal power increases, the magnitude of these second and third order intermodulation products will eventually equal the magnitude of the fundamental tone. These intercept points are called the second and third order intercept points (IP2 and IP3, respectively). The input amplitudes at which these intercepts occur are called the second and third order input intercept points. While IM2 and IM3 depend on the specific input amplitude being applied to the amplifier, the IIP2 and IIP3 points are independent of input signal and thus provide a metric for the linearity of the amplifier. These trends are highlighted in Figure 4.15, with input and output intercept points labeled. Also note the slopes of the fundamental tone, and second and third order intermodulation products are 1 : 1, 2 : 1, and 3 : 1. Thus, given the IIP2 and IIP3 points, the IM2 and IM3 values can be found for any input power.

4.5.2 Linearity of Microring Modulators

An analytic derivation of the linearity behavior of microring modulators requires performing Taylor series expansion on the thru port power transfer function from Eq. 4.31. The voltage dependence of both θ and a through Eqs. 4.29 and 4.30 need to be considered. Such analysis would quickly become encumbered and tedious.

Instead, the linearity performance is evaluated in simulation across a range of input parameters to determine behavior trends. A Simulink framework [94] is used to capture the full behavior of the microring modulators. The framework utilizes an analytic signal representation at an IF baseband-equivalent frequency to capture the amplitude and phase information of the electric fields of the optical waves, based on [21]. The fundamental components in the framework are point couplers and phase shifters, from which more complex structures are composed. The phase shifter models the voltage dependence of index and attenuation based on the plasma-dispersion and PN junction equations discussed above.

For low frequencies, the linearity performance can be determined by numerically performing Taylor expansions about the operating point using the static ring model. Given a ring modulator design and technology parameters, and for a given laser offset relative to ring resonance and voltage bias, the optical transfer function of the ring is computed for a small voltage range about the bias voltage, Fig. 4.16. A Taylor series is performed, and the

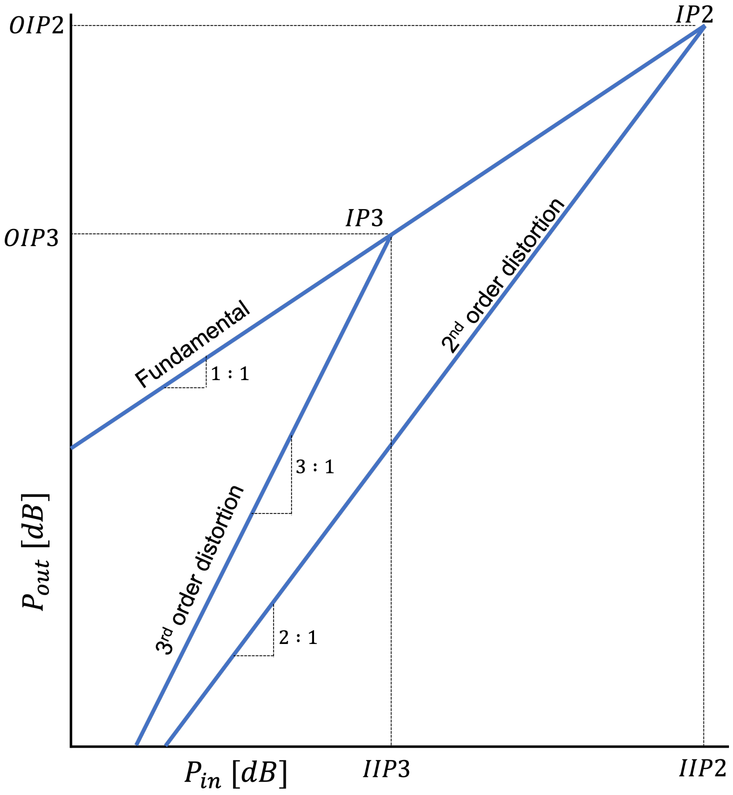

Figure 4.15: Output amplitude of fundamental tone, second order intermodulation tone, and third order intermodulation tone versus input amplitude. Intercept points are indicated. Note this is a log-scale plot.

intermodulation terms are calculated as [95]

$$IIP_2 = \frac{a_1}{a_2} \tag{4.53}$$

$$IIP_3 = \sqrt{\frac{4}{3}\left|\frac{a_1}{a_3}\right|} \tag{4.54}$$

where a_i represents the i^{th} term in the Taylor expansion. The modulation amplitude of 1 V in Fig. 4.16 is made purposely large to demonstrate the nonlinear modulation behavior.

To determine how laser offset with respect to ring resonance affects the linearity performance, the above procedure is repeated as the laser offset is swept, while keeping the bias voltage fixed. The power transmission, gain, and linearity behavior are shown in Fig. 4.17. In the top plot, the power transmission transfer function versus wavelength is plotted in red on the left axis. The ring resonance occurs in the center of the graph, at $\lambda = 1298.41\,\mathrm{nm}$

at the minimum of the transmission response. The gain is plotted in blue on the right axis. The gain is normalized to the peak gain value, as its exact magnitude depends on many parameters beyond those of the ring. It is interesting to note that the unlike the sensitivity (equivalent to gain) plotted in Fig. 4.13, the gain in Fig. 4.17 is not symmetric about the ring resonance. This is because the gain in this model is not simply calculated as the slope

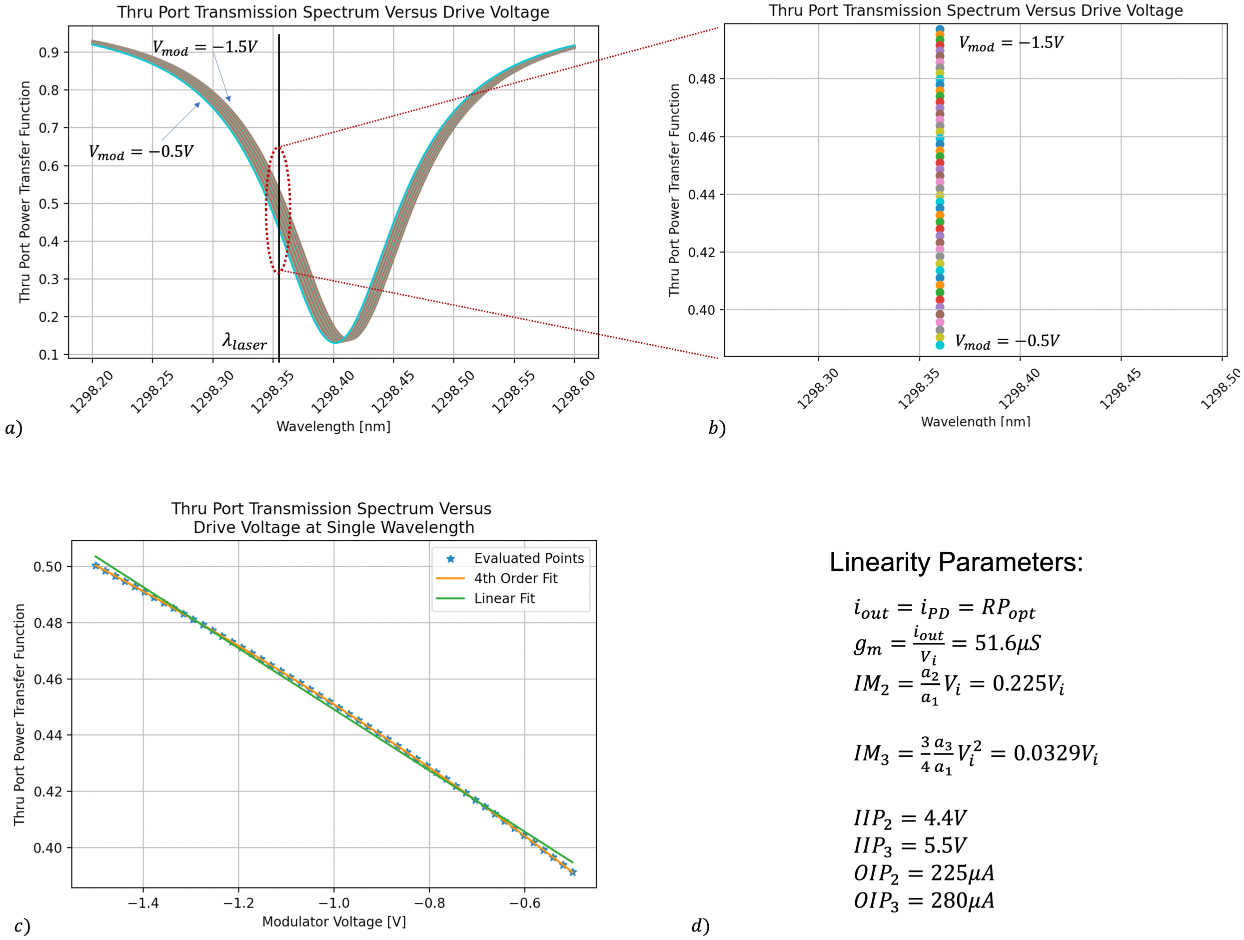

Figure 4.16: Sample calculation procedure for determining linearity metrics for a given wavelength and voltage bias point. a) Wavelength response of microring modulator for various voltages between $V_{mod} = -1.5\,\mathrm{V}$ and $V_{mod} = -0.5\,\mathrm{V}$. As b) Zoom in of thru power response. c) Plot of the thru power response versus input voltage, with linear and quartic fits. d) Calculation of linearity parameters. The ring model utilizes the nonlinear plasma dispersion model with an abrupt junction modulation. The FWHM bandwidth of the ring modulator is 22.6 GHz and the total quality factor is $Q = 10200$.

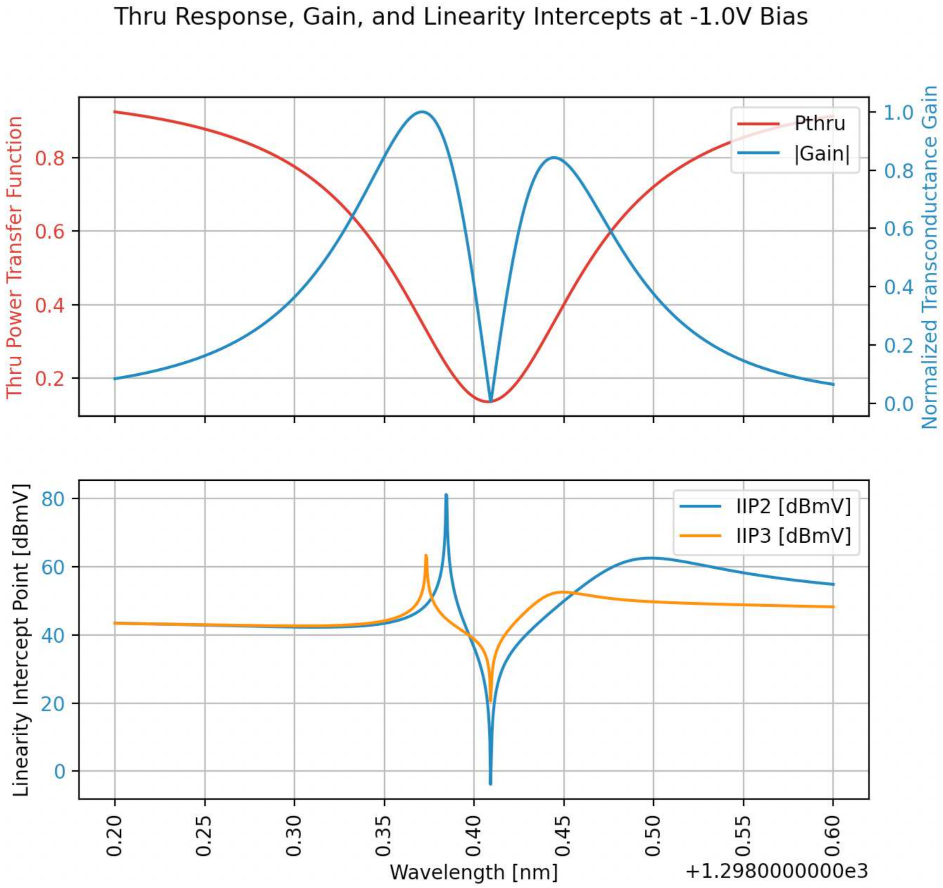

Figure 4.17: Power transmission response, transconductance gain, and IIP2 and IIP3 linearity intercept points for a microring modulator versus wavelength. (top) Thru port power transmission response (left) and normalized gain (right). The gain is normalized because its magnitude depends on other terms such as laser power and responsivity that are not parameters of the modulator ring. (bottom) IIP2 and IIP3 linearity intercept points. The ring model utilizes the nonlinear plasma dispersion model with an abrupt junction modulation. The FWHM bandwidth of the ring modulator is 22.6 GHz and the total quality factor is $Q = 10200$.

of the Lorentzian optical transfer function of the ring, but is rather calculated based on how the ring shifts due to the nonlinear index modulation due to the plasma dispersion effect.

The IIP2 and IIP3 linearity metrics are plotted on the bottom of Fig. 4.17 in units of dBmV. The linearity of the microring modulator depends strongly on the laser's offset wavelength relative to the ring resonance. Let us first consider the IM2 linearity. Far from resonance, the IIP2 is stable at roughly 44 dBmV. As the laser bias is brought closer to the ring resonance the IIP2 sharply spikes to 82 dBmV and then drops to very low values near resonance. As the laser is biased to the right of resonance, the IIP2 increases again, and settles to a higher value than on the left side of resonance. The IIP3 behaves similarly to the IIP2. Far from resonance, the IIP3 is nearly constant at 44 dBmV to the left of resonance and 48 dBmV to the right of resonance. The IIP3 also peaks sharply when the laser is biased at a slightly lower wavelength to the ring resonance. However, it should be noted that the laser offset that maximizes the IIP3 is not the same as the laser offset which maximizes IIP2. It should also be noted that the peak wavelengths for IIP2 and IIP3 linearity do not necessarily correspond to the wavelength that maximizes transconductance gain.

The linearity performance is now evaluated over both laser offset and bias voltage in Figure 4.18. The wavelength is plotted along the x-axis and the bias voltage along the y-axis. Thus, horizontal slices of each plot correspond to sweeps against wavelength at a constant bias voltage, similar to Fig. 4.17. The power transfer appears as expected: there is a notch as the wavelength approaches the resonance wavelength of the resonator. As reverse bias voltage increases (DC bias gets more negative), the resonance wavelength shifts to the right. In the second plot of Fig. 4.18, it can be seen that the gain of the microring modulator depends on both the laser offset and the bias voltage. The dependence on laser offset is expected, as the sensitivity analysis indicated in Fig. 4.13. The asymmetry of the gain about the resonance wavelength can again be observed in Fig. 4.18. Note also that the gain depends on the bias voltage, and that for larger reverse bias the peak gain is reduced. This is explained by the behavior of the abrupt junction diode: the depletion width shows a square root dependence on reverse bias voltage and the ring therefore shows a diminishing shift per volt at larger reverse biases.

The IIP2 and IIP3 linearity metrics are shown in the third and fourth plots of Fig. 4.18. First, note that at all bias voltages, there exists a 'sweet spot' for laser wavelength offset where the linearity peaks sharply. This sweet spot appears consistently at slightly lower wavelengths than the ring resonance. Precisely on ring resonance, the IIP2 and IIP3 fall sharply. This can be explained by the very small change in thru port power that occurs for a laser biased at the bottom of the Lorentzian. Note also that the IIP2 peak occurs at a roughly constant wavelength offset from resonance as the bias voltage is swept, while the IIP3 occurs at higher laser wavelength offsets from resonance as reverse voltage bias increases. This again highlights that the wavelengths at which gain, IIP2, and IIP3 peak are not the same, and can change with ring design and bias voltage. Finally, note that in addition to peaking when the laser is biased to the left of resonance, the IIP2 and IIP3 linearities peak on the right hand side of the resonance as well. While this right-side linearity peak may appear broader than the left-side peak, there are several reasons why the left-side peaks should be used. First, when the laser is biased at higher wavelengths than ring resonance, there is thermal instability due to the self heating of the ring resonator, which can lead to the ring snapping away from its nominal resonance position at even moderate optical powers [46]. Second, the wavelengths at which linearity peaks more closely align to the gain peak on the left side of the ring resonance. It is not expected that the linearity should be symmetric about the resonance; while the static Lorentzian is symmetric, the non-linear change in effective index and absorption that result from the plasma dispersion effect do not

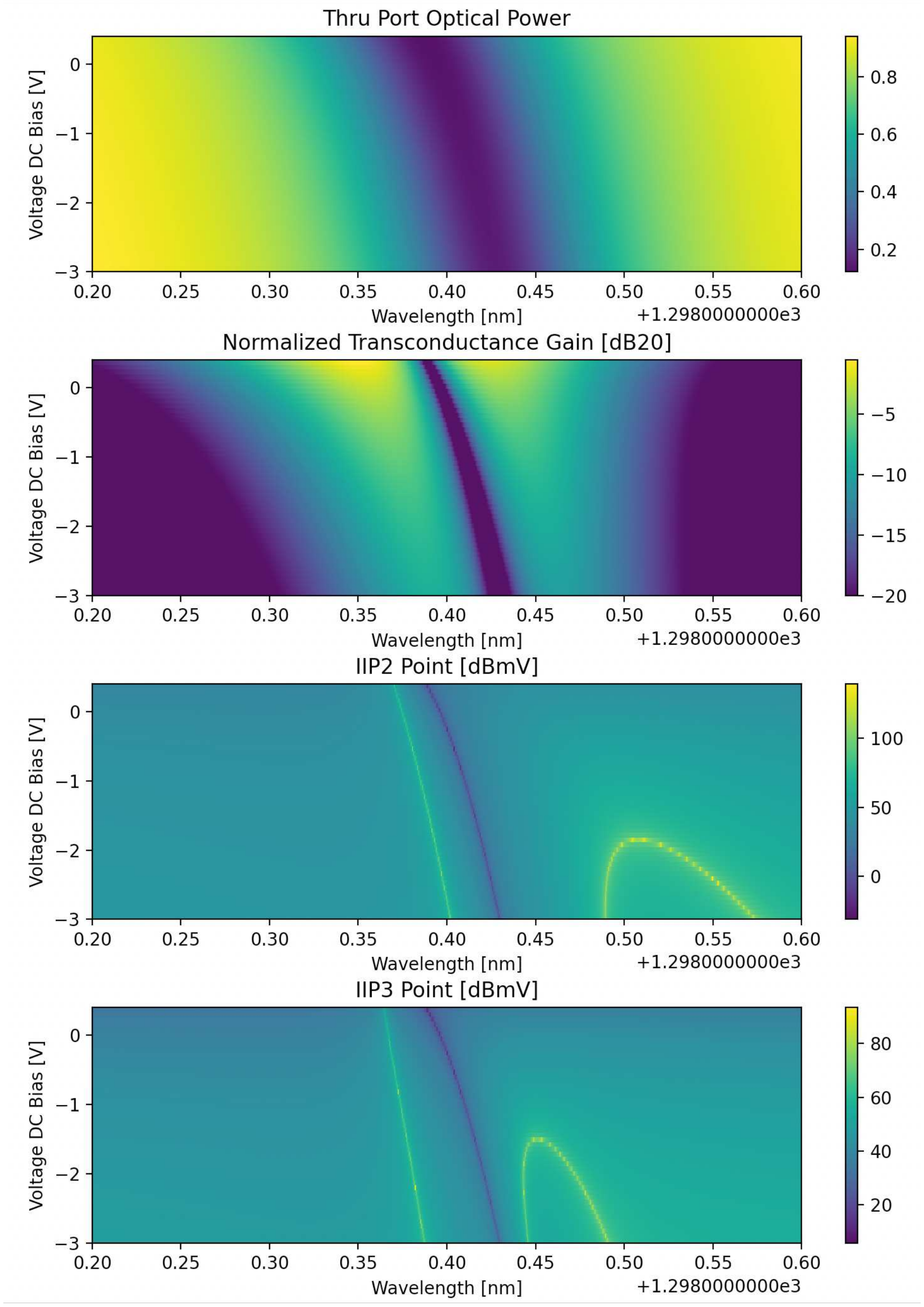

Figure 4.18: Power transmission response, transconductance gain, IIP2 linearity intercept, and IIP3 linearity intercept point (top to bottom) for a microring modulator versus laser offset wavelength and bias voltage. Linearity peaking is seen as the yellow lines in the third and fourth plots. The ring model utilizes the nonlinear plasma dispersion model with an abrupt junction modulation. The FWHM bandwidth of the ring modulator is 22.6 GHz and the total quality factor is $Q = 10200$.

inherently produce a symmetric function. This can be seen in Fig 4.16a, in which the lowest point of the Lorentzian continues to decrease as V_{mod} becomes more positive.

4.5.3 Noise in Microring Modulators

The noise figure of photonic links using microring modulators is now analyzed. From Eq. 4.21, noise figure depends on the transconductance gain of the link g_m, which in turn depends on the modulator's shift efficiency. The noise figure also depends on the optical loss in the link, which changes with modulator insertion loss as as the laser offset is swept relative to the resonance wavelength. The Simulink framework is again used to calculate the noise figure of a microring modulator as a function of voltage bias and wavelength offset, shown in Fig. 4.19. The upper figure shows the transconductance of the link, which peaks at an offset from the ring resonance. The middle plot shows the noise figure. Note that the noise figure shows a similar peaking (low noise figure is better) at an offset from the resonance. The bottom plot shows the transconductance and noise figure versus wavelength at a DC bias of $-0.5\,\mathrm{V}$. Note that the laser wavelength offset at which transconductance gain is maximized does not correspond exactly to the wavelength which minimizes noise figure. This is because both the insertion loss and transconductance vary as laser wavelength offset is changed, and noise figure (Eq. 4.22) contains terms that depend both on transconductance and on optical insertion loss.

4.5.4 Linearity of Microring Modulators in GlobalFoundries 45SPCLO

In order to validate the link models and analysis described above, the linearity and noise performance of a microring modulator were experimentally characterized. A microring modulator was implemented in GlobalFoundries 45nm CLO platform. Figure 4.20a shows a micrograph of the microring modulator. The microring modulator features lateral PN junctions, an embedded heater for wavelength tuning, and a drop port with monitor PD. The ring diameter is 7.7 um, corresponding to an FSR of 17.5 nm (Fig. 4.20b). Such a large FSR is desirable to enable many wavelength-division multiplexed (WDM) channels in a single fiber. The optical spectrum as a function of DC modulator voltage is plotted in Fig. 4.20c. As expected from the plasma dispersion effect, the DC voltage causes both a wavelength shift and absorption change which manifests as a changing quality factor. In the reverse bias region, the linear resonance shift per volt is extracted to be 4.5 GHz/V and the quality factor is $Q \approx 7500$.

Figure 4.20d shows the effect of increased laser power on the ring resonance. As the microring modulator absorbs a portion of the incident power, it experiences a self-heating effect. This self-heating causes the refractive index in the ring to change, which shifts the resonance wavelength. The self heating also distorts the Lorentzian line shape, as seen by the increasingly vertical right-of-resonance transmission spectrum for increased laser power in Fig. 4.20d, and can eventually lead to unstable DC bias conditions [46]. It should be

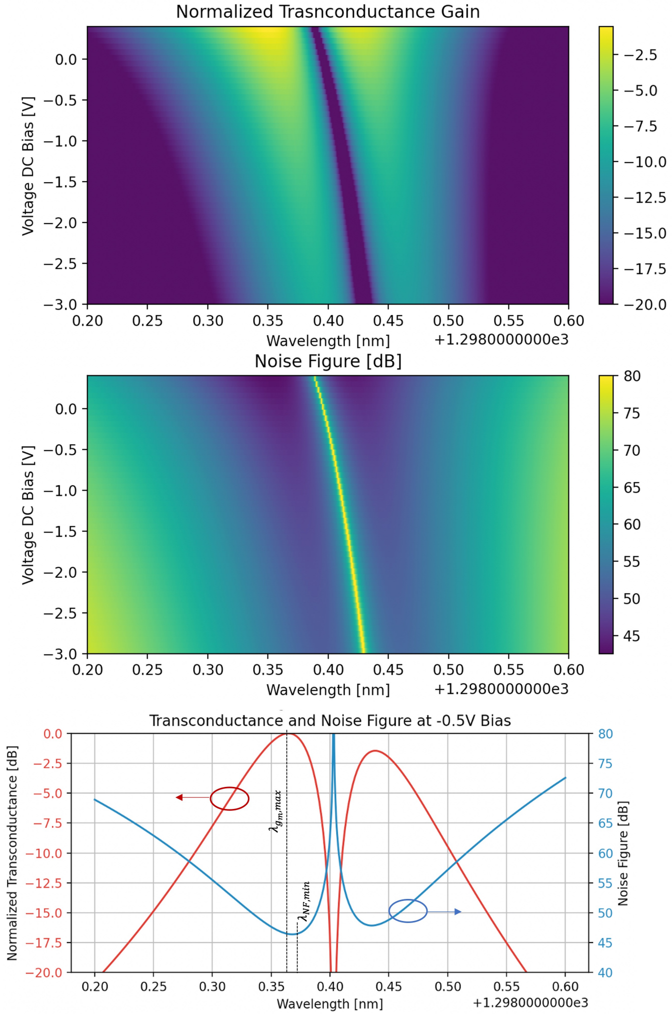

Figure 4.19: Normalized transconductance gain (top) and noise figure (middle) for a microring modulator versus laser offset wavelength and bias voltage. (bottom) Transconductance gain and noise figure versus wavelength at $-0.5\,\mathrm{V}$ bias. Note that the peak for transconductance does not correspond in wavelength to the peak in noise figure. The ring model utilizes the nonlinear plasma dispersion model with an abrupt junction modulation. The FWHM bandwidth of the ring modulator is 22.6 GHz and the total quality factor is $Q = 10200$. An ideal passive match is assumed at the input to the modulator. The laser power is 3 mW, optical link loss is assumed to be 6 dB, and responsivity is 1 A/W. The receiver noise current is assumed to be $2.8 \times 10^{-24}\ \mathrm{A}^2/\mathrm{Hz}$, equivalent to the noise of a TIA with $5\,\mathrm{k}\Omega$ resistive load.

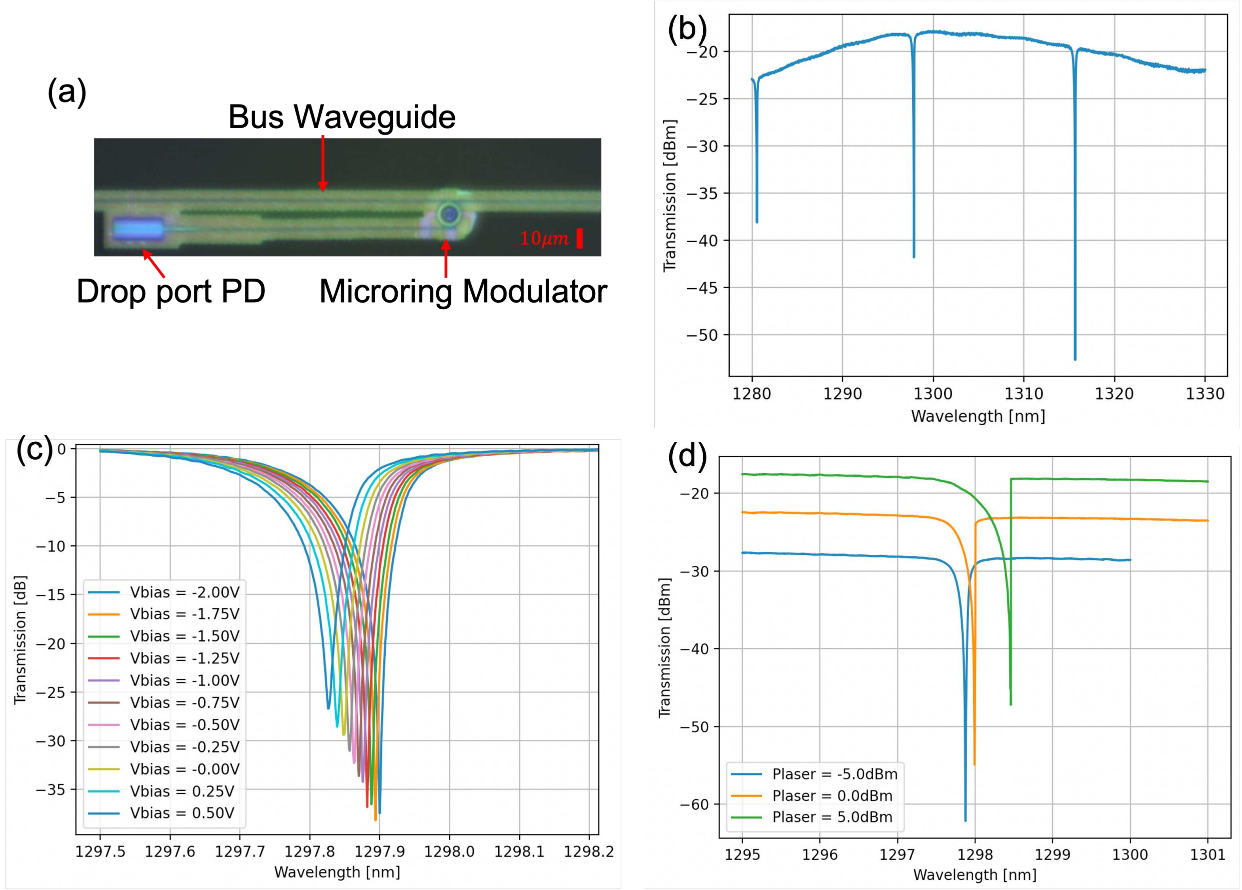

Figure 4.20: (a) Die micrograph after etching the substrate to expose photonic devices. (b) Measured wideband transmission spectrum at bias voltage $V_{bias} = 0\,\mathrm{V}$. (c) Measured DC transmission spectra at various applied voltages, normalized to peak transmission response. (d) Transmission spectra at various laser powers, showing the effects of self-heating.

noted that the distortion in Lorentzian line shape is only present for frequencies below the self-heating thermal bandwidth of the ring (usually on the order of 10's to 100's of MHz. For frequencies below this bandwidth, the distortion of the Lorentzian can impact the linearity of the microring modulator. Frequencies above the thermal bandwidth are not affected by this distortion.

The experimental setup used to characterize the linearity performance is shown in Fig. 4.21a. Two tones are combined and applied to the probed modulator site. Losses from the power combiner and bias-T are de-embedded from the measurements. A low-RIN tunable CW laser source (Santec-510, $-145\,\mathrm{dB/Hz}$ from $0.1 - 3\,\mathrm{GHz}$) is incident on the microring modulator. A low-noise amplified photodetector (ThorLabs PDB450C) is used to demodulate the opitcal signal into the electrical RF signal. The output of the photodetector is fed into a spectrum analyzer (Keysight N9010A). The input tones are centered around 1 MHz, to enable sufficiently high gain settings for the PDB450C photodetector. A split frequency of 2 kHz is used to minimize the sweep time of the spectrum analyzer.

The IIP3 intercept point is calculated versus laser offset wavelength relative to resonance and reverse bias voltage, Fig. 4.21b-d. The trend matches closely with the theoretical behavior predicted in Fig. 4.18. A peak in IIP3 is observed (yellow colors indicate higher IIP3) at wavelengths just below ring resonance. On resonance, the IIP3 linearity drops significantly (seen in blue), which is explained by the low optical modulation experienced at the relatively flat bottom of the Lorentzian. As optical power increases from −5 dBm in Fig. 4.21b to 5 dBm in Fig. 4.21d, the wavelength range over which the modulation remains linear increases. This matches well with the self-heating effect seen in Fig. 4.20d, with the left side of the resonance expanding. In Fig. 4.21d the IIP3 is very low for wavelengths to the right of resonance because the self-heating effect causes the ring resonance wavelength to rapidly shift away from the laser wavelength once the laser wavelength is greater than the resonance wavelength; this causes the laser to be biased far from resonance, which results in very low optical modulation (and thus very low a_1 in Eq. 4.52). Finally, the IIP3 at $V_{bias} = -0.5\,\mathrm{V}$ for all three optical power levels is plotted versus offset wavelength from resonance in Fig. 4.21e.

In addition to characterizing the IIP3 linearity of the modulator, the spur-free dynamic range is characterized. Third order spur-free dynamic range (SFDR) is a measure of the linearity of a modulator, defined as the ratio of the maximum input power before which the third order intermodulation tone crosses the minimum detectable signal, to the minimum input power that results in a detectable signal above the noise floor. It thus gives a measure of the maximum possible IM3 linearity achievable in a system with noise, Fig. 4.22. SFDR is expressed as

$$\mathrm{SFDR3} = \frac{2}{3}\left(\mathrm{IIP3} - \mathrm{MDS}_{in}\right) \tag{4.55}$$

MDS_{in} is the input referred minimum detectable signal. From Eq. 4.18, the total output noise is $g_i n_i + n_a = g_i n_i 10^{NF/10}$, or in dB: $MDS_{out,dB} = 10\log(g_i) + 10\log(n_i) + NF$, which implies

$$\mathrm{MDS}_{in} = 10\log(k_B T) + \mathrm{NF} \tag{4.56}$$

where NF (in dB) is the noise figure of the link.

The SFDR is characterized versus the voltage bias point and laser bias point (offset from ring resonance position), as shown in Fig. 4.23a-c. As part of the SFDR characterization, the minimum detectable signal must be calculated. This was done by measuring the noise floor at the output of link at the spectrum analyzer under matched input load with no signal applied. In this case, the noise floor includes the noise from the PDB450C's internal circuitry (reported noise equivalent power of $NEP = 1.55\mathrm{pA}/\sqrt{\mathrm{Hz}}$). However, this is analogous to how noise calculations are performed when designing an optical receiver in a monolithic process, where the TIA can be closely integrated with the photodetector, and thus the modulator and receiver are co-designed as a single link. Furthermore, this method avoids

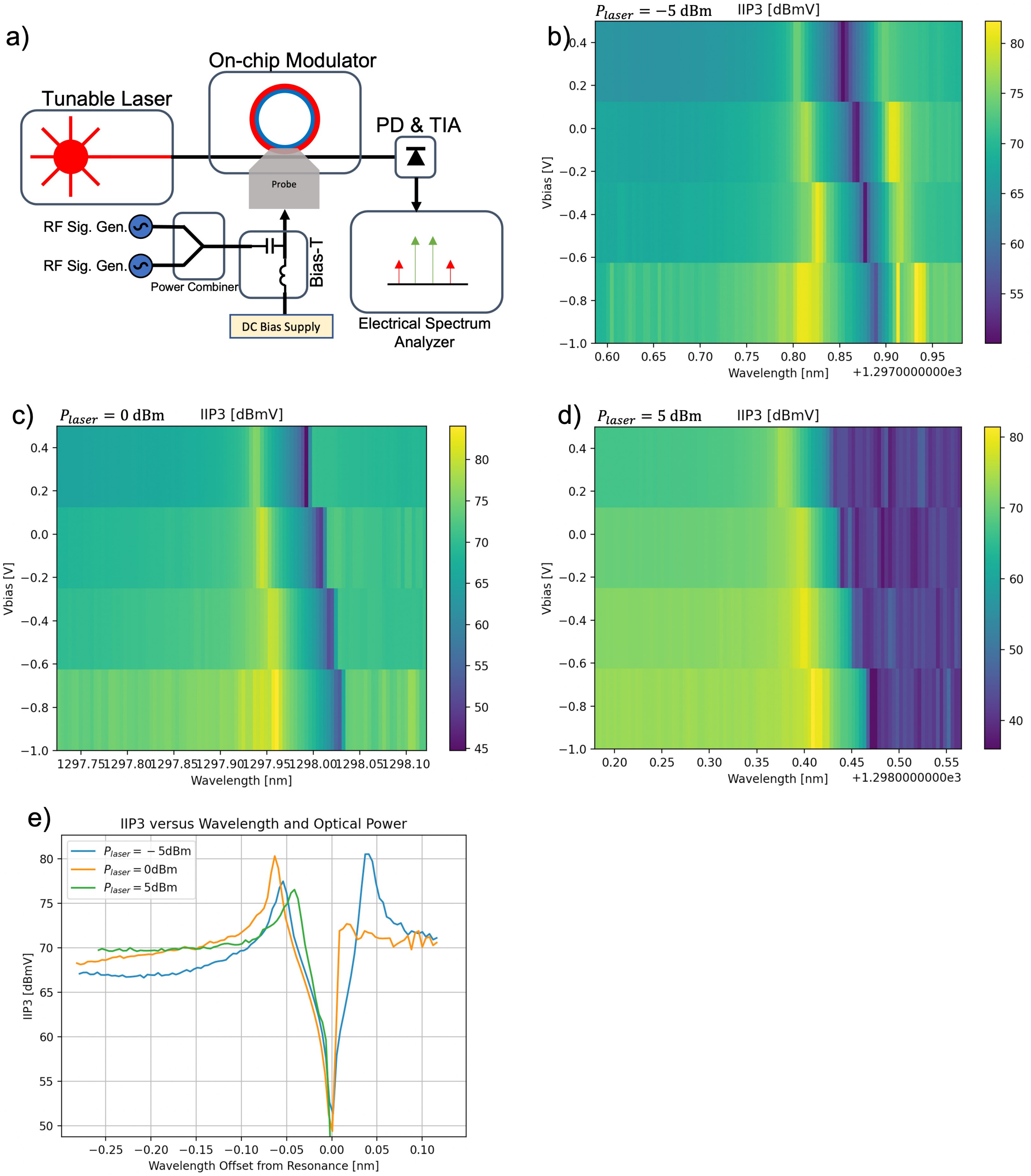

Figure 4.21: (a) Two tone linearity measurement setup. (b-d) IIP3 intercept point [dBmV] for −5 dBm, 0 dBm, and 5 dBm laser power. Ring resonance occurs at the dip in IIP3, seen in blue. e) IIP3 [dBmV] versus wavelength offset from resonance for all three power levels at $V_{bias} = -0.5\,\text{V}$.

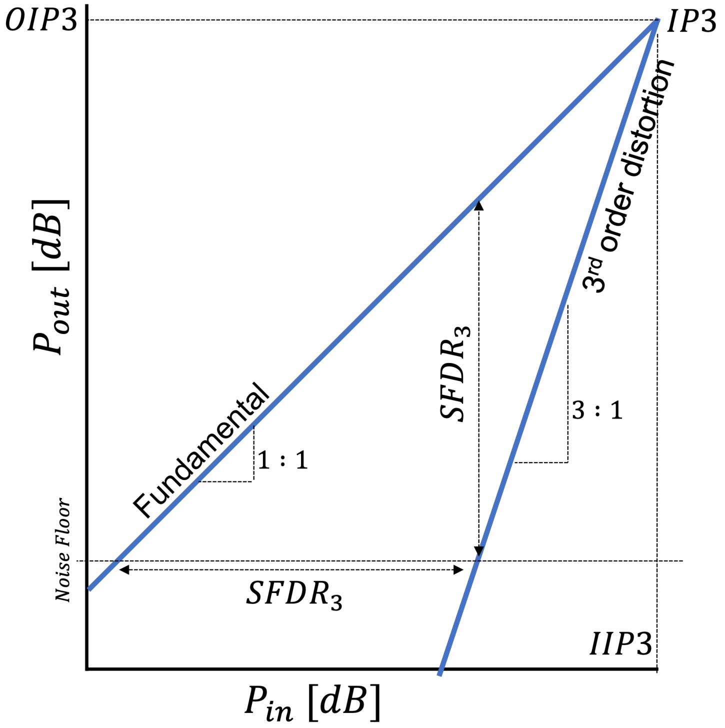

Figure 4.22: Output fundamental and third order power versus input power. The noise floor, independent of input power, plotted as a horizontal line. SFDR3 represents the maximum dynamic range achievable, bounded by the noise floor on the low end, and the power at which the third order intermodulation spur rises above the noise floor on the high end.

making assumptions about the dominant noise source, which can change when the optical power incident on the photodetector decreases near resonance.

Figure 4.23a shows the SFDR for low input laser power ($P_{laser} = -5\,\text{dBm}$). The SFDR shows a roughly symmetric response around the ring resonance (the dark central region), which shifts as the voltage bias point is varied. The peak SFDR is $SFDR_{peak,-5dBm} = 91.8\text{dB} \cdot \text{Hz}^{\frac{2}{3}}$. The SFDR remains within 3dB of its peak value across roughly 30 pm of optical bias, which covers 5.5 GHz of shift range, or roughly 1 V of peak-peak input swing.

Figure 4.23b shows the SFDR for moderate input laser power ($P_{laser} = 0\,\text{dBm}$), with $SFDR_{peak,0dBm} = 96.4\text{dB}\cdot\text{Hz}^{\frac{2}{3}}$. Here, the SFDR is no longer symmetric about the resonance, which is due to the distortion of the Lorentzian line shape caused by self heating.

Finally, Fig. 4.23c shows the SFDR characterization for relatively high input laser power ($P_{laser} = 5\,\text{dBm}$, with $SFDR_{peak,5dBm} = 97.5\text{dB} \cdot \text{Hz}^{\frac{2}{3}}$. For high laser power, the region over which SFDR remains high extends more broadly to the left of the ring resonance. However, to the right of right resonance, little modulation is observed. Both these effects are due to

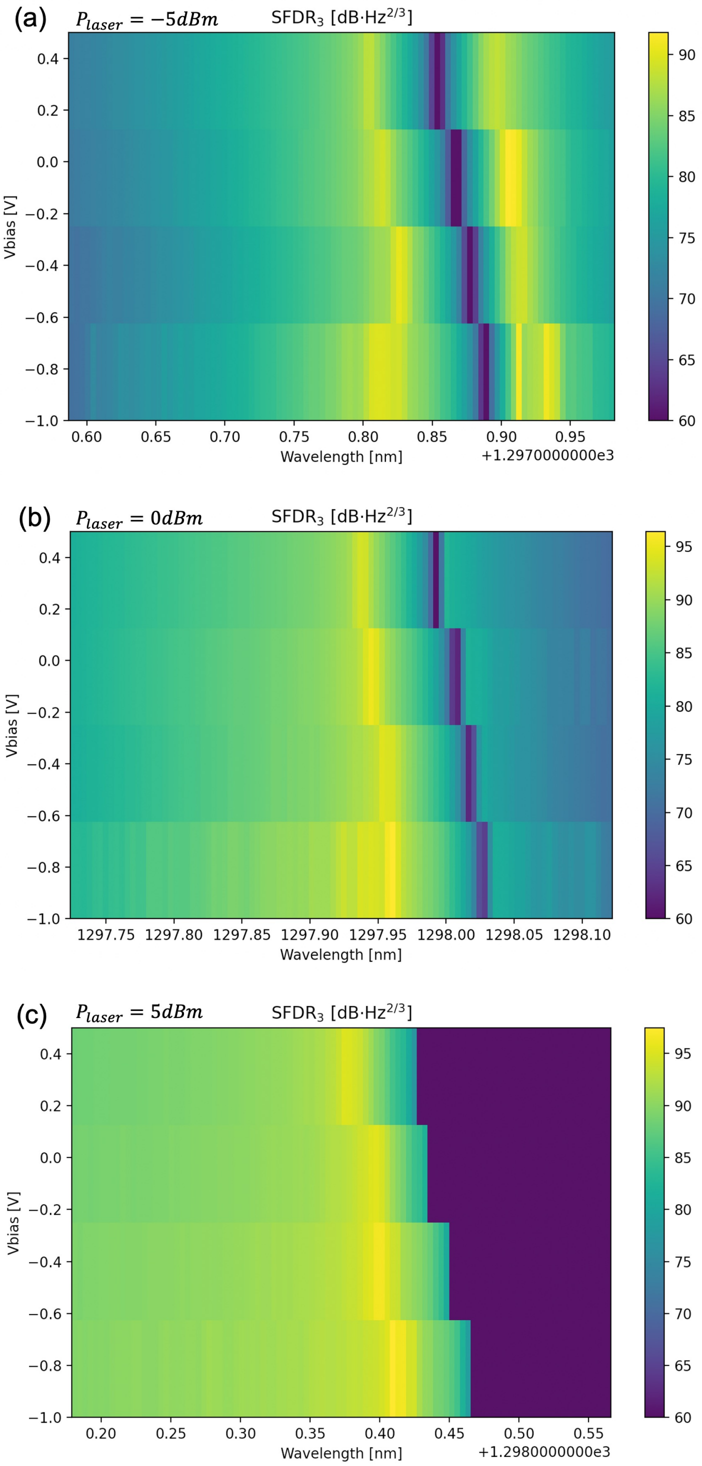

Figure 4.23: (a) SFDR$_3$ versus electrical and optical bias points, for $P_{laser} = -5\,\mathrm{dBm}$. (b) SFDR$_3$ versus electrical and optical bias points, for $P_{laser} = 0\,\mathrm{dBm}$. (c) SFDR$_3$ versus electrical and optical bias points, for $P_{laser} = 5\,\mathrm{dBm}$.

the unstable behavior of microring resonators under sufficiently high self-heating conditions [46].

These results show consistent behavior with the analysis from the Simulink simulation. Such results not only validate the Simulink modeling framework for use in analog link applications, but also demonstrate that microring modulators can be used to achieve competitive third-order SFDR performance. This ring implemented in the GF45SPCLO platform achieves similar linearity performance compared with prior work, at significantly significantly higher FSR or lower laser power [96, 97].

4.6 Conclusion

This chapter provides an analysis of optical links for analog modulation. The gain and noise performance of analog optical links were derived. Using the developed model, the design space for link noise figure can be explored across various technology parameters and optical design parameters, such as optical power. A motivating example of the potential benefits of analog optical links over conventional digital links for 5G applications showed that analog links offer the potential for substantial power saving at equivalent link performance.

Next, the optimal laser bias and optical design parameters were derived to achieve maximum modulation efficiency. The linearity performance of microring modulators for analog links was explored using a Simulink modeling framework. Measurements of the IM3 and SFDR3 metrics on a microring modulator implemented in GlobalFoundries 45nm CLO platform suggest that microrings, combined with performant RF transistors on the same chip, can be used for optical I/O scaling in fully-integrated WDM links for future 5G applications and beyond.

Chapter 5

Analog Optical Link for MRI

As discussed in Chapters 3 and 4, multi-channel analog optical links have the potential to enable I/O scaling in novel applications. In this chapter, a proof of concept WDM analog optical link using microring modulators is proposed for data remoting in Magnetic Resonance Imaging (MRI) systems. Section 5.1 begins with an overview of the system. A link model is introduced in Section 5.3 using the analog link modeling framework developed in the preceding chapter. Sections 5.4-5.6 provide chip implementation details. The packaging work needed for monolithic photonic SoC's in the GlobalFoundries 45nm RFSOI platform is discussed in Section 5.7. Finally, the chapter concludes with measurement results and discussion.

5.1 Introduction

Magnetic Resonance Imaging is a critical tool in medical diagnostics. In a MRI system, a strong static magnetic field (on the order of 1 to 10 Tesla) causes a split in the spin states of the proton in hydrogen nuclei. An RF electromagnetic pulse is applied to excite transitions between the two energy states. Gradient coils apply magnetic fields on the order of mT such that the transition energy between the spin states matches the energy in the excitation wave at only a specific location in the body, enabling localized imaging. Finally, small sensor coils pick up the RF electromagnetic waves that get emitted as the spin states decay back to the low energy state. The signals picked up by these sensor coils feed into receiver circuits, and are eventually processed to form the MRI image.

One of the main drawbacks to MRI is the long scan times required to scan through the volume of space to be imaged. To enable faster scan times and higher signal to noise ratio, parallel imaging can be performed, in which multiple coils simultaneously sense a localized region [98]. Commercial scanners have capability of 16, 32, and even 64 channels [99], and even higher channel counts are being considered in research [98]. One of the key challenges to achieving even higher channel count is the practical issue of added weight and bulk as the number of channels increases [100]. Special care must be taken to properly shield the coaxial

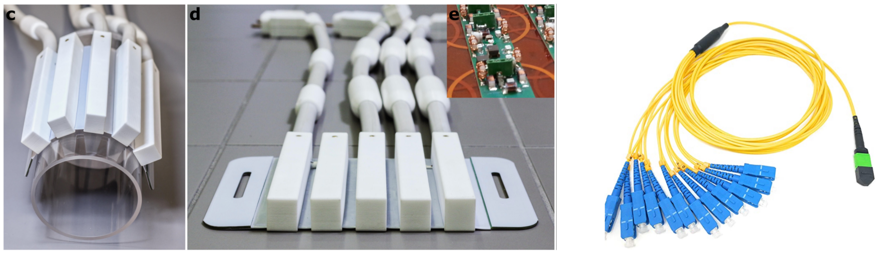

(a)

(b)

Figure 5.1: (a) Sample of a 23-channel MRI coil array. Note the bulky electronics (top right) and the thick coaxial cables required to bring the signal out of the magnetic environment. From [106]. (b) A 12-fiber fiber-optic cable. The main cable has 12 fibers in a single jacket. In this figure, the 12 fibers are individually broken out to show all the connections. The cable diameter is 2 mm including the protective jacket.

cables from the magnetic environment and to properly isolate the channels from each other to prevent interference and potential damage due to RF heating [101]. This results in bulky cabling, as shown in Figure 5.1(a).

One solution to the physical cabling challenge is to utilize fiber optic cables to remote the MRI data out of the magnetic environment. Fiber optic cables are significantly smaller, more lightweight, and potentially more flexible than coaxial cables, see Fig. 5.1(b). In addition, once the signal is in an optical cable, it is no longer susceptible to the interference from the strong magnetic field switching [102].

Prior work has been done to utilize optical links within an MRI environment. A 16-channel in-bore receiver is presented in [103], which uses discrete ADCs, ICs, and optical modules. This solution achieves 88 dBc SFDR and 1.56 dB NF in a 3T MRI environment, but its large form factor makes this solution challenging to incorporate into flexible and high-coil count arrays. In [102], a 2 channel on-coil receiver was demonstrated, which features a low noise receiver and ADC on chip, and drives an external optical module. One challenge with these digital optical links is that careful synchronization is required when quantizing the receive signal, which requires careful design and additional clock references to be passed into the bore. An analog optical link was demonstrated in [104], which featured an on-coil discrete preamplifier driving a discrete directly modulated laser diode located outside the main magnet. Finally, [105] utilizes a delta sigma modulator frontend and high oversampling rate to achieve above 80 dB dynamic range using off-the-shelf components.

5.2 System Summary

In this work, a 8-channel, on-coil, fully integrated MRI receiver is proposed. Microring modulators are used as the electro-optic modulator to demonstrate the capability of channel

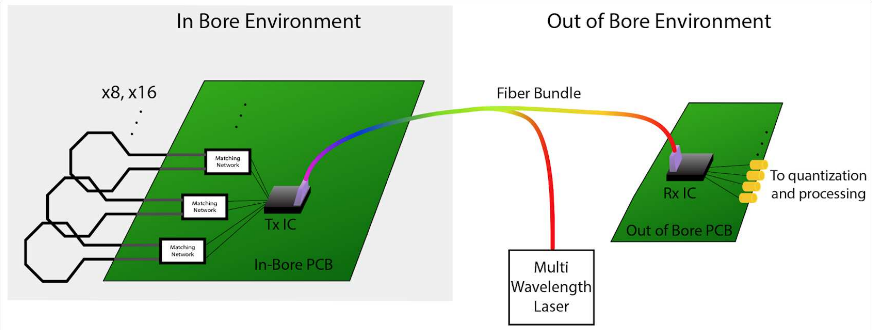

Figure 5.2: System architecture overview. A small printed circuit board sits in-bore and hosts an 8-channel transceiver chip. Off-chip matching elements interface with MRI coils. A fiber bundle remotes the data to an out-of-bore receiver IC. The light is provided through an out-of-bore multi-wavelength laser source.

densification enabled by WDM optical links and to demonstrate the feasibility of microrings for analog optical link applications. The system targets a 1.5 T MRI system, which corresponds to an RF excitation frequency of 64 MHz. The input SNR is assumed to be 55 dB from the MRI coil (prior optical links for MRI data remoting achieved 27 dB image-SNR [104] and 47 dB peak link-SNR [105]). The design goal of the electro-optic link is to remote the received signal from the MRI environment with minimal SNR and linearity degradation. Design objectives were therefore set to provide sub 3 dB SNR degradation and above 50 dB IM3 linearity across the link to maintain a noise-dominated SNDR above 50 dB.

The link developed in this work serves to remote data from MRI receiver coils inside the MRI bore to a receiver outside of the magnetic environment, Fig. 5.2. Inside the magnetic environment, multiple RF sense coils are interfaced to the link transceiver IC through on-board matching networks. Each channel gets amplified through a linear low-noise amplifier chain to drive a microring modulator, which brings the signal into the optical domain. The microring modulator of each channel is tuned to a slightly different resonance wavelength, to enable WDM channel densification by transmitting all 8 channels on the same fiber. A fiber moves the data from the MRI environment to a receiver IC that sits outside of the magnetic environment. Because of the low losses in optical fiber, this receiver IC can sit even hundreds of meters away from the MRI machine. The receiver IC features a WDM microring filter array to demultiplex each channel. Each channel passes through a linear receiver circuit which drives the analog waveform to pads, to be post-processed off-chip.

5.3 Link Model

The link model described in Chapter 4 is used to evaluate the performance of microring modulators in the context of MRI signaling. The doping and junction parameters used in the

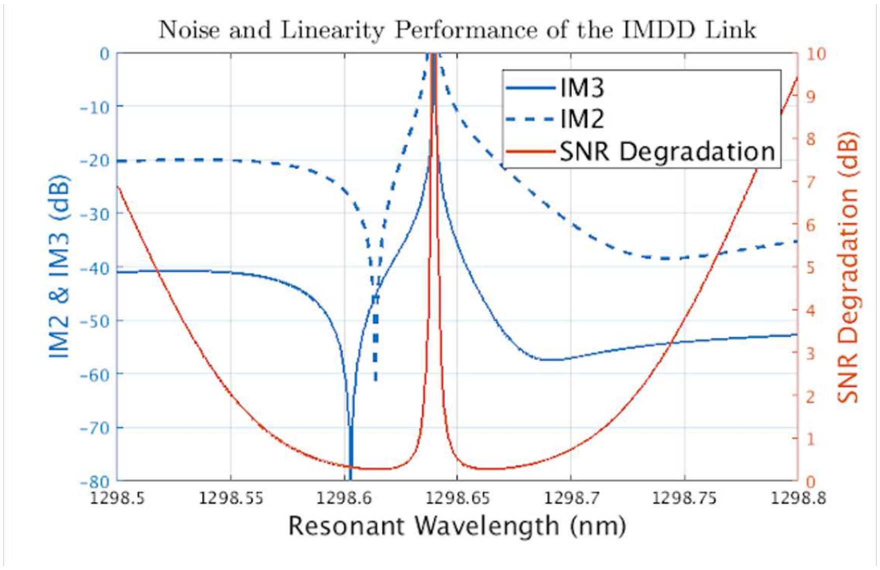

Figure 5.3: Noise and linearity performance of IMDD MRI link. Input SNR of 55 dB is assumed. An input swing of $v_{amp} = 0.4\,\mathrm{V}$ is applied to the ring modulator (corresponding to an amplifier gain of roughly 40 dB). The total ring Q is roughly 10000. Laser power is 2 mW, responsivity is 0.5 A/W, and 6 dB link loss is assumed.

model lead to an effective resonance shift per volt of 3 GHz/V which agrees with previously characterized devices in the GlobalFoundries 45nm RFSOI platform. It is assumed that a linear electrical amplifier can modulate the microring modulator with a swing of $v_{amp} = 0.4\,\mathrm{V}$, which corresponds to an amplifier gain of roughly 40 dB for peak input signal amplitude. A laser power of $P_{laser} = 2\,\mathrm{mW}$ is assumed, as well as 6 dB of total optical loss along the link. The responsivity of the photodetector is assumed to be $R = 0.5\,\mathrm{A/W}$, which has previously achieved in this platform [71].

Figure 5.3 shows the linearity and noise performance achieved by a microring modulator link under the above assumptions. The IM3 linearity at 0.4 V drive amplitude is better than 50 dB for a range of $> 20\,\mathrm{pm}$, which corresponds to over 1 V of modulator range over which the linearity is preserved. In addition, the SNR degradation is below 1 dB for a wide range of offset wavelengths relative to ring resonance. These results suggest that microring modulators can be designed in the 45nm RFSOI platform to achieve the desired performance metrics for the MRI link.

5.4 Circuit Design

5.4.1 Transmitter Design

In order to achieve an optical-link SNR degradation of $< 1\,\mathrm{dB}$ as shown in Fig. 5.3, a low-noise preamplifier must be used to amplify the signal from the MRI coil to suitable drive levels for the microring modulator. This preamplifier serves as both the receiver circuit for the signal from the MRI coil, as well as the transmitter driving the microring in the optical link. The input power from an MRI coil depends on many factors, including the positioning of the coil, the protocol of the MRI scan being used, and the thickness of the sample. For the design of this system, it is assumed that the input power is in the range of $-80\,\mathrm{dBm}$ to $-40\,\mathrm{dBm}$ [102], which is equivalent to $31\mu V$ to $3.1\,\mathrm{mV}$ on a $50\,\Omega$ load. Thus, the transmitter requires a gain of between 40 dB and 80 dB to achieve the 0.4 V swing on the microring modulator.

The architecture of the coil-receiver / transmit ring driver circuit is shown in Fig. 5.4a). The circuit is broken into several stages, each with various constraints. Because of the high gain requirements, the stages are ac-coupled to reduce large offset errors and ease offset calibration. In addition, all stages except the final ring driver are differential, to provide good power supply rejection and superior IM2 linearity. The first stage circuit details are shown in Fig. 5.4b). This stage uses a current-reuse amplifier to increase the effective transconductance. A feedback resistor sets the first stage gain, and can be digitally controlled via an RDAC. The next stage comprises a mixer, which is bypassed during standard operation. Its role is to enable potentially higher frequency input signals beyond the bandwidth of the subsequent stages. The second stage amplifier is a Cherry-Hooper architecture (Fig. 5.4c), and is designed to provide additional signal gain. The third and fourth stages are variable gain amplifiers, and utilize a standard folded cascode topology. Each stage is designed to produce a gain between 0 dB and 17 dB in roughly 1.5 dB steps. All preceding stages are supplied from a 1.2 V analog supply. The final stage is the output driver which modulates the microring. This stage provides differential to single ended conversion, and is supplied from a high voltage supply (1.8 V) to increase the output swing range. A common mode feedback loop is used to set the output voltage to $V_{out,cath}$, which is a bias provided from off-chip. This bias is necessary to set the DC cathode voltage on the microring modulator.

The overall amplifier chain is simulated to have a bandwidth from $1\,\mathrm{MHz} - 114\,\mathrm{MHz}$. The minimum gain is 50 dB and has over $40dB$ gain tuning. The 50 dB IM3 linearity occurs at an output voltage swing of $v_{amp} = 0.26\,\mathrm{V}$. While this is slightly lower than the design target, the impact on the SNR degradation due to the optical link is negligible. The noise figure of the end-to-end link is simulated to be below 1 dB.

5.4.2 Receiver Design

The receiver serves to recover the analog electrical signal from the photocurrent generated by a photodetector. The receiver architecture is shown in Fig. 5.5. A pseudodifferential

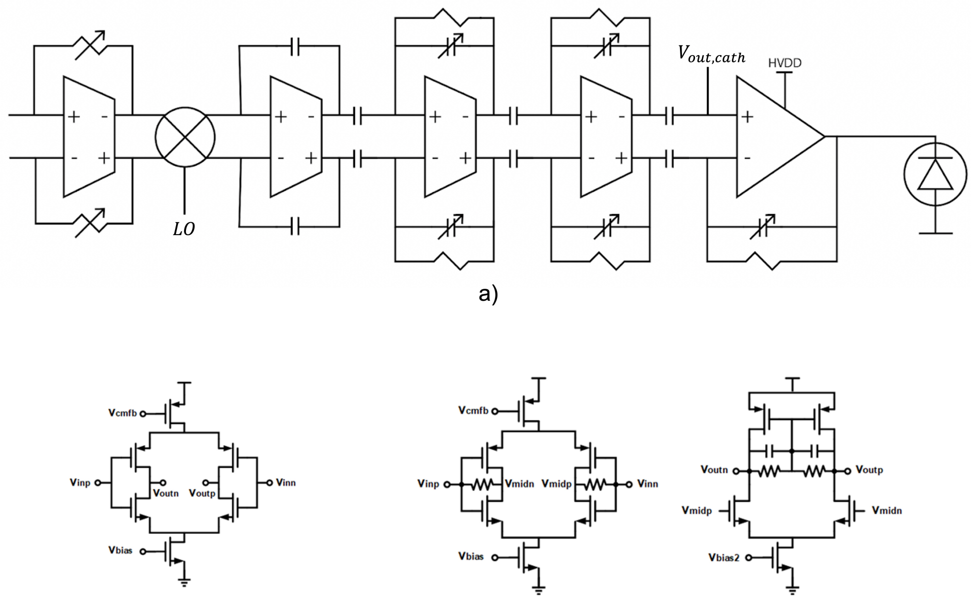

a)

b)

c)

Figure 5.4: Architecture of the MRI receiver / transmit driver for the microring modulator. a) Architecture of the gain chain, including 1st stage, bypass-able mixer, 2nd gain stage, two VGA stages, and output driver stage. b) Circuit details for 1st stage amplifier. c) Circuit details for 2nd stage amplifier.

transimpedance amplifier (TIA) is used to amplify the received photocurrent. A CML driver buffers the output of the TIA and drives pads to bring the signal off-chip for analysis and post-processing.

The TIA features a 10-bit current bleeder DAC on the photocurrent input node to cancel the DC photocurrent received from the photodetector. The dummy TIA has two current DACs operating in push and pull configuration to provide offset correction. A 9-bit SAR ADC, generated in BAG [107], quantizes the recovered voltage. The output of the SAR goes into the digital backend that provides a thermal tuning loop to keep the ring resonance locked to the laser.

The feedback resistance of the TIA was chosen to balance the linearity and noise performance of the receiver. A larger resistance results in better input-referred current noise, but results in a larger output swing which could limit the linearity of the receiver. From the link model in Section 5.3, the peak signal photocurrent has an amplitude of roughly $28\,\mu$A. However, this value can easily change if the losses in the link vary from the expected values, or if laser power is changed. The resistor was therefore designed as a resistor DAC configurable between $100\,\Omega$ and $1\,\mathrm{k}\Omega$. At $R_{fb} = 100\,\Omega$, the IM3 at $28\,\mu$A input current is 90 dB (IIP3 of $300\,\mu$A) and spot noise is $\approx 1 \times 10^{-18}$ V^2/Hz.

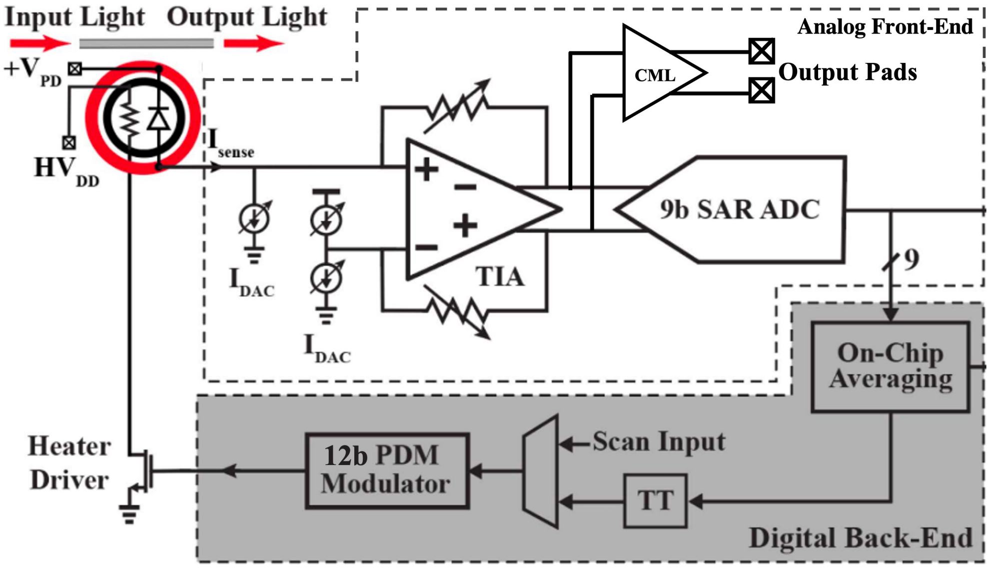

Figure 5.5: Receiver architecture. A pseudodifferential TIA receives the photocurrent. CML drivers drive analog pad outputs. A SAR ADC quantizes the signal, which feeds into the digital backend for thermal tuning. From [6].

5.5 Optical Design

Berkeley Photonics Generator (BPG) was used to implement the optical portions of the design. The hierarchy of the photonic layout can be broken down into several categories: microring modulators and filters, WDM ring rows, and top level routing.

The microring modulators were designed using spoked interleaved junctions, Fig. 5.6a. The microring is doped with alternating P and N regions to form depletion regions inside the ring. A highly doped silicon resistive heater is placed in the center of the ring, and is used to tune the resonance wavelength through silicon's thermo-optic coefficient. In these designs, several of the PN junctions in the microring are re-wired to serve as an embedded photodetector which is used to track the optical power in the ring for thermal tuning. Special attention must be given to the arrangement of dopants and wiring for this embedded PD to ensure that the parasitic diode that forms between adjacent contacts does not affect the power monitor circuits, Fig. 5.6b. The rings in this work are doped such that the parasitic diode forms between the DC anode and cathode bias nets. The modulator rings are designed to be critically coupled near $\lambda = 1290\,\text{nm}$ to achieve the highest modulator efficiency. The quality factor of these modulators is expected to be near 10000.

The photodetectors in this work are implemented as microring resonator based detectors. A silicon-germanium layer is grown in a partially etched trench around the optical mode-field center of the ring, which enhances the carrier generation [71]. Such resonant photodetectors

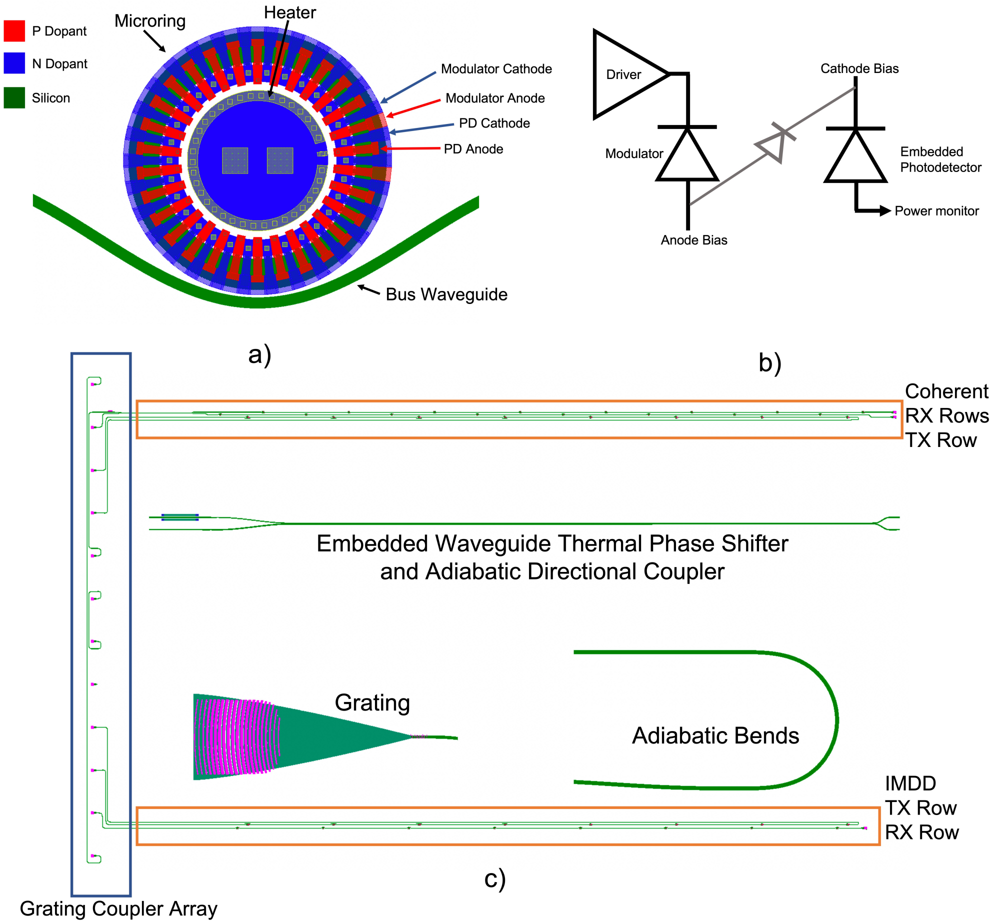

Figure 5.6: a) Microring modulator layout. Spoked junction design is shown, comprising alternating P and N doped regions to form depletion regions within the ring. Note the special doping patterns on the right side of the ring around the embedded photodetector spokes. b) Equivalent electrical model of the microring junctions. c) Top level photonic system. The grating coupler array is on the left, with fixed grating pitch and loopback structures for alignment. Also called out are the grating shape, adiabatic bends used throughout the layout, and an adiabatic directional coupler used for the coherent link architecture.

have been shown to significantly boost responsivity in the GlobalFoundries 45nm RFSOI platform as compared with linear photodetectors, due to the lack of pure germanium in the process.

Multiple microring resonators are cascaded into a single WDM row. The BPG class used for this ring-row was configured to allow for independent ring parameters for each ring. The row-generator was designed in close synchronization with the top level integration, to determine proper ring pitch and routing clearance constraints. All waveguide routing turns were implemented using the semi-automated `WgRouter` BPG utility, and featured adiabatic Euler-circular-Euler bends to avoid mode overlap losses at the terminals of the bend.

Finally, a top-level generator class was developed to integrate all photonic elements on the chip, Fig 5.6c. The generator includes a grating coupler array with loopback structures at the outermost gratings to help alignment during fiber attach and to deembed grating and waveguide loss. The gratings are designed to be unidirectional and couple through the back side of the chip (ie, face up after flip chip packaging). The chip features two 8-channel WDM links. The first link is a 8-channel IMDD link comprising a TX ring row and RX ring row. The second is a 8-channel coherent link comprising a TX ring row and a RX row with embedded thermal phase shifter and adiabatic directional coupler for achieving a laser forwarded coherent link [108].

5.6 Digital System

Both the transmit and receive microring modulators and filters require precise tuning controllers to adjust the ring resonance wavelength. Such control is required to compensate for process and temperature variation, as the precise resonance wavelength can vary over the full FSR. As discussed in Chapter 4, the transmit microring resonance wavelength must be aligned at a specific offset with respect to the fixed input laser wavelength in order to achieve peak modulation amplitude, peak linearity, or peak noise figure. In contrast, the receive microring resonance should ideally be placed exactly aligned with the laser wavelength, such that maximum power circulates within the microring, and maximum photocurrent is generated.

As indicated in Eq. 3.24, as the resonance wavelength of the microring becomes aligned with the laser wavelength, the ring experiences a power buildup such that the power circulating within the ring is enhanced. Off of resonance, the buildup factor is lower, and less power circulates within the ring. Thus, sensing the optical power circulating within the microring provides a proxy for alignment of the ring with respect to the laser wavelength. For transmit microrings, the embedded photodetector described in Fig. 5.6 is used to directly sense the power in the ring. An integrating frontend and voltage controlled oscillator based ADC then quantize the sensed photocurrent to produce a digital value. For the receiver microring, the signal photocurrent can directly be used to monitor the power in the ring. A SAR ADC shown in Fig. 5.5 quantizes the signal photocurrent, which is averaged to produce a low-frequency reading of the power circulating in the microring.

A thermal tuning controller uses a finite state machine (FSM) to adjust the resonance wavelength of the ring. The input is the digital reading of the power circulating in the ring. The output of the thermal tuner is a 12-bit heater control signal which feeds into a pulse density modulator (PDM), which in turn drives a heater driver that adjusts the temperature of the ring, as shown in Fig. 5.5.

Though the transmit and receive rings track different points, the FSMs that controls the two thermal tuning loops are very similar. Both operate by progressing through the following states:

- **State Scan:** In the scan state, the controller ramps the heat code up from a user-configured start heat to a user-configured stop heat. During this scan, the controller for the receiver microring keeps track of the maximum power observed circulating within the microring. For the transmit ring, the controller keeps track of the maximum delta in observed power between two consecutive heat steps; this delta in power is used to track the slope of the Lorentzian shape.

- **State Return:** After the scan is complete, the heater returns to a user-configured heat code, to position the ring's resonance on the right or left side of the laser wavelength, as desired.

- **State Find:** The heat code is changed to the code which maximized the power in the ring (receiver) or modulation slope (transmitter).

- **State Lock:** The current power in the ring is compared to the power which maximized the metric of interest. If the current power in the ring is larger/smaller than the optimal power, the heater code is incremented/decremented. The sign of the feedback loop is user-configured.

In addition, a bypass state allows the heat output code to be configured manually through a scan chain.

An example of the thermal controller functionality is shown in Fig. 5.7. In Fig. 5.7a), the maximum slope point is tracked. The ring locks to the largest slope value observed during the scan stage. Note that the slope lock point is to the right of resonance in the heater-sweep domain; this corresponds to a ring resonance wavelength which is larger than the laser wavelength, and thus puts the ring in the thermally stable side of operation [46]. In Fig. 5.7b), the maximum power point is tracked.

Finally, the chip features two-phase latch based scan chains to allow user configuration. This configuration is used to adjust bias currents through current DACs, as well as amplifier gain settings. In addition, each channel can be reset and entered into a low power state through the digital configuration. Finally, the scan chains allows the thermal controller to be monitored and configured.

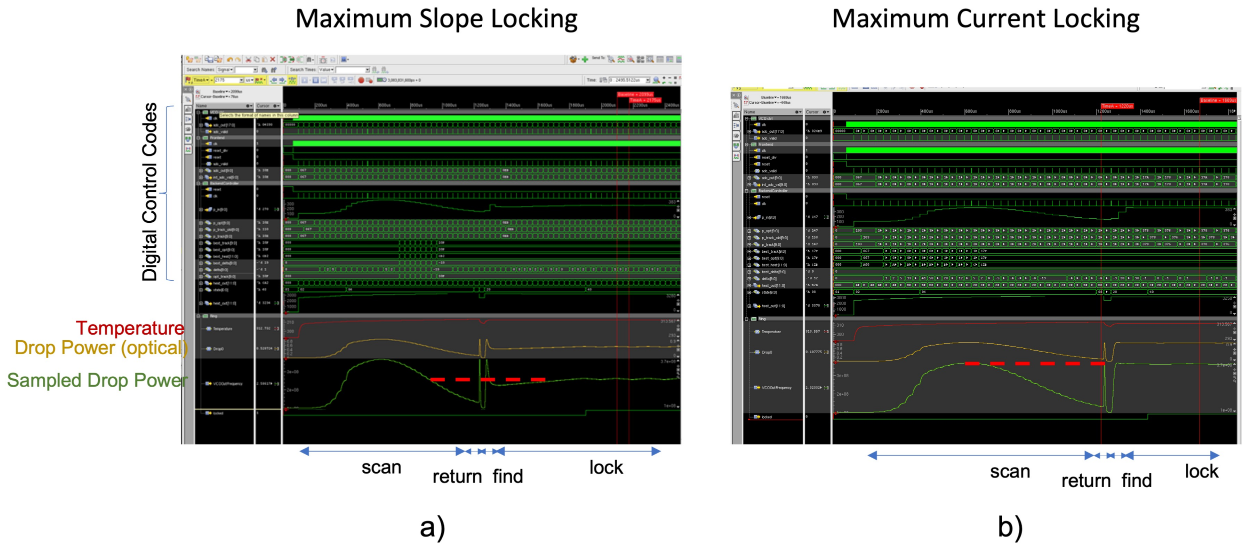

Figure 5.7: a) Maximum slope locking, used for TX rings. b) Maximum power locking, used for RX rings. Both sequences show the thermal loop controller sweeping the ring heater such that the ring resonance passes through the laser wavelength. Red dashed lines show that during lock, the thermal tuning controller tracks maximum slope point, in a), and maximum power point, in b).

5.7 Chip Integration and Packaging

The MRI analog link was taped out in GlobalFoundries 45nm RFSOI platform. A die micrograph is shown in Figure 5.8. The insets detail the MRI receiver and microring driver (the transmit portion of the optical link) on the left, and the optical receiver on the right.

Packaging of the die required special steps in order to enable the photonic devices on the chip. This procedure is detailed below, and in Fig. 5.9

1. **Flip-chip die attach** The die is flip-chip attached onto a high-density PCB. The underwent a copper pillar bumping processes prior to flip chip attach. Underfill epoxy (Namics U8410) is added to provide mechanical support. See Fig. 5.9a).

2. **Substrate release** The die undergoes a XeF2 etch to remove the silicon wafer substrate. The etch naturally stops at the buried oxide layer. Etching the subtrate is necessary to enable the photonic devices; without the etch, the optical mode leaks into the substrate, causing high loss. The underfill fillet protects the active device layer and BEOL stack. See Fig. 5.9b).

3. **Underfill sidewall removal** The underfill sidewall must be removed because it is now taller than the remaining chip and prevents the fiber block from landing on the surface

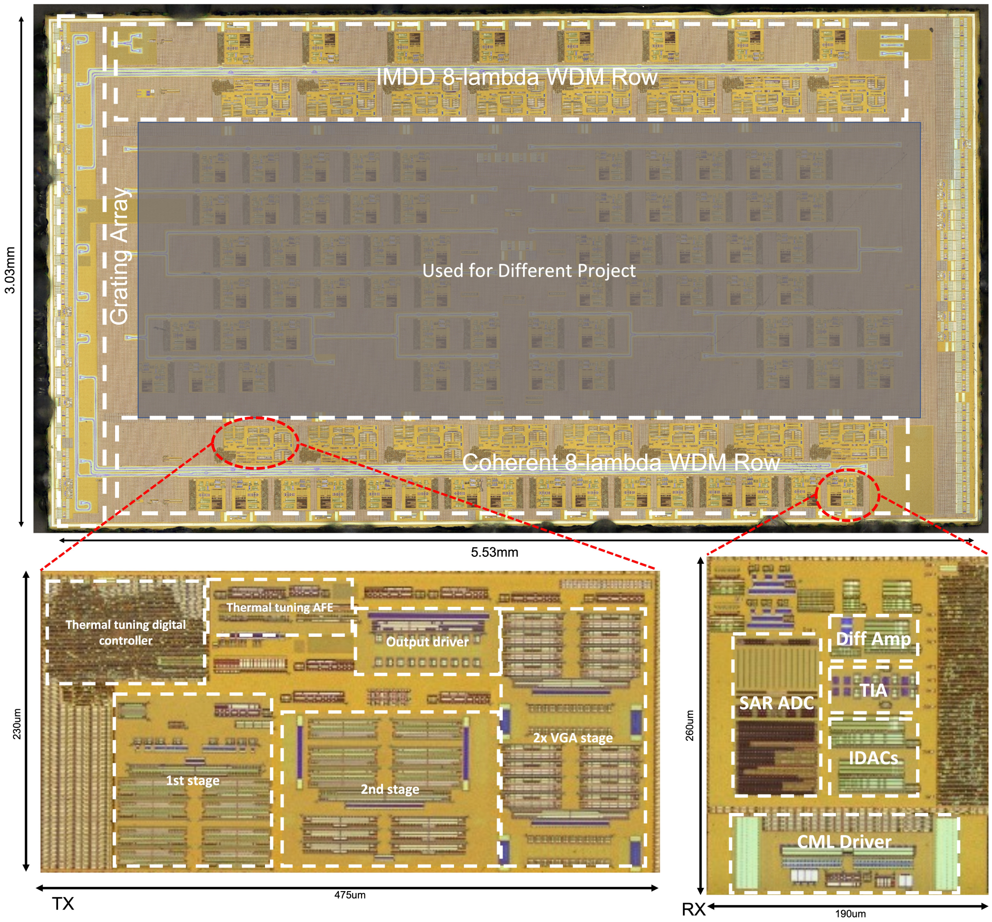

Figure 5.8: Die micrograph of MRI analog link chip. Insets detail the transmitter (MRI receiver and optical driver) and receiver.

of the BOX layer. A nitric acid etch is performed to remove the underfill epoxy. See Fig. 5.9c).

4. **Fiber attach:** To provide stable optical coupling into and out of the chip, a 12-channel fiber block (250 μm pitch) is attached. To assign in alignment, the loopback structures in the grating array are used. The fiber block is secured to the chip using a UV cured epoxy (NOA-61). See Fig. 5.9d).

Images of the chip on board package before post-processing and after fiber attach can be seen in Figs. 5.9e-f.

A host board was designed to provide the multiple supplies, bias voltages and currents, and control signals, Fig. 5.10. The host board includes a zero insertion force socket to hold the chip-on-board package. It also features 16 input and 16 output channels with on-

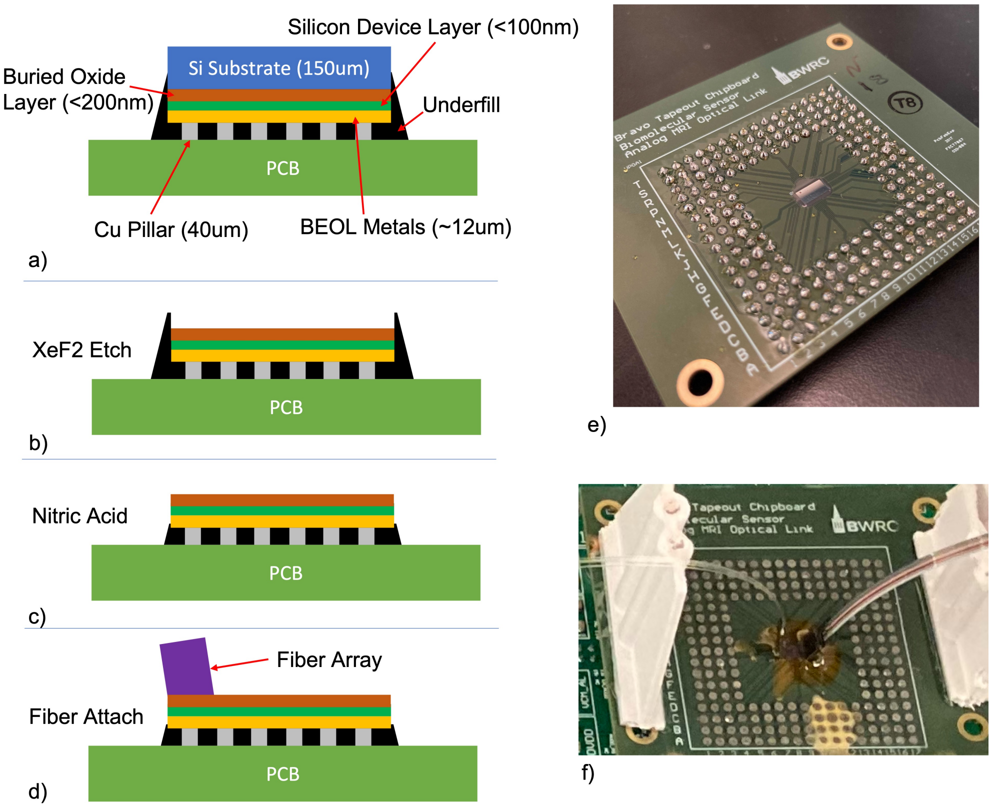

Figure 5.9: a-d) Packaging flow including flip chip attach, XeF2 substrate etch, nitric acid sidewall etch, and fiber attach. e-f) Flip chip package before and after post-processing.

board matching networks. An external FPGA provides an interface between a Python chip control framework and the hostboard and chip. The Python firmware controls the board configuration, such as enabling proper power sequencing, the chip scan chain interface, as well as controlling test equipment.

5.8 Measurement Results and Current Status

5.8.1 Passive Optical Characterization

Characterization of the MRI analog link chip began with passive optical scans of the transmit and receive optical rows, shown in Fig. 5.11. The eight ring resonances in the TX and RX rows are visible. The more gradual wavelength-dependent loss on which the ring resonances are superimposed is the wavelength response of the grating couplers.

The quality factor of the transmit rings is roughly $Q = 10k$, in agreement with the value used in the model. The quality factor of the receive rings is $Q = 10.5k$ The FSR is roughly

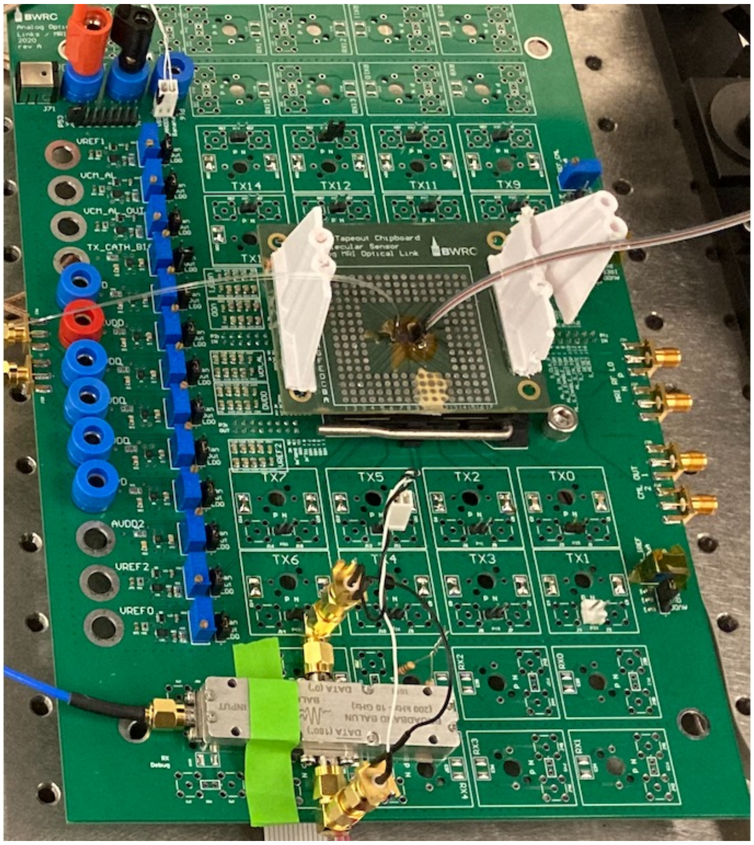

Figure 5.10: Host board in test setup for MRI system. Chip board in zero insertion force socket with fiber attach and fiber stress relief posts shown in center of board.

18 nm. The ring order is initially unknown, as resonance position can vary with fabrication variation within an FSR. The mapping of TX/RX macro number to ring resonance position was determined by performing a one-time calibration sweep, in which the heat codes of the rings were sequentially toggled as the laser was swept through an FSR. The resonance positions of each ring were stored in a calibration file for subsequent lookup. The nonuniform wavelength spacing of the rings occurs was an intentional design choice to accommodate two different laser sources. The tighter ring spacing was chosen to interface with an Innolume comb laser source with 80 GHz laser channel spacing. The broader ring spacings were designed to evenly span the remainder of the FSR, to accommodate multi-wavelength sources which maximize channel spacing within an FSR.

Finally, passive optical scans of the loopback structures on the grating array were performed to deembed the insertion loss of each grating coupler. The insertion loss was determined to be roughly 7 dB per grating. This loss is significantly larger than the 2dB estimated loss per coupling in the link model. This loss is due to non-idealities in the fiber attach flow.

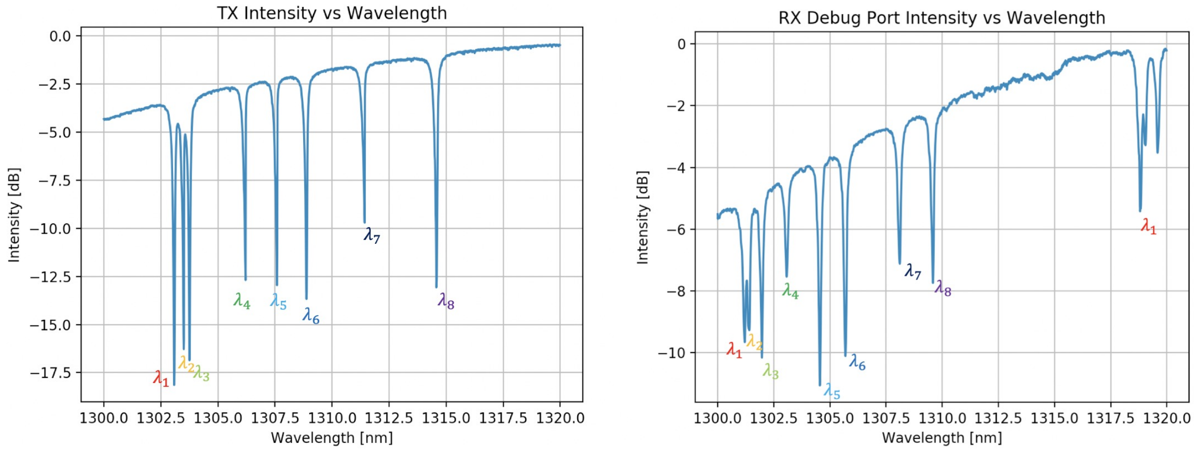

Figure 5.11: Passive optical scans through the TX (left) and RX (right) optical rows. Insertion loss is normalized to the peak transmission. Wavelength numbering indicates the 8 resonances (not in order of TX/RX macro number).

During fiber attach, a 6-axis positioning stage is used to align the fiber array block with the grating array. The peak insertion loss achieved after alignment was roughly 2.5 dB. However, during UV cure of the epoxy, linear shrinkage occurs, causing the fiber array to move out of alignment. It was found during multiple fiber attach procedures that attempting to manually correct for the shrinkage during a slow UV curing process was likely to move the fibers further from alignment.

5.8.2 Experimental Setup

To characterize the electrical performance of the link, a two-tone test is performed. The setup is shown in Fig. 5.12. A two-output signal generator (Keysight 81160A) produces the two input tones. The tones go through a discrete combiner, followed by a fixed 20 dB attenuator and a variable (0 dB to 11 dB) attenuator (HP 8494A). Finally, the input goes through a balun (Marki BALH0003) to produce the differential electrical input signal to the optical transmitter.

A tunable laser (Santec TSL550) is fed into a polarization controller. To overcome the high optical loss due to the grating couplers, the modulated optical output is passed through an optical fiber amplifier (ThorLabs BOA1130P). A tunable in-line filter is used after the BOA to reduce the contribution of amplified spontaneous emission (ASE) noise. Two 90/10 splitters are used to tap out some optical power to an optical spectrum analyzer (Yokogawa AQ6370C) and an optical power meter (Agilent 81635A) to aid in filter alignment and optical power monitoring. The optical signal is fed into an external photodetector (ThorLabs PDB450C), and finally into an electrical spectrum analyzer (Agilent N9030A).

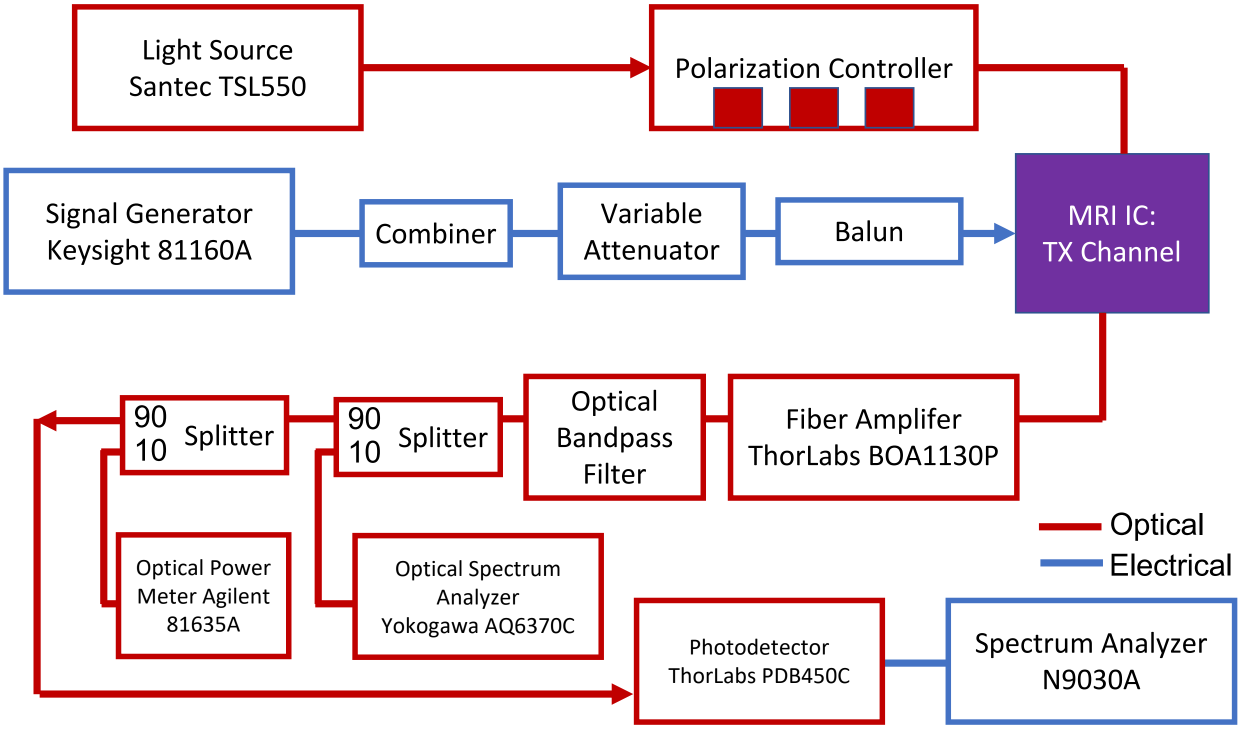

Figure 5.12: Experimental setup to perform two-tone linearity characterization. Red boxes and arrows indicate optical equipment and signal flow. Blue boxes and arrows indicate electrical equipment and signal flow.

To achieve the lowest effective noise floor, the link should be limited by shot noise. First, to overcome the large insertion loss of the gratings, the input laser power was set to 8 dBm. In addition, the bias current of the BOA (affecting its gain) was swept with no signal input to the modulator, and the noise floor on the electrical spectrum analyzer was observed in conjunction with the optical power monitor. The BOA was biased in the regime such that each dB change in optical power affected a corresponding dB change in the noise floor, indicating that the noise floor was limited by shot noise. The optical power impinging on the photodetector was limited to roughly 0 dBm to avoid any linearity limitations of the PDB450C photodetector.

A two tone test was performed. The linear amplifier was configured to its minimum gain setting, including bypass of the first gain stage. A pair of input tones at 29.9 MHz and 30.1 MHz was applied, at a fixed modulation amplitude of 500 mVpp. The attenuator at the input of the link was set to 27 dB, implying an input voltage of roughly $v_{amp,in} = 2\,\text{mV}$ after the combiner loss, balun splitting loss, and excess loss. In this state, the laser was swept from 600 pm below the ring wavelength to 100 pm above the ring wavelength in increments of 10 pm. At each laser wavelength, the total optical power (10% tap) hitting the photodetector

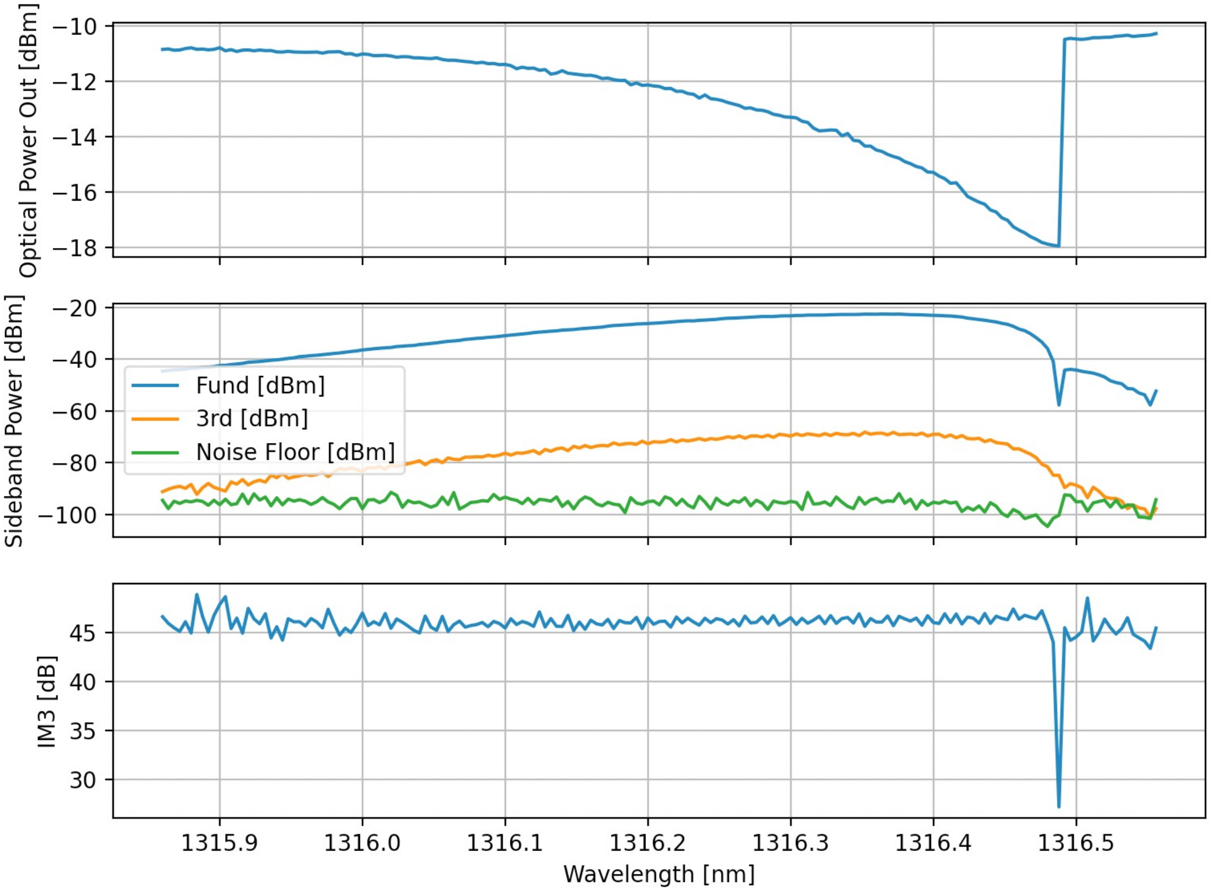

Figure 5.13: Linearity of the optical link versus offset wavelength from resonance. (Top) Optical power into the photodetector. A strong self-heating effect is observed, generating the asymmetric Lorentzian shape. (Middle) Spectrum analyzer power levels of the fundamental and third order intermodulation sidebands, as well as the noise floor. (Bottom) IM3 linearity of the link.

was recorded, as well as the power in each sideband and the noise floor of the spectrum analyzer.

The results of this sweep are shown in Fig. 5.13. The top graph in Fig. 5.13 show the optical power into the photodetector. The curve produced is due to the Lorentzian-shaped insertion loss of the microring modulator. A strong self heating effect can be observed due to the high optical input power (8 dBm), which causes the flattened Lorentzian to the left of resonance and the sharp jump in optical power just after the resonance wavelength is reached. The central plot show the powers of the fundamental and third order intermodulation sidebands recorded by the electrical spectrum analyzer, as well as the noise floor. The noise floor is recorded to ensure the validity of the measurement (ie, ensure that the

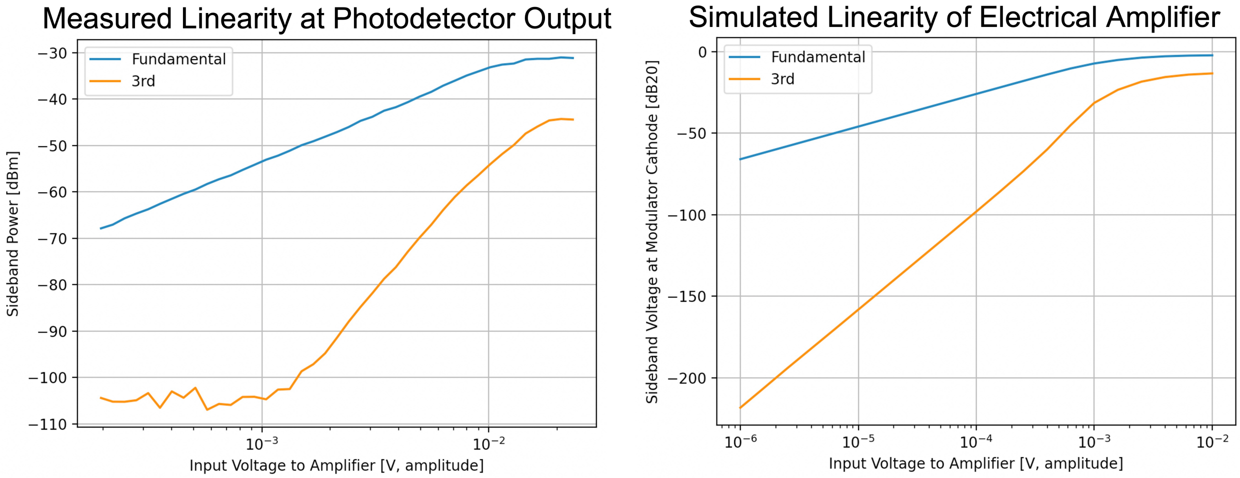

Figure 5.14: (left) Measured linearity of the optical link versus input voltage into the electrical amplifier. (right) Simulated linearity of the electrical amplifier versus input voltage at the same gain settings.

sidebands are not buried in the noise floor). The fundamental and third order sidebands are both observed to increase at the same rate as the laser wavelength approaches the resonance wavelength, plateau, and then fall sharply. This behavior is due to the wavelength offset dependent modulation efficiency (discussed in Fig. 4.13). The IM3 linearity (the difference between the fundamental and third order intermodulation sidebands) is plotted in the bottom of Fig. 5.13. That the IM3 is constant suggests that the electrical amplifier limits the linearity, preventing observation of the linearity peaking of the microring modulator shown in Fig. 5.3.

To investigate this further, another two tone test was performed. In this test, the laser was biased at the wavelength that maximized the fundamental output tone (ie, provided the greatest modulator gain), which in simulation (Fig. 4.17) is very near the wavelength that maximizes third-order linearity. The input modulation amplitude was then swept with a fixed input attenuation of 28 dB, while the fundamental and third order intermodulation sideband powers were recorded on the electrical spectrum analyzer. The results are shown on the left of Fig. 5.14. It can be seen that at low input powers, the third order intermodulation sideband falls below the noise floor. The input optical power was set to 10 dBm and the BOA was set to deliver roughly 0 dBm total optical power into the photodetector. The SFDR in Fig. 5.14 is measured to be 54.5 dB. With the 24 Hz resolution bandwidth of the measurement, the third-order SFDR is calculated to be 63 $\mathrm{dBHz}^{2/3}$.

It is useful to compare the linearity results with those of the simulation. The plot on the right of Figure 5.14 shows the simulated linearity of the electrical amplifier configured to the same gain settings and with the same current bias configurations as the experimental results. The absolute values of the sideband amplitudes cannot be directly compared, as this plot shows the electrical output voltage of the amplifier, while the plot on the left shows the sideband amplitude of the entire link. However, the IIP3 for each plot can be compared. The experimental data suggest an IIP3 of 33 mV while the simulated data suggest an IIP3 of 19 mV. These results are similar enough to suggest that there is no additional nonlinearity source that is limiting the measured response. From this result, it therefore seems that the linearity of the optical link is limited by the linearity of the electrical preamplifier, rather than the linearity of the optical link. The simulated power consumption of the transmit chain is 54 mW per channel. Unfortunately, due to design bugs in the project which shares the same die, excessive current is pulled from the same supply as powers the MRI transmitter, making it challenging to reliably measure the power consumption on the die.

5.9 Conclusion

This chapter described a proof-of-concept WDM analog optical link for data remoting in MRI systems using microring modulators. The noise and linearity models from Chapter 4 indicate that the optical link supports an IM3 linearity above 50 dB and a sub 1 dB SNR degradation for an input voltage of $V_{amp} = 0.4\,\text{V}$ with an SNR of 55 dB. A linear preamplifier chain was designed with tunable gain from 40 dB to 80 dB to amplify the input MRI signal to this swing. The total end-to-end link was simulated achieve a noise figure below 2 dB. An 8-channel WDM link IC was implemented in GlobalFoundries 45nm process.

The measured third-order SFDR is 63 dB, and corresponds to a peak IM3 of 54.5 dB at 1 mV input amplitude. The measurement results suggest that the linearity of the link is limited by the electrical amplifier, preventing the IM3 linearity peaking suggested in Fig. 5.3 from being observed. Additional work is required to determine which noise sources contribute most strongly to the noise floor in the measurements. Better fiber attach to reduce the insertion loss can greatly improve the noise performance of the link. An improved noise performance would allow the input amplitude to reduced, enabling superior linearity performance of the amplifier. It is left to collaborators on this work to determine whether the link, with its current performance, is suitable for MRI data remoting demonstrations.

Chapter 6

Conclusion

Silicon photonics has the potential to address some of the key I/O scaling and data bandwidth bottlenecks that will limit future wireless systems and sensor networks. The goals of this work are to investigate and address some of the key system implementation and scaling challenges that will enable increased bandwidth density and energy efficiency in silicon photonic links. The author was fortunate to have experienced the full design flow for silicon photonics systems, including model development, system level simulation, photonic device design and circuit design, top-level chip integration, tapeout, and measurement. Throughout this process, new tools, link models, and system design frameworks have been developed to aid the design and implementation of novel photonic systems.

6.1 Key Contributions

First, a new photonic system design framework called Berkeley Photonics Generator (BPG) was developed. BPG enables the development of large-scale, customizable, and process-portable photonic integrated circuit generators, which encapsulate parameterized design methodologies for producing layouts, schematics, and testbenches. Within BPG, technology-specific parameters are abstracted away, and a DRC-cleaning '*photonic compiler*' is utilized to produce implementations in particular technology nodes. BPG's modular framework allows compatibility with 3rd party industry standard tools, such as Lumerical, Cadence, and Mentor Graphics to enable closed-loop optical design, multi-physics simulation, design verification, and seamless electronic-photonic integration. This framework has already been used in several technology nodes and across several organizations to implement large-scale systems, including high speed optical links, photonic molecular biosensors and ultrasound sensing systems, and cryogenic egress links. From the author's experience, utilizing BPG vastly improves the design time and enables more complex electro-optic systems to be designed than could be with previous tools.

Next, a new framework for modeling crosstalk and insertion loss penalty for digital optical links was described. This framework provides intuitive understanding for the receive-filter imposed limitations of channel densification in optical links. The major sources of signal impairment including in-band channel attenuation, crosstalk, and ISI were characterized as functions of technology parameters and system design choices. It was found that insertion loss, and therefore intrinsic quality factor, plays a dominant role in eye closure penalty. The framework was used to select the optimal ring filter design parameters for a given technology node, channel spacing, and target datarate. The framework showed that higher order filters offer limited utility, as the increased insertion loss mitigates the improved channel isolation unless operating at extreme quality factors and datarates. The modeling framework can be applied to most of today's silicon photonic platforms to provide architecture guidelines and optimize receive filter design as channel counts scale in future systems.

Finally, this work proposed analog modulation as an alternative signaling modality in optical links. The theoretical gain, noise, and linearity performance limits were derived. Microring modulators were shown to provide competitive linearity and noise performance for analog links, enabling simple channel count scaling through WDM. A proof-of-concept microring-resonator-based analog optical link system for magnetic resonance imaging data remoting was proposed. An 8-wavelength WDM analog link was implemented in Global Foundries 45nm RFSOI platform. Circuit implementation details and the packaging flow required for this monolithic electronic-photonic IC were described.

6.2 Future Work

Berkeley Photonics Generator

The Berkeley Photonics Generator provides a unified open-source framework for photonic system design. However, new features and improvements can make the tool even more useful for designers.

- **Plugins for Open-Source Simulators:** BPG's plugin architecture can support additional simulation tools. Creating a plugin for open-source simulation tools, such as MEEP [109], would allow designs to utilize a fully free and public tool to perform optical design and verification.

- **Open Source Layout Versus Schematic:** Layout versus schematic verification is critical to ensure the integrity of any design. Currently, BPG is able to utilize proprietary tools such as Mentor's Calibre to extract the layout netlist. Implementing a netlist-extraction engine in open source tools such as KLayout [13] can enable more designers to access these features.

- **Open Source Behavioral Simulation:** Behavioral simulation is a key element of system design. BPG's netlist-extraction can be used to generate schematics which utilize VerilogA compact models [21] within the Virtuoso design tool. More work is needed to develop plugins for additional time-domain behavioral simulation tools, such as Simulink [94] or others.

BPG is open source, so all contributions are welcome!

Channel Modeling

The crosstalk model presented in this work studied the design and performance tradeoffs limited to microring drop filters within the receiver. However, the optical channel impairments caused by microring modulators in the transmitter were not including in this work. Because of the dynamic behavior of microring modulators, additional work is needed to develop accurate time-domain models. Potential areas for study include optimizing the ring design for a given datarate under tight channel spacing constraints, and exploring the sensitivity of transmit-side crosstalk and ISI to process variation.

Analog Optical Links

- **Continued Characterization of MRI Link:** This work presented a proof of concept analog optical link for MRI applications. Additional testing is needed to determine what limits the noise floor at the photodetector. In addition, better fiber attach can be performed on new samples to achieve lower insertion loss, improving the noise performance of the link. Finally, it would be interesting to demonstrate data remoting for MRI image data, even with the limited noise performance.
- **High Frequency Analog Links:** Ring-based analog modulation may prove more suitable for applications with higher datarates and less stringent linearity and noise requirements. One such application might be in data remoting for mm-wave data in antenna arrays or base stations. Novel optical architectures such as multi-resonant ring modulators [76, 110] allow for efficient narrow-band high frequency modulation. Such devices, combined with appropriately designed pre-amplifiers, can provide inherently WDM-compatible solutions to high-speed data remoting.
- **Feedback Linearization:** At lower datarates, feedback can be used to create a more linear modulation response. For example, the weakly-coupled drop port on the modulator is often used to provide a monitor signal for thermal tuning. This same signal can instead be used with an appropriately designed error amplifier and loop filter to create a stable feedback loop around the electrical driver and ring modulator. Such feedback can enable a more linear transmission response.

6.3 Final Remarks

Silicon photonics is an exciting and interesting field, both for its applications and inherent beauty. Analog optical modulation in particular holds promise for energy efficient links, and there are many innovative solutions available to provide practical I/O scaling. I feel fortunate to have worked on so many aspects of electro-optic system design, from photonic device design to top-level chip integration and modeling, and am excited by the systems silicon photonics will enable.

Bibliography

[1] E. Timurdogan *et al.*, “400g silicon photonics integrated circuit transceiver chipsets for cpo, obo, and pluggable modules,” *Optics InfoBase Conference Papers*, vol. Part F174-, pp. 2020–2022, 2020. DOI: `10.1364/OFC.2020.T3H.2`.

[2] K. Hosseini *et al.*, “8 tbps co-packaged fpga and silicon photonics optical io,” *2021 Optical Fiber Communications Conference and Exhibition, OFC 2021 - Proceedings*, pp. 1–3, 2021. DOI: `10.1364/ofc.2021.th4a.2`.

[3] V. M. Stojanović, P. Bhargava, S. Buchbinder, and J. Kim, “Epda for epsoc design: From co-simulation to photonic circuit generators,” in *Design Automation and Test in Europe (DATE)*, 2019.

[4] P. Zarkos *et al.*, “Monolithically integrated electronic-photonic ultrasound receiver using microring resonator,” *2021 Conference on Lasers and Electro-Optics, CLEO 2021 - Proceedings*, pp. 2021–2022, 2021. DOI: `10.1364/cleo_si.2021.sth1h.2`.

[5] C. Adamopoulos *et al.*, “Fully integrated electronic-photonic biosensor for label-free molecular sensing in advanced zero-change cmos-soi process,” *2021 Conference on Lasers and Electro-Optics, CLEO 2021 - Proceedings*, pp. 4–5, 2021. DOI: `10.1364/cleo_at.2021.jm4d.3`.

[6] C. Adamopoulos *et al.*, “Lab-on-chip for everyone: Introducing an electronic-photonic platform for multiparametric biosensing using standard cmos processes,” *IEEE Open Journal of the Solid-State Circuits Society*, vol. 1, no. October, pp. 198–208, 2021. DOI: `10.1109/ojsscs.2021.3118336`.

[7] M. Wade *et al.*, “An error-free 1 tbps wdm optical i/o chiplet and multi-wavelength multi-port laser,” *2021 Optical Fiber Communications Conference and Exhibition, OFC 2021 - Proceedings*, no. c, pp. 6–8, 2021. DOI: `10.1364/ofc.2021.f3c.6`.

[8] S. Buchbinder *et al.*, “Silicon microring modulator for high sfdr analog links in monolithic 45nm cmos,” in *Conference on Lasers and Electro-Optics*, 2022.

[9] M. Fiers *et al.*, “Improving the design cycle for nanophotonic components,” *Journal of Computational Science*, vol. 4, no. 5, pp. 313–324, 2013, ISSN: 1877-7503. DOI: `10.1016/j.jocs.2013.05.008`. [Online]. Available: `http://dx.doi.org/10.1016/j.jocs.2013.05.008`.

[10] L. H. Gabrielli, *Gdspy*. [Online]. Available: `https://github.com/heitzmann/gdspy`.

[11] Synopsys, *Photonic Solutions.* [Online]. Available: `https://www.synopsys.com/photonic-solutions.html`.

[12] Cadence, *Integrated Design Flows for Photonics Circuits.* [Online]. Available: `https://www.cadence.com/en_US/home/solutions/photonics.html`.

[13] M. Köfferlein, *KLayout.* [Online]. Available: `https://www.klayout.de/`.

[14] *BPG.* [Online]. Available: `https://github.com/BerkeleyPhotonicsGenerator/BPG`.

[15] P. Zarkos *et al.*, "Fully integrated electronic-photonic ultrasound receiver array for endoscopic imaging applications in a zero-change 45nm cmos-soi process," in *2021 Symposium on VLSI Circuits*, IEEE, 2021, in press.

[16] E. Chang, N. Narevsky, K. Settaluri, and E. Alon, "BAG: A Process-Portable Framework for Generator-based AMS Circuit Design," *Proceedings of the Custom Integrated Circuits Conference*, 2019, ISSN: 08865930. DOI: `10.1109/CICC.2019.8780349`.

[17] L. Alloatti, M. Wade, V. Stojanovic, M. Popovic, and R. J. Ram, "Photonics design tool for advanced CMOS nodes," *IET Optoelectronics*, vol. 9, no. 4, pp. 163–167, 2015, ISSN: 17518768. DOI: `10.1049/iet-opt.2015.0003`.

[18] C. Sun *et al.*, "Teraphy : An o-band wdm electro-optic platform for low power , terabit / s optical i / o," 2020, pp. 1–2, ISBN: 9781728164601.

[19] Siemens EDA, *Calibre Design Solutions.* [Online]. Available: `https://eda.sw.siemens.com/en-US/ic/calibre-design/`.

[20] Ansys/Lumerical, *High-Performance Photonic Simulation Software - Lumerical.* [Online]. Available: `https://www.lumerical.com/`.

[21] C. Sorace-Agaskar, J. Leu, M. R. Watts, and V. Stojanovic, "Electro-optical co-simulation for integrated cmos photonic circuits with veriloga.," *Optics express*, vol. 23, no. 21, pp. 27 180–203, 2015, ISSN: 1094-4087. DOI: `10.1364/OE.23.027180`.

[22] Cadence Design Systems, *Circuit Design.* [Online]. Available: `https://www.cadence.com/en_US/home/tools/custom-ic-analog-rf-design/circuit-design.html`.

[23] P. Agnello et al., "High performance 45-nm soi technology with enhanced strain, porous low-k beol, and immersion lithography," in *2006 International Electron Devices Meeting*, 2006, pp. 1–4. DOI: `10.1109/IEDM.2006.346879`.

[24] M. Rakowski *et al.*, "45nm cmos - silicon photonics monolithic technology (45clo) for next-generation, low power and high speed optical interconnects," in *Optical Fiber Communication Conference (OFC) 2020*, Optical Society of America, 2020, T3H.3. DOI: `10.1364/OFC.2020.T3H.3`. [Online]. Available: `http://www.osapublishing.org/abstract.cfm?URI=OFC-2020-T3H.3`.

[25] A. Leinse *et al.*, "TriPleX waveguide platform: low-loss technology over a wide wavelength range," in *Integrated Photonics: Materials, Devices, and Applications II*, International Society for Optics and Photonics, vol. 8767, SPIE, 2013, pp. 86–98. DOI: `10.1117/12.2020574`. [Online]. Available: `https://doi.org/10.1117/12.2020574`.

[26] Applied Nanotools Inc, *NanoSOI Fabrication.* [Online]. Available: `https://www.appliednt.com/nanosoi-fabrication-service/`.

[27] N. M. Fahrenkopf, C. McDonough, G. L. Leake, Z. Su, E. Timurdogan, and D. D. Coolbaugh, "The aim photonics mpw: A highly accessible cutting edge technology for rapid prototyping of photonic integrated circuits," *IEEE Journal of Selected Topics in Quantum Electronics*, vol. 25, no. 5, pp. 1–6, 2019. DOI: `10.1109/JSTQE.2019.2935698`.

[28] J. M. F. Cabanillas and M. A. Popović, "Fast adiabatic mode evolution based on geometry-induced suppression of nearest-mode crosstalk," in *2018 Conference on Lasers and Electro-Optics (CLEO)*, 2018, pp. 1–2.

[29] J. M. F. Cabanillas, B. Zhang, and M. A. Popović, "Demonstration of 3±0.12 db power splitting over 145 nm optical bandwidth in a 31-um long 3-db rapid adiabatic coupler," in *2020 Optical Fiber Communications Conference and Exhibition (OFC)*, 2020, pp. 1–3.

[30] J. F. Cabanillas, D. Kita, A. Khilo, F Sedgwick, J. Fini, M. Popovic, M. Wade, "Demonstration and fabrication tolerance study of a low-loss,ultra-broadband rapid adiabatic 3-db coupler in a next-generation 45 nm monolithic electronic-photonic platform," in *Optical Fiber Communication Conference (OFC) 2021*, Optical Society of America, 2021, Tu5B.4.

[31] H. Gevorgyan et al., "High shift efficiency o-band spoked-ring modulator allowing fully electro-optic channel tuning in a 45nm cmos platform," in *2021 Conference on Lasers and Electro-Optics (CLEO)*, 2021.

[32] M. Wade et al., "Teraphy: A chiplet technology for low-power, high-bandwidth in-package optical i/o," *IEEE Micro*, vol. 40, no. 2, pp. 63–71, 2020. DOI: `10.1109/MM.2020.2976067`.

[33] C. Adamopoulos *et al.*, "Fully integrated electronic-photonic sensor for label-free refractive index sensing in advanced zero-change cmos-soi process," in *2021 IEEE Custom Integrated Circuits Conference (CICC)*, IEEE, 2021, pp. 1–2.

[34] H. Gevorgyan, A. Khilo, D. Van Orden, D. Onural, B. Yin, M. T. Wade, V. M. Stojanović, and M. A. Popović, "4cryo-compatible, silicon spoked-ring modulator in a 45nm cmos platform for 4k-to-room-temperature optical links," in *Optical Fiber Communication Conference (OFC) 2021*, Optical Society of America, 2021, M3B.3.

[35] C. Sun *et al.*, "Teraphy : An o-band wdm electro-optic platform for low power , terabit / s optical i / o," *IEEE Symposium on VLSI Circuits, Digest of Technical Papers*, pp. 31–32, 2020.

[36] C. Sun *et al.*, “Single-chip microprocessor that communicates directly using light,” *Nature*, vol. 528, no. 7583, pp. 534–538, 2015, ISSN: 0028-0836. DOI: `10.1038/nature16454`.

[37] S. Rumley, D. Nikolova, R. Hendry, Q. Li, D. Calhoun, and K. Bergman, “Silicon photonics for exascale systems,” *Journal of Lightwave Technology*, vol. 33, no. 3, pp. 547–562, 2015, ISSN: 07338724. DOI: `10.1109/JLT.2014.2363947`.

[38] P. J. Winzer and R.-J. Essiambre, “Advanced optical modulation formats,” *Proceedings of the IEEE*, vol. 94, no. 5, 2006.

[39] W. Bogaerts *et al.*, “Silicon microring resonators,” *Laser and Photonics Reviews*, vol. 6, no. 1, pp. 47–73, 2012, ISSN: 18638880. DOI: `10.1002/lpor.201100017`. arXiv: `arXiv:1208.0765v1`.

[40] B. E. Little, S. T. Chu, H. A. Haus, J. Foresi, and J. Laine, “Microring resonator channel dropping filters,” *Journal of Lightwave Technology*, vol. 15, no. 6, pp. 998–1005, 1997.

[41] GlobalFoundries, “Advanced 45nm rf soi technology,” pp. 1–2, 2008.

[42] A. Yariv, “Critical coupling and its control in optical waveguide-ring\nresonator systems,” *IEEE Photonics Technology Letters*, vol. 14, no. 4, pp. 2001–2003, 2002.

[43] M. Soltani, Q. Li, S. Yegnanarayanan, and A. Adibi, “Toward ultimate miniaturization of high q silicon traveling-wave microresonators,” *Optics Express*, vol. 18, no. 19, p. 19 541, 2010, ISSN: 1094-4087. DOI: `10.1364/oe.18.019541`.

[44] J. Heebner, R. Grover, and T. Ibrahim, *Optical Microresonators: Theory, fabrication, and applications*. 2008, vol. 138, pp. 1–266, ISBN: 9780387730677.

[45] M. R. Watts, “Adiabatic microring resonators,” *Optics Letters*, vol. 35, no. 19, p. 3231, 2010, ISSN: 0146-9592. DOI: `10.1364/ol.35.003231`.

[46] C. Sun *et al.*, “A 45 nm cmos-soi monolithic photonics platform with bit-statistics-based resonant microring thermal tuning,” *IEEE Journal of Solid-State Circuits*, vol. 51, no. 4, pp. 893–907, 2016, ISSN: 00189200. DOI: `10.1109/JSSC.2016.2519390`.

[47] H. A. Haus, *Waves and Fields in Optoelectronics*. Engelwood Cliffs, NJ: Prentice Hall, 1984.

[48] A. V. Krishnamoorthy *et al.*, “Exploiting cmos manufacturing to reduce tuning requirements for resonant optical devices,” *IEEE Photonics Journal*, vol. 3, no. 3, pp. 567–579, 2012, ISSN: 1943-0647. DOI: `10.1109/jphot.2011.2140367`.

[49] W. A. Zortman, D. C. Trotter, and M. R. Watts, “Silicon photonics manufacturing,” *Optics Express*, vol. 18, no. 23, p. 23 598, 2010, ISSN: 1094-4087. DOI: `10.1364/oe.18.023598`.

[50] J. C. Mikkelsen, W. D. Sacher, and J. K. S. Poon, “Dimensional variation tolerant silicon-on-insulator directional couplers,” *Optics Express*, vol. 22, no. 3, p. 3145, 2014, ISSN: 1094-4087. DOI: `10.1364/oe.22.003145`.

[51] G. Li *et al.*, "Ring resonator modulators in silicon for interchip photonic links," *IEEE Journal on Selected Topics in Quantum Electronics*, vol. 19, no. 6, 2013, ISSN: 1077260X. DOI: `10.1109/JSTQE.2013.2278885`.

[52] V. Stojanović *et al.*, "Monolithic silicon-photonic platforms in state-of-the-art cmos soi processes [invited]," *Optics Express*, vol. 26, no. 10, p. 13 106, 2018, ISSN: 1094-4087. DOI: `10.1364/oe.26.013106`.

[53] M. T. Wade, "Devices and systems-on-chip for photonic communication links in a microprocessor," Ph.D. dissertation, 2015.

[54] K. H. Muller and M. Mueller, "Timing recovery in digital synchronous data receivers," *IEEE Transactions on Communications*, vol. 24, no. 5, 1976.

[55] B. Razavi, "Challenges in the design of high-speed clock and data recovery circuits," *IEEE Communications Magazine*, vol. 40, no. 8, pp. 94–101, 2002, ISSN: 01636804. DOI: `10.1109/MCOM.2002.1024421`.

[56] M. Sysak, J. Johnson, D. Lewis, and C. Cole, "Cw-wdm msa technical specifications," Tech. Rep., 2021, pp. 1–25.

[57] A. Mirza, F. Sunny, P. Walsh, K. Hassan, S. Pasricha, and M. Nikdast, "Silicon photonic microring resonators: A comprehensive design-space exploration and optimization under fabrication-process variations," *IEEE Transactions on Computer-Aided Design of Integrated Circuits and Systems*, vol. 0070, no. c, pp. 1–1, 2021, ISSN: 0278-0070. DOI: `10.1109/tcad.2021.3132555`.

[58] Z. Su *et al.*, "Reduced wafer-scale frequency variation in adiabatic microring resonators," *Optical Fiber Communication Conference, OFC 2014*, vol. 1, no. c, pp. 31–33, 2014.

[59] X. Chen, M. Mohamed, Z. Li, L. Shang, and A. R. Mickelson, "Process variation in silicon photonic devices," *Applied Optics*, vol. 52, no. 31, pp. 7638–7647, 2013, ISSN: 15394522. DOI: `10.1364/AO.52.007638`.

[60] N. Boynton, A. Pomerene, A. Starbuck, A. Lentine, and C. T. Derose, "Characterization of systematic process variation in a silicon photonic platform," *6th IEEE Photonics Society Optical Interconnects Conference, OI 2017*, pp. 11–12, 2017. DOI: `10.1109/OIC.2017.7965506`.

[61] B. E. Little *et al.*, "Very high-order microring resonator filters the wdm applications," *IEEE Photonics Technology Letters*, vol. 16, no. 10, pp. 2263–2265, 2004, ISSN: 10411135. DOI: `10.1109/LPT.2004.834525`.

[62] M. A. Popovic *et al.*, "Multistage high-order microring-resonator add-drop filters," *Optics Letters*, vol. 31, no. 17, pp. 2571–2573, 2006.

[63] F. Xia, M. Rooks, L. Sekaric, and Y. Vlasov, "Ultra-compact high order ring resonator filters using submicron silicon photonic wires for on-chip optical interconnects," *Optics Express*, vol. 15, no. 19, p. 11 934, 2007, ISSN: 1094-4087. DOI: `10.1364/oe.15.011934`.

[64] B. G. Lee, B. A. Small, K. Bergman, Q. Xu, and M. Lipson, "Transmission of high-data-rate optical signals through a micrometer-scale silicon ring resonator," *Optics Letters*, vol. 31, no. 18, p. 2701, 2006, ISSN: 0146-9592. DOI: `10.1364/ol.31.002701`.

[65] J. R. Ong, R. Kumar, and S. Mookherjea, "Ultra-high-contrast and tunable-bandwidth filter using cascaded high-order silicon microring filters," *IEEE Photonics Technology Letters*, vol. 25, no. 16, pp. 1543–1546, 2013, ISSN: 10411135. DOI: `10.1109/LPT.2013.2267539`.

[66] M. A. Popovic *et al.*, "Tunable, fourth-order silicon microring-resonator add-drop filters," in *European Conference and Exhibition of Optical Communications*, vol. 33, 2007.

[67] S. J. Mason, "Feedback theory – further properties of signal flow graphs," *Proceedings of the I.R.E*, vol. 44, no. 7, 1956.

[68] H. Jayatilleka *et al.*, "Wavelength tuning and stabilization of microring-based filters using silicon in-resonator photoconductive heaters," *Optics Express*, vol. 23, no. 19, p. 25 084, 2015, ISSN: 1094-4087. DOI: `10.1364/oe.23.025084`. arXiv: `1507.00686`.

[69] J. E. Cunningham *et al.*, "Highly-efficient thermally-tuned resonant optical filters," *Optics Express*, vol. 18, no. 18, p. 19 055, 2010, ISSN: 1094-4087. DOI: `10.1364/oe.18.019055`.

[70] Y. Ehrlichman, A. Khilo, and M. A. Popović, "Optimal design of a microring cavity optical modulator for efficient RF-to-optical conversion," *Optics Express*, vol. 26, no. 3, p. 2462, 2018, ISSN: 10944087. DOI: `10.1364/oe.26.002462`.

[71] N. Mehta, S. Buchbinder, and V. Stojanovic, "Design and characterization of monolithic microring resonator based photodetector in 45nm soi cmos," *European Solid-State Device Research Conference*, vol. 2019-Septe, pp. 206–209, 2019, ISSN: 19308876. DOI: `10.1109/ESSDERC.2019.8901767`.

[72] M. Lipson, "Guiding, modulating, and emitting light on Silicon - Challenges and opportunities," *Journal of Lightwave Technology*, vol. 23, no. 12, pp. 4222–4238, 2005, ISSN: 07338724. DOI: `10.1109/JLT.2005.858225`.

[73] T. Baehr-Jones *et al.*, "Ultralow drive voltage silicon traveling-wave modulator," *Optics Express*, vol. 20, no. 11, p. 12 014, 2012, ISSN: 1094-4087. DOI: `10.1364/oe.20.012014`.

[74] W. D. Sacher and J. K. S. Poon, "Dynamics of microring resonator modulators.," *Optics express*, vol. 16, no. 20, pp. 15 741–15 753, 2008, ISSN: 1094-4087. DOI: `10.1364/OE.16.015741`.

[75] Y. Ban, J. M. Lee, B. M. Yu, S. H. Cho, and W. Y. Choi, "Small-signal frequency responses for si micro-ring modulators," *2014 IEEE Optical Interconnects Conference, OI 2014*, vol. 7, no. 1, pp. 47–48, 2014. DOI: `10.1109/OIC.2014.6886081`.

[76] H. Gevorgyan, A. Khilo, and M. A. Popović, "Efficient coupled-cavity electro-optic modulator on silicon for high carrier frequency, narrowband rf signals," vol. 1, no. c, FW5C.1, 2019. DOI: `10.1364/fio.2019.fw5c.1`.

[77] L. Alloatti, D. Cheian, and R. J. Ram, "High-speed modulator with interleaved junctions in zero-change cmos photonics," *Applied Physics Letters*, vol. 108, no. 13, pp. 18–21, 2016, ISSN: 00036951. DOI: `10.1063/1.4944999`.

[78] H. Gevorgyan, A. Khilo, M. T. Wade, V. M. Stojanovic, and M. A. Popovic, "Moscap ring modulator with 1.5 um radius, 8.5 thz fsr and 30 ghz/v shift efficiency in a 45 nm soi cmos process," *Optics InfoBase Conference Papers*, no. c, pp. 8–10, 2021. DOI: `10.1364/ofc.2021.th5a.3`.

[79] H. Gevorgyan *et al.*, "High Shift Efficiency O-band Spoked-Ring Modulator Allowing Fully Electro-Optic Channel Tuning in a 45nm CMOS Platform," *2021 Conference on Lasers and Electro-Optics, CLEO 2021 - Proceedings*, no. c, pp. 2–3, 2021. DOI: `10.1364/cleo_si.2021.sw3c.5`.

[80] L. A. Coldren, S. W. Corzine, and M. L. Masanovic, *Diode Lasers and Photonic Integrated Circuits*, 2nd ed. Hoboken: John Wiley & Sons Inc, 2012.

[81] F. Tan, "Signal modulation and relative intensity noise properties of transistor laser and nano-cavity vcsel," Ph.D. dissertation, University of Illinois at Urbana-Champaign, 2013.

[82] R. Paschotta, *Relative intensity noise.* [Online]. Available: `https://www.rp-photonics.com/relative%7B%5C_%7Dintensity%7B%5C_%7Dnoise.html`.

[83] J. Notaros *et al.*, "Ultra-efficient cmos fiber-to-chip grating couplers," pp. 1–3, 2016.

[84] T. L. Marzetta, "Massive mimo: An introduction," *Bell Labs Technical Journal*, vol. 20, pp. 11–22, 2015, ISSN: 1538-7305. DOI: `10.15325/BLTJ.2015.2407793`.

[85] J. Dunn, B. Nikolic, A. Niknejad, and E. Alon, "An open , scalable massive mimo testbed operating at e- band frequencies," Ph.D. dissertation, University of California Berkeley, 2020.

[86] E. Naviasky, L. Iotti, G. Lacaille, B. Nikoli, and E. Alon, "Beamforming integrated receiver in 28nm cmos," pp. 218–220, 2021.

[87] L. Iotti, G. Lacaille, and A. M. Niknejad, "A 12mw 70-to-100ghz mixer-first receiver front-end for mm-wave massive-mimo arrays in 28nm cmos," pp. 414–416, 2018.

[88] M. Wade, "Teraphy: A chiplet technology for low-power, high-bandwidth in-package optical i/o," *2019 IEEE Hot Chips 31 Symposium,*, 2019. DOI: `10.1109/HOTCHIPS.2019.8875658`.

[89] L. Gao, Q. Ma, and G. M. Rebeiz, "A 4.7 mw w-band lna with 4.2 db nf and 12 db gain using drain to gate feedback in 45nm cmos rfsoi technology," *Digest of Papers - IEEE Radio Frequency Integrated Circuits Symposium*, vol. 2018-June, no. c, pp. 280–283, 2018, ISSN: 15292517. DOI: `10.1109/RFIC.2018.8428986`.

[90] R. A. Soref and B. R. Bennett, "Electrooptical effects in silicon," *IEEE Journal of Quantum Electronics*, vol. 23, no. 1, pp. 123–129, 1987, ISSN: 15581713. DOI: `10.1109/JQE.1987.1073206`.

[91] M. Nedeljkovic, R. Soref, and G. Z. Mashanovich, "Free-carrier electrorefraction and electroabsorption modulation predictions for silicon over the 1-14-μm infrared wavelength range," *IEEE Photonics Journal*, vol. 3, no. 6, pp. 1171–1180, 2011, ISSN: 19430655. DOI: `10.1109/JPHOT.2011.2171930`.

[92] L. Chrostowski and M. Hochberg, *Silicon Photonics Design: From Devices to Systems.* Cambridge: Cambridge University Press, 2015.

[93] S. Lin, S. Moazeni, K. T. Settaluri, and V. Stojanović, "Electronic-photonic co-optimization of high-speed silicon photonic transmitters," *Journal of Lightwave Technology*, vol. 35, no. 21, pp. 4766–4780, 2017, ISSN: 07338724. DOI: `10.1109/JLT.2017.2757945`.

[94] S. Lin, *Silicon photonics simulink toolbox*, 2017. [Online]. Available: `https://github.com/isgcal/SiPh%7B%5C_%7DSimulink`.

[95] A. M. Niknejad, *Integrated circuits for communications (ee142,) lecture notes*, 2016. [Online]. Available: `http://rfic.eecs.berkeley.edu/142/lectures.html`.

[96] A. Jain *et al.*, "A high spur-free dynamic range silicon dc kerr ring modulator for rf applications," *Journal of Lightwave Technology*, vol. 37, no. 13, pp. 3261–3272, 2019, ISSN: 15582213. DOI: `10.1109/JLT.2019.2913638`.

[97] M. Song *et al.*, "Nonlinear distortion in a silicon microring-based electro-optic modulator for analog optical links," *IEEE Journal on Selected Topics in Quantum Electronics*, vol. 16, no. 1, pp. 185–191, 2010, ISSN: 1077260X. DOI: `10.1109/JSTQE.2009.2030154`.

[98] J. Hamilton, D. Franson, and N. Seiberlich, "Recent advances in parallel imaging for mri," *Progress in Nuclear Magnetic Resonance Spectroscopy*, vol. 101, pp. 71–95, 2017, ISSN: 00796565. DOI: `10.1016/j.pnmrs.2017.04.002`.

[99] Siemens, *Magnetic resonance imaging*, 2022. [Online]. Available: `https://www.siemens-healthineers.com/en-us/magnetic-resonance-imaging`.

[100] M. A. Ohliger and D. K. Sodickson, "An introduction to coil array design for parallel mri," *NMR in Biomedicine*, vol. 19, no. 3, pp. 300–315, 2006, ISSN: 09523480. DOI: `10.1002/nbm.1046`.

[101] J.-M. Verret, F. Pilleul, O. Beuf, and C. Rabrait, "Distribution of rf traps to reduce rf heating with endoluminal coils: An experimental study," in *ISMRM 21st Annual Meeting & Exhibition*, 2013.

[102] B. Sporrer *et al.*, "A fully integrated dual-channel on-coil cmos receiver for array coils in 1.5-10.5 t mri," *IEEE Transactions on Biomedical Circuits and Systems*, vol. 11, no. 6, pp. 1245–1255, 2017, ISSN: 19324545. DOI: `10.1109/TBCAS.2017.2764443`.

[103] J. Reber *et al.*, "An in-bore receiver for magnetic resonance imaging," *IEEE Transactions on Medical Imaging*, vol. 39, no. 4, pp. 997–1007, 2020, ISSN: 1558254X. DOI: `10.1109/TMI.2019.2939090`.

[104] J. Yuan, J. Wei, and G. X. Shen, "A 4-channel coil array interconnection by analog direct modulation optical link for 1.5-t mri," *IEEE Transactions on Medical Imaging*, vol. 27, no. 10, pp. 1432–1438, 2008, ISSN: 02780062. DOI: `10.1109/TMI.2008.922186`.

[105] M. Fan *et al.*, "A high-dynamic-range digital RF-over-fiber link for MRI receive coils using delta-sigma modulation," *Review of Scientific Instruments*, vol. 92, no. 6, 2021, ISSN: 10897623. DOI: `10.1063/5.0047041`. eprint: `2105.13305`. [Online]. Available: `https://doi.org/10.1063/5.0047041`.

[106] R. Frass-Kriegl *et al.*, "Flexible 23-channel coil array for highresolution magnetic resonance imaging at 3 tesla," *PLoS ONE*, vol. 13, no. 11, pp. 1–16, 2018, ISSN: 19326203. DOI: `10.1371/journal.pone.0206963`.

[107] E. Chang *et al.*, "Bag2: A process-portable framework for generator-based ams circuit design," *2018 IEEE Custom Integrated Circuits Conference, CICC 2018*, pp. 1–8, 2018. DOI: `10.1109/CICC.2018.8357061`.

[108] S. Lin, "Electronic-photonic co-design of silicon photonic interconnects," Ph.D. dissertation, University of California Berkeley, 2017.

[109] A. F. Oskooi, D. Roundy, M. Ibanescu, P. Bermel, J. D. Joannopoulos, and S. G. Johnson, "Meep: A flexible free-software package for electromagnetic simulations by the FDTD method," *Computer Physics Communications*, vol. 181, no. 3, pp. 687–702, 2010, ISSN: 00104655. DOI: `10.1016/j.cpc.2009.11.008`. [Online]. Available: `http://dx.doi.org/10.1016/j.cpc.2009.11.008`.

[110] H. Gevorgyan, A. Khilo, and M. A. Popovic, "Broadband efficient coupled-cavity electro-optic modulators based on q engineering for rf photonics applications," *2018 Conference on Lasers and Electro-Optics, CLEO 2018 - Proceedings*, no. c, pp. 1–2, 2018.